Title
Submolecular Resolution Spectroscopic Imaging for Photoactive Molecules and Assemblies

Author
Wang, Shenkai

Publication Date
2019

Peer reviewed|Thesis/dissertation

UNIVERSITY OF CALIFORNIA

Los Angeles

Submolecular Resolution Spectroscopic Imaging for Photoactive Molecules and Assemblies

A dissertation submitted in partial satisfaction of the

requirements for the degree Doctor of Philosophy

in Chemistry

by

Shenkai Wang

2019

ABSTRACT OF THE DISSERTATION

Submolecular Resolution Spectroscopic Imaging

for Photoactive Molecules and Assemblies

by

Shenkai Wang

Doctor of Philosophy in Chemistry

University of California, Los Angeles, 2019

Professor Paul S. Weiss, Chair

Characterizing photon absorption and excitation at the nanoscale is an important tool for optimizing and applying photoactive systems. Coupling laser irradiation and scanning tunneling microscopy (STM) enables the measurement of photo-generated carriers with submolecular precision. Here, we introduce a custom-built laser-assisted STM that employs evanescent illumination and functions at ambient conditions and room temperature. Laser beams (405 nm, 633 nm, and 780 nm) are frequency modulated by a mechanical chopper wheel and incorporated into the tunneling junction through total internal reflection. Photo-induced changes in tunneling current are detected phase-sensitively by a lock-in amplifier and in-phase signal that is related to local photoelectron density is recorded at every pixel during the raster scans to generate maps of

photo-induced carriers. Non-absorbing *n*-dodecanethiolate (C12) self-assembled monolayers (SAMs) are used to test thermal effects and as negative controls for photoactive molecules.

We measured photo-induced charge separation in isolated individual C_{60}-tethered 2,5-dithienylpyrrole triad (C_{60} triad) molecules with submolecular resolution under 405 nm laser illumination. Photo-induced charge separation was not detected for all C_{60} triad molecules, indicating that the conformations of the molecules may affect their excitation probability, lifetime, and/or charge distribution. Photo-induced signal was not observed for dodecanethiol molecules in the surrounding matrix nor for control molecules without C_{60} moieties, as neither absorbs incident photons at these energies. We also studied solution-deposited titanyl phthalocyanine (TiOPc) SAMs on Au{111} using the laser-assisted STM. We observed hexagonal and rectangular lattice structures in TiOPc SAMs that are different from previously reported self-assembled structures in ultra-high vacuum and more related to the crystal structures of TiOPc. The photo-responses of TiOPc SAMs were characterized with 633 nm and 780 nm laser illumination. The distributions of photoelectrons in hexagonal lattice matches with theoretical calculated charge density changes in TiOPc molecules upon excitation. However, the photo-responses of TiOPc molecules in rectangular lattices are different from those expected; TiOPc molecules in this arrangement may have low probabilities of activation by 633 nm and 780 nm light. Our results suggest that the photo carrier generation efficiency of TiOPc molecules is related to their packing arrangement in SAMs and local environment.

In a study aiming to fabricate molecular level mixed *p*-*n* junctions in SAMs, we explored the reactivity of 1-decaboranethiolate SAMs and discovered that the reaction between 1-decaboranethiolate and 4-phenyl-1-butyne (4p1b) results in highly ordered 4p1b SAMs. The

initially disordered 1-decaboranethiolate changed into ordered ($\sqrt{3}\times\sqrt{3}$)*R*30° lattices on Au{111} typical of alkyne SAMs, indicating the complete substitution of 1-decaboranethiolate moieties, as determined by nanoscale imaging with scanning tunneling microscopy and X-ray photoelectron spectroscopy. Vibrational spectroscopy results indicate that the process happens gradually and that alkynyl groups are not totally oxidized in the ordered 4-phenyl-1-butyne monolayer.

Our spectroscopic imaging method can elucidate the change of electronic structures of photoactive molecules and assemblies upon activation and spatially resolve it. By analyzing the photo-induced charge distributions in individual molecules and SAMs, we can elucidate the effects of molecular structure, intermolecular interactions, and local environment on the probabilities of photoactivation and energy conversion. Such information can guide the design of molecules and nanostructures for photovoltaics and the modification of processing route for devices for higher performance.

The dissertation of Shenkai Wang is approved.

William M. Gelbart

Alexander Michael Spokoyny

Aydogan Ozcan

Paul S. Weiss, Committee Chair

University of California, Los Angeles

2019

For my family

Table of Contents

List of Figures

List of Abbreviations and Symbols

4p1b	4-phenyl-1-butyne
C12	*n*-dodcanethiolate
C_{60} triad	C_{60}-tethered 2,5-dithienylpyrrole triad
DPSe	diphenyl diselenide
DTP	2,5-dithienylpyrrole derivative
FTIR	Fourier transform infrared spectroscopy
HOMO	highest occupied molecular orbital
HOPG	highly oriented pyrolytic graphite
LUMO	lowest unoccupied molecular orbital
Mithrene	silver benzeneselenolate
MOCHA	metal-organic chalcogenolate assemblies
MPEA	9-(4-mercapto-phenylethynyl) anthracene
OPE	oligo(phenylene ethynylene)
SAM	self-assembled monolayer
SERS	surface-enhanced Raman spectroscopy
SNOM	scanning near-field optical microscopy
STM	scanning tunneling microscopy
TERS	tip-enhanced Raman spectroscopy
TiOPc	titanyl phthalocyanine
UV	ultraviolet
XPS	X-ray photoelectron spectroscopy

Å	Ångström
°C	degree Celsius
cm^{-1}	wavenumber
eV	electronvolt
Hz	hertz
h	hour
kHz	kilohertz
mM	millimolar
mL	milliliter
mm	millimeter
nm	nanometer
pA	picoAmpere
s	second
V	volt
µL	microliter
µm	micrometer

Acknowledgements

This dissertation represents the majority of the research I have done during my graduate education at UCLA. My research experience in Prof. Paul Weiss group is precious and rewarding, during which I have acquired the essential abilities and qualities needed to become a scientist. I would like to take the opportunity to express my gratitude to the professors, colleagues, and friends who helped me during this journey.

I am very lucky to be one of Prof. Paul Weiss's graduate students. Paul is an intelligent scientist with profound experience and insight in chemical research. He emphasizes the importance of identifying valuable scientific problems and exploring the impact of our research. Under his guidance, I have forged and polished my skills to design comprehensive research procedures and to present my research in a convincing manner. None of the work in this dissertation could have been accomplished without his support.

I would like to thank my committee members Prof. William Gelbart, Alexander Spokoyny, and Aydogan Ozcan. Their constructive advice and valuable criticism helped me enhance my researches and broaden my ideas. It is my great pleasure to collaborate with Prof. Anastassia Alexandrova from UCLA, Prof. Alex Jen from University of Washington, Seattle (now at City University Hong Kong), Dr. Tomáš Baše from The Czech Academy of Sciences, and Dr. J. Nathan Hohman from Lawrence Berkeley National Lab (now at the University of Connecticut). Their expertise in theoretical and synthetic chemistry allows me to extend the boundaries of my research and to fortify the conclusions we draw.

I also want to thank all the members from the Weiss group for providing a motivative and cooperative research environment. I want to give special thanks to Dr. Naihao Chiang, Dr. Natcha

Wattanatorn, Diana Yugay, Dominic P. Goronzy, Kris Barr, Logan Stewart, Thomas D. Young, and Kevin Cheung, for their help and support. The discussions we had and the thoughts we shared are invaluable for me to complete my graduate research.

The instruments I used for my research were developed from the support of US Department of Energy (DE-SC-0005161). The analysis and image processing methods were developed under the support of W. M. Keck Foundation. I also want to thank UCLA and California NanoSystems Institute for providing facilities.

Finally, I want to thank my family. It's the love from my parents that supports me to overcome the difficulties and pursue my dream as a scientist.

VITA

Shenkai Wang obtained his Bachelor of Science degree in chemistry from Peking University in 2010. While in Peking University, he did research in Prof. Kai Wu's group focusing on the study of the self-assembly of organic semiconductors embedded in peptide frameworks. Shenkai joined Prof. Paul S. Weiss group as a graduate student in 2014. His research in the Weiss group focuses on the development of a laser-assisted scanning tunneling microscopy and the study of photo-responses of photoactive molecules and assemblies.

List of Selected Publications and Presentations

Wang, S.; Goronzy, D.; Young, T.; Wattanatorn, N.; Stewart, L.; Baše, T.; Weiss, P. S., Formation of Highly Ordered Terminal Alkyne Self-Assembled Monolayers on Au{111} Surface through Substitution of 1-Decaboranethiolate.*The Journal of Physical Chemistry C* **2019,** *123*, 1348–1353.

Wang, S.; Wattanatorn, N.; Chiang, N.; Zhao, Y.; Kim, M.; Ma, H.; Jen, A. K.-Y.; Weiss, P. S., Photo-Induced Charge Transfer in Single Molecule *p-n* Junctions. *The Journal of Physical Chemistry Letters* **2019,** *10*, 2175–2181.

Wang, S.; Chiang, N.; Guo, H.; Wattanatorn, N.; Barr, K.; Alexandrova, A.; Weiss, P. S., Photoinduced Carrier Distribution in Titanyl Phthalocyanine Monolayers. *Submitted*.

Wang, S.; Wattanatorn, N.; Chiang, N.; Weiss, P. S., Submolecular Resolution Spectroscopic Imaging for Photoactive Molecules and Assemblies. Fall ACS National Meeting, Boston, MA, August 2018.

CHAPTER 1

Detection of Single-Molecule Optical Response with Laser-Assisted Scanning Tunneling Microscopy

1.1 Introduction

Understanding photon excitation and energy conversion at the nanoscale is critical for applications in many areas of science and technology, such as catalysis,[1-4] spectroscopy,[5] plasmonics,[6] and photovoltaics.[7-11] Exploring photo-induced charge transfer at the molecular level can provide fundamental information needed for enhancing the efficiency of light harvesting and emission devices. At the same time, considerable effort has been directed toward the manipulation of the electronic structure and conformation of single molecules and nanostructures using electromagnetic waves. However, characterization of the interactions between light and matter at the single molecular level remains challenging since traditional optical methods are restricted by the diffraction limit of the light applied. In order to circumvent this limit, a variety of techniques based on scanning probe microscopy have been developed, including tip-enhanced Raman spectroscopy,[5,12-16] break junction measurements,[17-20] inelastic electron tunneling spectroscopy,[21] ultrafast optical excitation,[22-24] photon emission from local excitation,[11,25,26] and microwave polarizability mapping.[27,28] However, most of the available approaches require ultrahigh vacuum and/or low temperature, which make these techniques time consuming, complicated, and of limited relevance to real systems. A technique that can characterize photoactive molecules under ambient conditions at room temperature can be more useful for optoelectronic research.

Scanning tunneling microscopy (STM), and associated spectroscopic imaging methods, with atomic resolution, have been widely used to investigate electron transfer through single molecules and assemblies in metal-molecule-metal junctions.[12,27,29-35] Incorporating laser irradiation into the tunneling junction further extends the ability of STM and enables us to probe photo-induced carrier dynamics at the nanoscale.[24,36-53] However, direct illumination of the tunneling junction results in

thermal drift and thermal expansion, which interfere with the measured tunneling current changes caused by photoabsorption of molecules or nanostructures. In this chapter, I introduce our custom-built laser-assisted STM that functions under ambient conditions at room temperature while minimizing the effects of laser heating by evanescent field excitation. The characterization of photoactive molecules isolated in the defects of *n*-dodecanethiolate self-assembled monolayers (SAMs) or form assemblies by themselves on Au{111} will be introduced in subsequent chapters.

1.2 Laser-Combined Scanning Tunneling Microscopy

Scanning tunneling microscopy (STM) provides a way to study molecules and nanomaterials with atomic resolution in real time and space. For a small bias and constant current, a STM image corresponds to a map of constant local state density at the Fermi level,[30,49,54,55] and is correlated with local morphology and atomic and/or molecular orbitals.[56-61] Therefore, STM can track the changes of geometric and electronic structures of molecules and nanostructures upon perturbations and modulations (*i.e.*, electric field) and provide valuable information that is inaccessible to ensemble measurements. Electromagnetic waves are among the most important and useful modulations that can be introduced into the tunneling junction. Measuring photon absorption of the molecular junction enables chemical identification with STM while the atomically resolved absorption map can provide fundamental insights that will not only facilitate theoretical studies but guide the engineering of the system as well. Techniques that measure the photo-response of molecules and nanomaterials in the tunneling junction optically and electronically will be introduced.

1.2.1 Optical Spectroscopy and Scanning Tunneling Microscopy

Coupling optical spectroscopy with STM can greatly enhance the sensitivity and spatial resolution of spectroscopic imaging, since the geometry of the metal STM tip allows it to provide significant field enhancement and coupling between electromagnetic near-field and far-field radiation.[11] One technique developed based on this principle is scanning near-field optical microscopy (SNOM).[48,62-64] For this technique, a metal-coated glass fiber with a submicrometer aperture at its end is generally used to guide the light to illuminate the surface. The interaction between light and the object can be detected by radiated light or reflected light going back through the fiber, and the diffraction limit can be overcome by near-field probing with the subwavelength aperture. In some cases, a nanometer-sized optical antenna is attached to the aperture for better resolution.[65]

Another technique that uses STM to facilitate optical spectroscopy is tip-enhanced Raman spectroscopy (TERS).[5,66] As a powerful variant of surface-enhanced Raman spectroscopy (SERS), TERS can be applied to a wide range of systems. For TERS, a laser can be focused on the apex of the metal STM tip and Raman spectra can be collected at every pixel during raster scans of the surface. The geometry and the plasmonic modes of the metal tip can provide pronounced field enhancement. Maps featuring different vibrational modes can be generated by registering the integrated intensity of a TERS peak at every pixel.[5,66] By correlating the vibrational maps with topographic data, information on the vibrational activity within molecules can be visualized in real space. This technique has been applied to a variety of systems such as biomolecules,[67-69] carbon nanomaterials,[70-73] and photoactive molecules used for photovoltaics or optoelectronics.[74-76]

1.2.2 Electrical Detection of Photon Absorption by Scanning Tunneling Microscopy

Photo-induced geometric and/or electronic structural changes of molecules or nanomaterials in a STM junction will result in changes in the tunneling current. For techniques that measure such tunneling current changes, the lasers applied are normally frequency modulated and phase-locked, so that a lock-in amplifier can be used to detect the laser-induced tunneling current changes,[45,49,50,53,77] as such changes make only small contributions to the total current. With such techniques, photo-induced carrier distribution across the surface can be spatially resolved with nanometer-scale resolution. Important photoactive systems such as carbon nanotubes,[45,50,78] quantum dots,[52,77,79] gold nanostructures,[80] semiconductor devices,[81-83] and single molecule *p-n* junctions[53] have been characterized with such experimental approaches. The distribution of photo-induced carriers being visualized in these studies illustrates the charge distribution changes in these systems upon activation and the effect of local environments on the charge generation efficiencies, which cannot be acquired by traditional spectroscopic methods. Detailed information provided by these experiments can be used as a guidance for designing more efficient photoactive systems and for fabricating single-molecule devices.

Absorption of single photons in STM molecular junctions can be measured by the application of ultrafast lasers.[22,42] The generation of hot electrons charging a molecule within the tunneling junction has been observed by one- and two-photon excitation.[24] As an advanced variant of this method, two laser pulses (pump and probe) that are separated by a variable delay time can be generated and applied to study the dynamics of the photo carriers.[51]

Laser illumination of the tunneling junction can cause thermal expansion,[22,84-88] which decreases the distance between the STM tip and substrate and increases the tunneling current during the

delay time of the feedback loop circuit. Therefore, most of laser-combined STM techniques that detect photon absorption electrically introduce laser illumination into the tunneling junction through total internal reflection to minimize the thermal effect.

1.3 Self-Assembled Monolayers

Self-assembled monolayers (SAMs) have been intensively studied because of their well-defined and modular structures and chemical properties that provide functionalized surfaces for scientific studies and technological exploration and application.[89-95] With rational design of molecules in SAMs, we control the physical and chemical properties of the surface and use bottom-up approaches to fabricate nanostructures and devices.[96-100]

The most extensively studied class of SAMs is derived from the adsorption of alkanethiols on metal surfaces. The high affinity of thiols for the surfaces of noble and coinage metals makes it possible to generate well-defined organic surfaces with useful and highly alterable chemical functionalities displayed at the exposed interface.[99-101] Other anchor groups have also been studied but are less commonly used since they typically result in weaker bonds and disordered SAMs.[102-106] Meanwhile, physically adsorbed SAMs of organic or organometallic molecules on metals or highly oriented pyrolytic graphite (HOPG) surfaces also received significant attention.[107,108] The arrangements of molecules in these SAMs can be different from that in their crystals,[109] but they resemble the molecular arrangements at the electrode interfaces in thin film electronic devices. Therefore, these SAMs can serve as model systems to study electron transfer at electrode interfaces and potentially guide the fabrication process to achieve higher device efficiency.[110,111]

1.3.1 Defects in Self-Assembled Monolayers of Thiols on Gold

Self-assembled monolayers formed by thiol molecules on Au surfaces are air-stable, highly ordered, and can be easily fabricated, which makes them ideal candidates for surface modification and surface research under ambient conditions.[99-101,112] The chemical and steric structures of thiol molecules can affect their conformations in SAMs and result in defects of different types and densities.[98,113,114] The density of defects can also be controlled by the fabrication processes and subsequent treatment of the SAMs.[115] Such defects have been thoroughly explored by STM and widely used to isolate functional molecules so that they can be studied individually under ambient conditions at room temperature.[27,34,47,113,116-119] The thiol molecules used as the matrices can provide well defined restrictive environments while acting as negative controls for observing the behavior of target molecules. Furthermore, the local environments in the defects is related to the arrangements of neighboring molecules and can affect the properties of the functional molecules inserted. For example, it has been shown that the switching rate of oligo(phenylene ethynylene) (OPE) molecules depends on the tightness of the defects into which they are inserted, indicating that some extent of molecular motion is a critical part of the switching.[113,120] The switching of OPE molecules can be visualized in STM topographic images as apparent height changes compared to neighboring thiol matrix molecules.[121]

1.3.2 Photoactive Molecules in Well-Defined Nanoscale Environments

Self-assembled monolayers of alkanethiols provide a viable way to isolate photoactive molecules and to measure and to control their photo-responses at the single-molecule level under ambient conditions and at room temperature.[114] For example, azobenzene-functionalized molecules with non-conductive, saturated tethers have been inserted and isolated in

1-decanthiolate SAMs and the photoisomerization of the azobenzene group has been studied by STM[118] and SERS[122] with ultraviolet (UV) and visible light illumination. It has been shown that the photoisomerization of the azobenzene groups from *trans* to *cis* conformation was triggered by UV light illumination (365 nm) and could revert back via thermal relaxation or under visible light illumination (450 nm).

As a potential precursor for organic photovoltaic molecules, 9-(4-mercapto-phenylethynyl) anthracene (MPEA) molecules have been inserted in *n*-dodecanethiolate SAMs and studied with laser-combined STM.[123] The apparent height of MPEA molecules increased compared to the surrounding matrices under 365 nm light illumination. Since the restrictive environment in *n*-dodecanethiol SAMs limits the changes in the geometry of MPEA molecules, the increased apparent height can be attributed to the changes of the intrinsic conductance of MPEA molecules under light activation.

Regioselective reactions between neighboring MPEA molecules have also been observed in the defects in *n*-dodecanethiol SAMs.[47] Symmetric disulfide derivatives of MPEA were used to ensure close contact of neighboring molecules with upright configuration in the defects. Non-centrosymmetric [4 + 4] photocycloaddition reaction, which is not favored in solution, has been observed between adjacent surface bound MPEA molecules. Since the product molecules have lower conductance than MPEA, the decreased apparent height of protrusions were used as indications of the reaction.

1.4 Custom-Built Laser-Assisted Scanning Tunneling Microscope

In this section, I introduce our custom-built laser-assisted STM (Figure 1.1) that characterizes photo-induced carrier distributions with submolecular resolution under ambient conditions at room

temperature. We adopt the Kretschmann-Raether geometry and introduce evanescent illumination of the tunneling junction through total internal reflection. Such a configuration has been described by Scherer, Lyding, and other groups.38,40-42,45 Thin Au{111} films deposited on c-cut sapphire prism surfaces are used as substrates. Frequency modulated p-polarized 405 nm, 633 nm, and 780 nm lasers are used as the light sources, and phase-sensitive measurements of the tunneling current are performed using a lock-in amplifier. We used n-dodecanethiolate SAMs to test the effect of thermal expansion, and the detection of thermal expansion is used to as an indicator for proper laser alignment and power.

1.4.1 System Design

Photographs of our custom-built laser-assisted STM are shown in Figure 1.2 to 1.5. The acoustic enclosure (Herzan LLC, NanoVault, Figure 1.2) housing the STM scanner is bolted to an optical table (Newport SmartTable®) with pneumatic legs and active damping cancellation, which is used for isolating floor vibrations and laser alignment. All cables passing through the wall of the acoustic chamber are tightly clamped with foam. The STM is placed on a vibration isolation platform (Minus K Technology Inc., 100BM) that has 1.5 Hz horizontal and 0.5 Hz vertical natural frequencies. The STM scanner is a cylindrical piezoelectric tube (EBL Products Inc.) mounted on two sets of approach micro sliders (Omicron MS-5, 40-400 nm movement per step in 5 mm distance). Four divided quadrants are used for raster scan while an inner electrode controls the distance between tip and sample. The lower micro slider (Micro Slider 2, see Figure 1.3) is used to move the tip parallel to the substrate surface plane in ~5 mm range. The upper micro slider (Micro Slider 1, see Figure 1.3) is used to bring the tip close to the surface stepwise until a tunneling current can be detected, or away from the surface without crashing the tip into the

surface. The Pt/Ir 80:20 tip wire with 250 μm diameter was supplied by Goodfellow Cambridge and was freshly cut before use. A Faraday cage is used to cover the STM to minimize electromagnetic noise. The tunneling current is detected using preamplifier (RHK Technology, Inc., Stage I: IVP-300, 109 V/A gain and Stage II: IVP-PGA, ×10 gain selected) configured to 1010 V/A gain and 5 kHz bandwidth. Data collection and control electronics are custom built with National Instrument PXI systems and described in previous publications.124

We use c-cut sapphire prism-supported metal films as substrates. The sample holder for the substrates is custom-built with stainless steel and is shown in Figure 1.4. The prism is fixed in position by screwing a cap with a hole in the center. The gold foil on the cap makes direct contact with the top surface of the sample and provides electrical contact to the current preamplifier via a gold spring. To prevent the spring from being shorted with electrically grounded sample holder, the stainless steel surface surrounding the spring is insulated with nail polish. The slit at the rear of the sample holder offers passage to incident and reflected laser beams.

Laser beams are transmitted through a broadband window on the wall of the acoustic enclosure and focused onto the Au/sapphire interface by a converging lens (focal length = 75 mm). The alignment of the focusing lens in the XYZ directions is accomplished by a stepper motor actuator (Newport Corporation, TRA25PPD). We have installed a motorized continuous rotation stage (Thorlabs Inc., CR1Z7) to align the lens focal plane perpendicular to the propagation direction of the incident beam. The light incident angle at Au/sapphire interface can be varied through the rotating stage (Newport Corporation, RV160PE-F) holding the STM scanner and sample holder. The relative position between the STM tip and the illumination spot can be visualized through a

digital camera (Thorlabs Inc., DCU223C) that has XYZ motion controlled by motorized translation stages (Newport Corporation, ILS200CC and Thorlabs Inc., MTS Series).

1.4.2 Sapphire Prism Supported Au{111} Surface

Thin (40 nm), flat (roughness 0.3-1 nm) epitaxial Au{111} films are deposited on *c*-cut sapphire cylindrical prisms. Half-cylindrical sapphire prisms (1 cm × 1 cm, 1 cm diameter) with *epi*-polished *c*-cut planes, $Al_2O_3(0001)$ were purchased from Meller Optics (Providence, RI). These substrates were annealed in air at 1100 ℃ and 1400 ℃ for 24 h and 18 h, respectively, in consecutive cycles. Thin Au{111} films were grown on *c*-cut plane sapphire prisms with a Nb seed layer.[125] The annealed sapphire substrates were introduced to the ultrahigh vacuum evaporator chamber with a base pressure in the 10^{-10} mbar range, and were outgassed for 1 h at 150 ℃ to remove adsorbed water. A 2-nm-thick Nb seed layer was evaporated at a rate of 0.15 Å/s at room temperature.[126] The pressure increased to ~5×10^{-9} mbar during evaporation. Room temperature deposition favors the Nb{110} orientation over Nb{111}, while elevated temperatures (over 800 ℃) yield Nb{111}.[127] The orientation of Au{111} is parallel to Nb{110} with the epitaxial relationship as follows:[126,128,129] $Au(111)[0\bar{1}1]||Nb\{111\}[001]||Al_2O_3/0001/[10\bar{1}0]$. Thin Au films (45 nm) were then deposited at a substrate temperature of 300 ℃ and an evaporation rate of 0.50 Å/s. The surface temperature should not exceed 300 ℃, to avoid inter-diffusion and intermetallic compounds (primarily $AuNb_3$ and Au_2Nb_3) that occur above 325 ℃.[130]

1.4.3 Laser Alignment and Phase-Sensitive Detection

Laser beams (*p*-polarized, 405 nm, Coherent Inc. CUBE diode laser, 633 nm, Melles Griot Inc. He/Ne laser, 780 nm, MTO Laser Inc. diode laser) are aligned to illuminate the same spot using Thorlabs optical elements (Figure 1.5). The power of the 405 nm laser can be controlled by

computer. The power of 633 nm and 780 nm lasers can be adjusted manually through an attenuator. A polarizer is used to ensure that the lasers are *p*-polarized. The lasers are modulated by a mechanical chopper wheel (Thorlabs Inc., MC1F60) to create a reference frequency input for the lock-in amplifier (Stanford Research Systems Inc., Model SR850), so that light-triggered changes in the tunneling current can be recorded phase sensitively. To ensure that the lasers are illuminating the raster scan area, the position of the tip is adjusted horizontally through Micro Slider 2 and vertically through the height of the vibration isolation platform under the monitor of the digital camera. Images of the STM tip under the illumination of the lasers are recorded by a digital camera and are shown in Figure 1.6. The incident angle we use for our experiments is 36°, as it is the total internal reflection angle for sapphire/Au interface for the three lasers we use. The electric field intensity distribution at the sapphire/Au/air interface for 405 nm light has been simulated previously,[123] which suggests that when the incident angle is 36°, total internal reflection is achieved and the evanescent field is strong enough to penetrate the 40 nm gold layer. We also measured the reflection coefficient of sapphire/Au interface for *p*-polarized 633 nm and 780 nm lasers and *s*-polarized 633 nm laser at different incident angles (Figure 1.7a). From Figure 1.7a, we see that for *p*-polarized 633 nm and 780 nm lasers, the minimum reflection coefficients at sapphire/Au interface are reached at ~36°. For an *s*-polarized 633 nm laser, there is not a significant change in the reflection coefficient, indicating that *s*-polarized lasers do not generate evanescent fields at sapphire/Au interfaces. Considering that errors in the incident angle can be introduced by the vibration isolation platform, we adjust the rotation stage over small ranges (± 0.5°) around 36° to reach total internal reflection each time we start a new experiment. A white paper behind the

STM scanner is used to observe the reflection spot and determine when the smallest reflection coefficient is reached.

Vapor-deposited *n*-dodecanethiolate (C12) SAMs on sapphire-prism supported Au{111} substrates are used to test the thermal effect of the lasers since C12 does not absorb visible light. Data collected under 633 nm laser illumination and a reference frequency of 4.8 kHz are shown in Figure 1.7b, as an example. Phase-sensitive signals caused by thermal expansion are observed. We can see that when the surface is under illumination, the in-phase lock-in signal increases when the sample bias is positive and decreases when the sample bias is negative. This change is because the polarity of the tunneling current corresponds to sample bias, so the phase shift of the thermal expansion induced tunneling current oscillation changes 180° when the polarity of the sample bias is flipped. Such thermal-expansion induced phase-sensitive signal can be used as an indicator for proper STM tip illumination and small adjustments in the relative position between the tip and illumination spot are made to maximize the thermal expansion signal before each experiment. However, the height of the vibration isolation platform and the tilt angle of the tip relative to the surface can vary for different samples and tips, so the thermal expansion signal intensity is not directly comparable between different experiments. We adjust the reference phase shift of the lock-in amplifier so that the phase shift of the thermal expansion signal is 0° for positive sample bias and 180° for negative sample bias. In this case, the intensity of the in-phase signal is maximized and we should not detect any quadrature signal. During the raster scan of the surface, we collect tip height information and in-phase lock-in signals simultaneously and generate topographic and spectroscopic images. In this way, the distribution of photo-induced carriers can be spatially resolved with submolecular resolution. The distribution of thermal expansion induced

in-phase signals were tested with C12 SAMs under 633 nm illumination and the results are shown in Figure 1.8. Figure 1.8a,b are simultaneously collected topographic and spectroscopic images at –1 V sample bias while Figure 1.8c,d are simultaneously collected topographic and spectroscopic images of C12 SAM at +1 V sample bias. The frequency of the chopper wheel was set as 5.0 kHz but there can be small fluctuations around the set point. Since the control system of our STM cannot obtain current signals at frequencies higher than 5.0 kHz, when the real frequency of the chopper is above 5.0 kHz, there is no thermal expansion-induced in-phase signal registered in the spectroscopic image. In Figure 1.8b,d, there are periodic regions showing the intrinsic noise of the lock-in amplifier. However, such unexpected data provide a convenient way to compare photo-induced signal and intrinsic noise. By comparing the highlighted hexagon regions in Figure 1.8, we can see that in our experimental setup, when the sample bias is negative, the thermal effect of the tunneling junction results in more negative in-phase signals corresponding to C12 molecules. When the sample bias is positive, the thermal effect results in more positive in-phase signals corresponding to C12 molecules. Such results can be used to determine whether the in-phase signals we collect for other systems are caused by thermal effects or photo-induced charge transfer. For systems in which thermal effect and photo-induced electrons are difficult to differentiate, it is advised that the same region should be characterized under both positive and negative bias. In the corresponding spectroscopic images, photo-induced electrons should correspond to more negative in-phase signals and photo-induced holes should correspond to more positive signals regardless of the polarity of the bias, while thermal expansion-induced in-phase signals should be negative at negative sample bias and positive at positive sample bias.

1.5 Dissertation Overview

This dissertation is organized as follows. Chapter 1 has discussed laser-augmented STM techniques and introduced our custom-built laser-assisted STM. Chapter 2 will demonstrate the characterization of photo-induced charge distribution in single molecule *p-n* junctions isolated in C12 SAMs. In Chapter 3, we will show two different lattice structures in solution deposited titanyl phthalocyanine (TiOPc) SAMs and their different photo-responses to 405 nm, 633 nm, and 780 nm lasers. In Chapter 4, we will describe the displacement process of 1-decaboranethiolate SAMs by 4-phenyl-1-butyane molecules on Au{111}. Conclusion and other systems that can be potentially characterized by our laser-assisted STM will be included in Chapter 5.

Chapter 2 has been reformatted from the manuscript:

Wang, S.; Wattanatorn, N.; Chiang, N.; Zhao, Y.; Kim, M.; Ma, H.; Jen, A. K. Y.; Weiss, P. S. Photoinduced Charge Transfer in Single-Molecule *p–n* Junctions. *J. Phys. Chem. Lett.* **2019,** *10*, 2175–2181.

Chapter 3 has been reformatted from a manuscript in preparation:

Wang, S.; Chiang, N.; Guo, H.; Wattanatorn, N.; Barr, K.; Alexandrova, A.; Weiss, P. S., Photoinduced Carrier Distribution in Titanyl Phthalocyanine Monolayers. *Submitted*.

Chapter 4 has been reformatted from the manuscript:

Wang, S.; Goronzy, D. P.; Young, T. D.; Wattanatorn, N.; Stewart, L.; Baše, T.; Weiss, P. S. Formation of Highly Ordered Terminal Alkyne Self-Assembled Monolayers on the Au{111} Surface through Substitution of 1-Decaboranethiolate. *J. Phys. Chem. C* **2019,** *123*, 1348-1353.

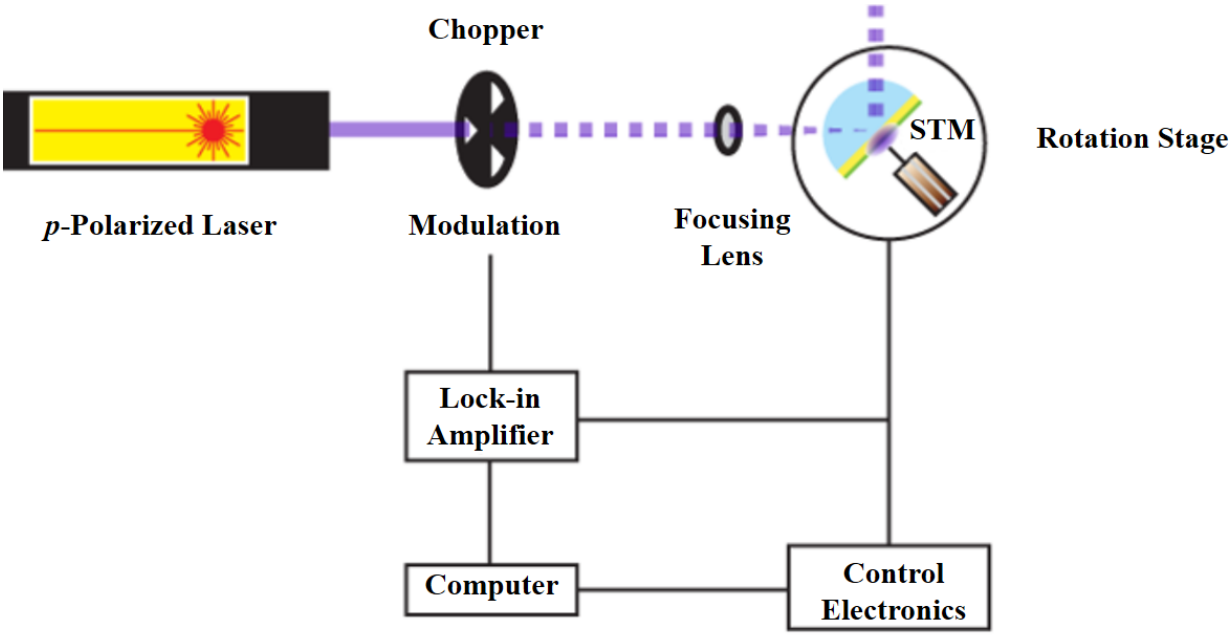

Figure 1.1. Scheme illustration of the experimental setup for laser-assisted scanning tunneling microscopy.

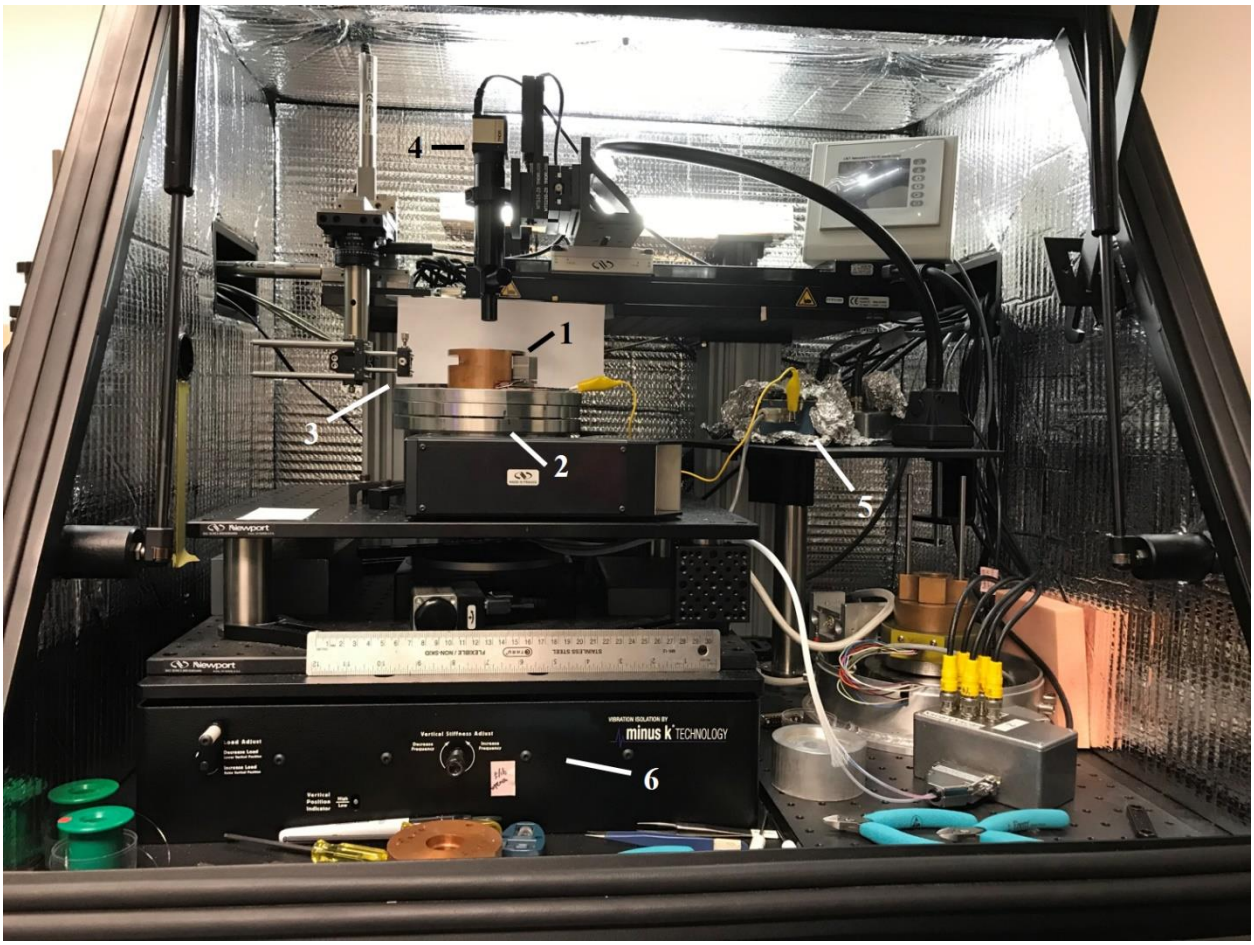

Figure 1.2. Photograph of the acoustic enclosure. The scanning tunneling microscope (STM) scanner (1) is bolted on a rotation stage (2) that is used to change incident angle of lasers. The lasers are focused through a converging lens (3) that is controlled by stepper motor actuator. A digital camera (4) is used to monitor the relative position of the STM tip and the illumination spot. Tunneling current is detected through a preamplifier (5). A vibration isolation platform (6) is used to minimize vibrational noise.

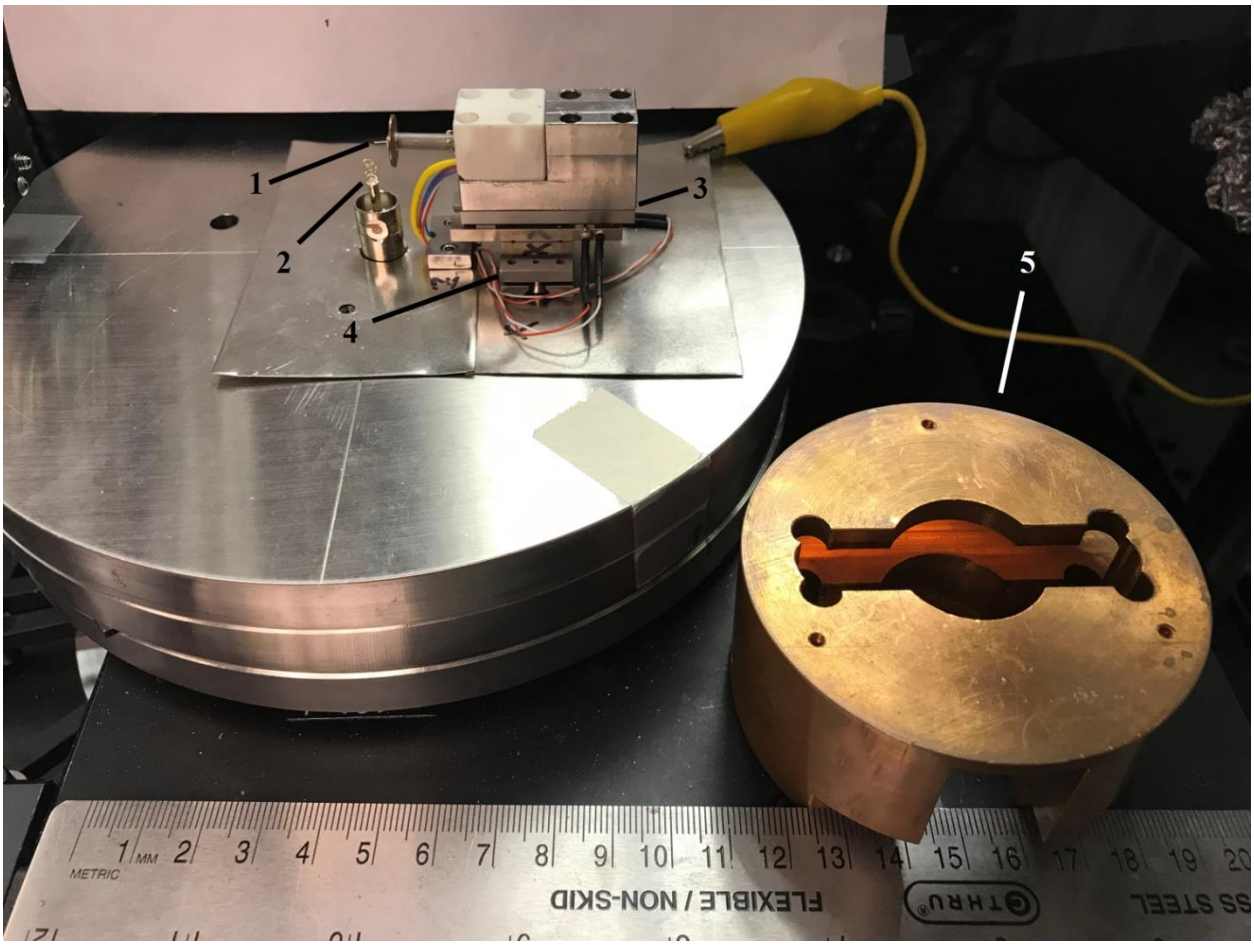

Figure 1.3. Photograph of the scanning tunneling microscope (STM) scanner. The raster scan is controlled by a piezoelectric tube (1). A gold spring (2) is used to provide electrical connect between the sample and the preamplifier. Micro slider 1 (3) and micro slider 2 (4) are used to provide primary control of the relative position between the tip and the substrate. A Faraday cage is used to minimize electromagnetic noise.

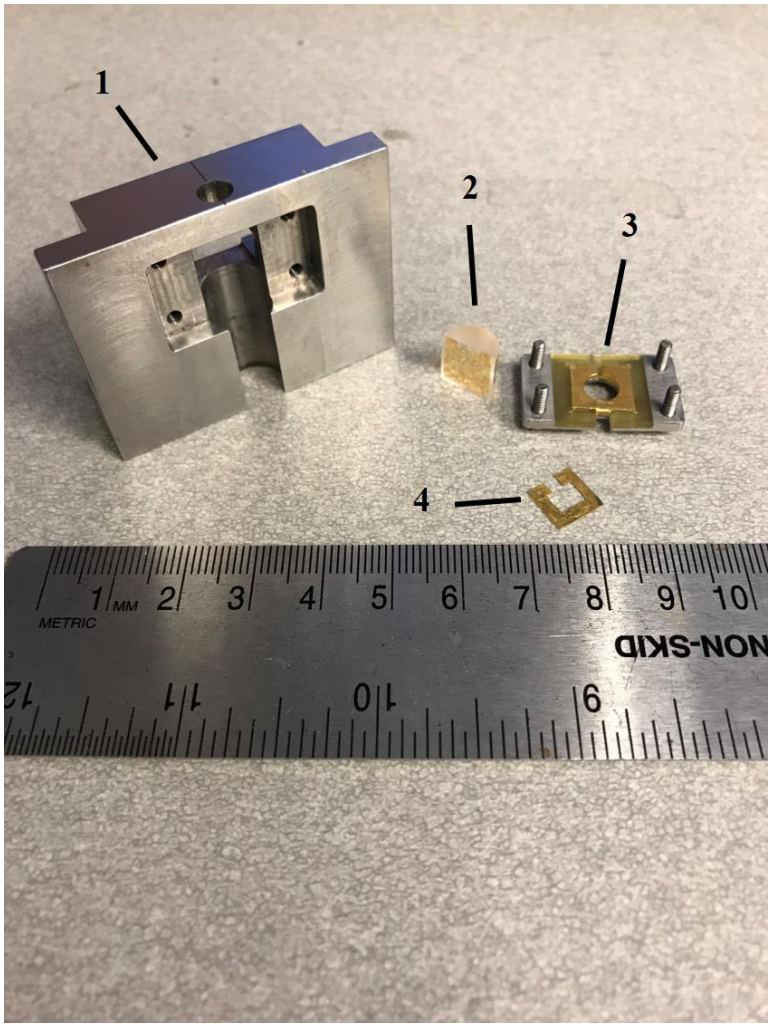

Figure 1.4. Photograph of the sample holder. The sample holder (1) is made for sapphire-prism supported metal film substrates (2). A cap (3) is used to hold the sample still. Gold foil (4) is used to provide electrical connect between the surface and the cap.

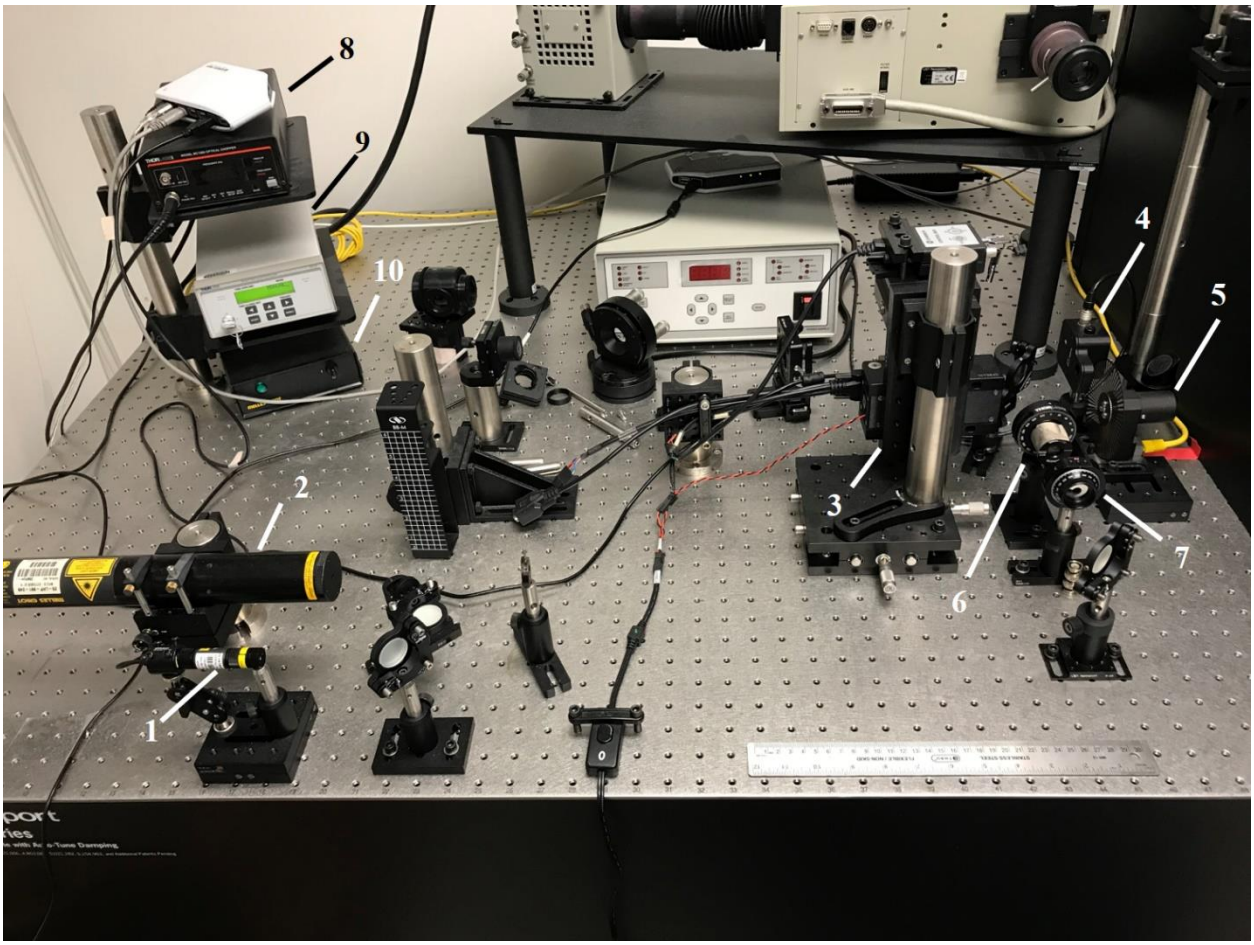

Figure 1.5. Photograph of the laser table. We use 780 nm (1), 633 nm (2), and 405 nm (3) lasers for our experiments. A shutter (4) is used to control the illumination of the sample. Lasers are frequency modulated by a chopper wheel (5). A polarizer (6) is used to ensure polarization of 780 nm and 633 nm lasers. The power of the 405 nm laser can be adjusted through computer program, while the power of 780 nm and 633 nm lasers can be adjusted manually using an attenuator (7). The chopper wheel is controlled by controller 8. The shutter is controlled by a computer program through adaptor 9. The 633 nm laser is controlled by power switch 10.

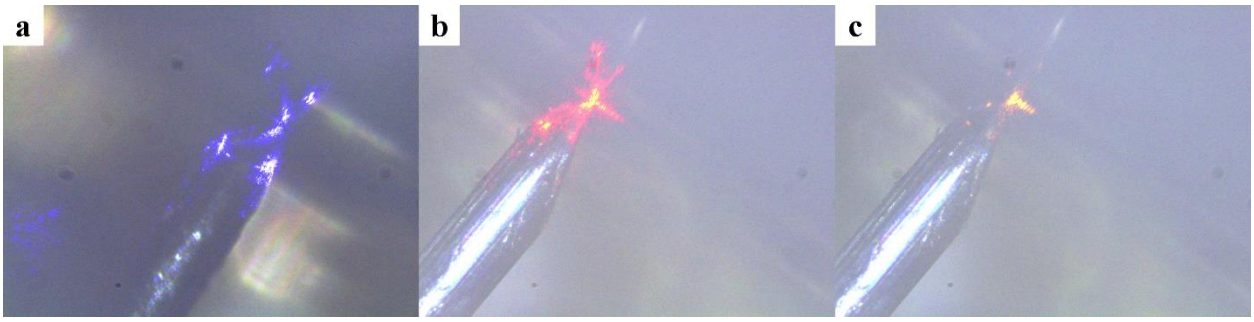

Figure 1.6. Photograph taken with a digital camera, showing the relative position between the scanning tunneling microscope probe tip and (a) 405 nm, (b) 633 nm, and (c) 780 nm laser illuminations spot. We use 36° as the incident angle for all three lasers.

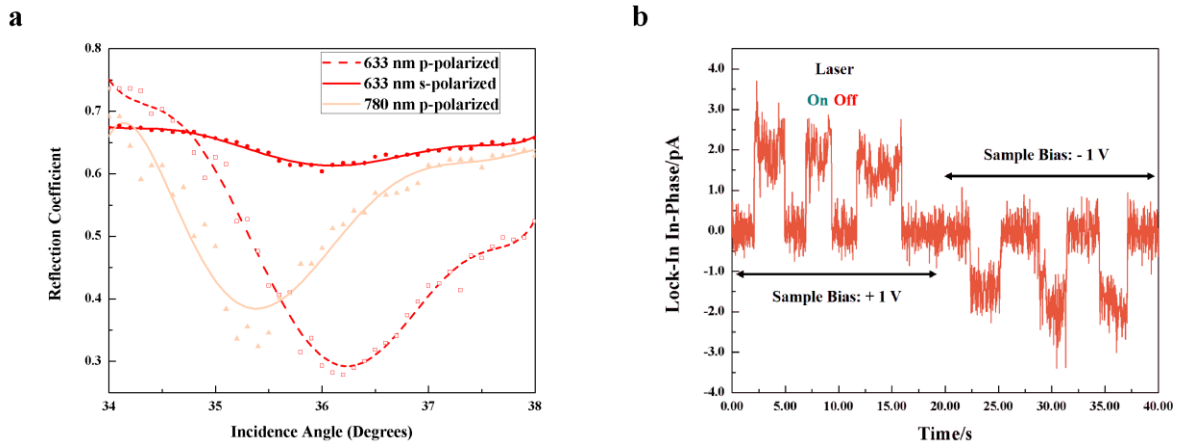

Figure 1.7. (a) Reflection coefficient of *p*-polarized 633 nm and 780 nm lasers and *s*-polarized 633 nm laser at the sapphire/Au interface at different incident angles. (b) Time track of in-phase lock-in signal collected under modulated evanescent illumination of *p*-polarized 633 nm laser (modulation frequency 4.8 kHz). The sample bias changed from +1.00 V to –1.00 V at time = 20 s.

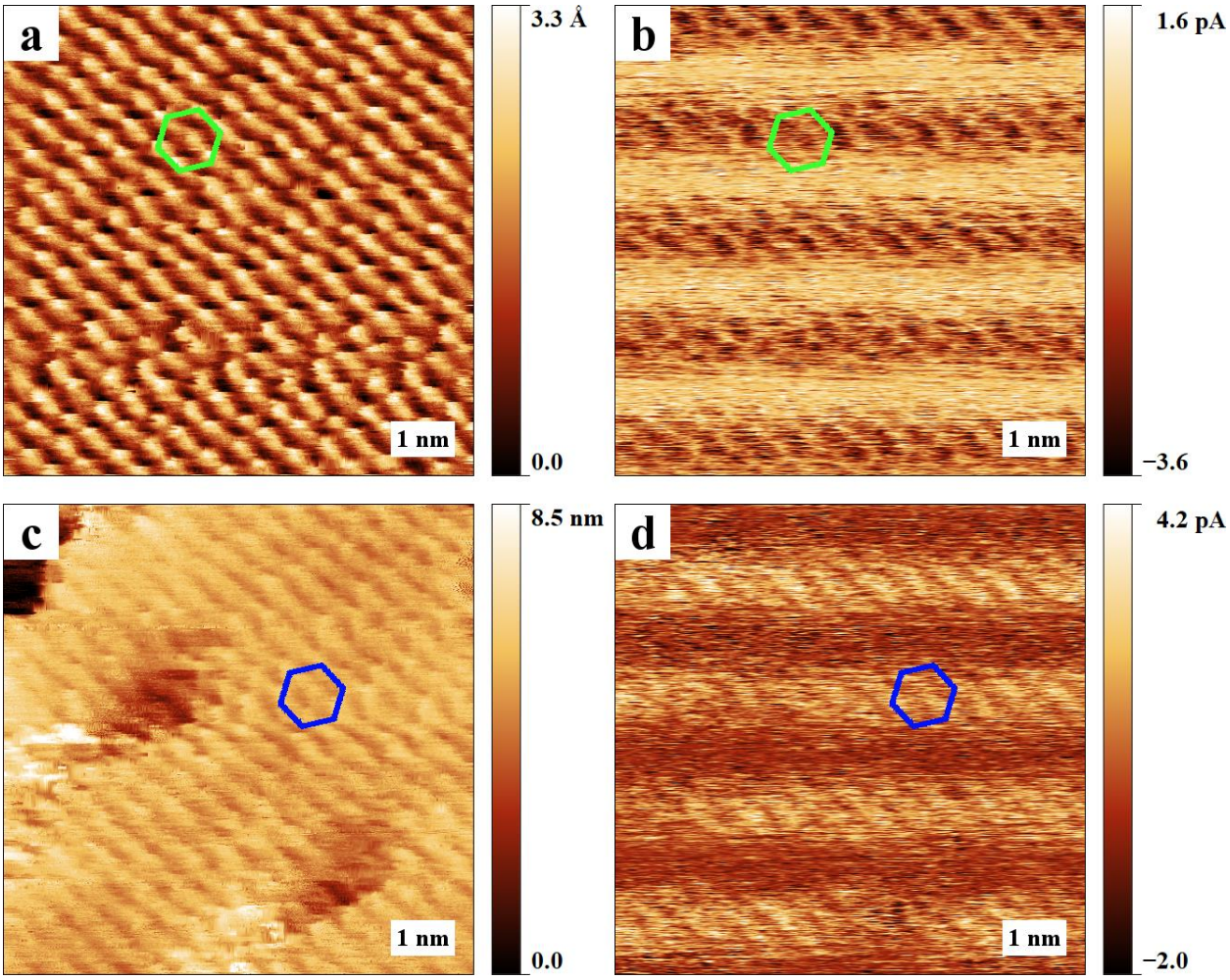

Figure 1.8. Scanning tunneling microscopy images showing *n*-dodecanethiol self-assembled monolayers under evanescent 633 nm laser illumination. (a) Topographic and (b) spectroscopic images were simultaneously obtained at a sample bias of –1.00 V and a tunneling current of 12.0 pA. The green hexagon highlights the same relative region. (c) Topographic and (d) spectroscopic images were simultaneously obtained at a sample bias of +1.00 V and a tunneling current of 12.0 pA. The blue hexagon highlights the same relative region.

REFERENCES

(1) Esswein, A. J.; Nocera, D. G. Hydrogen Production by Molecular Photocatalysis. *Chem. Rev.* **2007,** *107*, 4022–4047.

(2) Walter, M. G.; Warren, E. L.; McKone, J. R.; Boettcher, S. W.; Mi, Q. X.; Santori, E. A.; Lewis, N. S. Solar Water Splitting Cells. *Chem. Rev.* **2010,** *110*, 6446–6473.

(3) Chen, X. B.; Shen, S. H.; Guo, L. J.; Mao, S. S. Semiconductor-Based Photocatalytic Hydrogen Generation. *Chem. Rev.* **2010,** *110*, 6503–6570.

(4) Wang, H.; Zhang, L.; Chen, Z.; Hu, J.; Li, S.; Wang, Z.; Liu, J.; Wang, X. Semiconductor Heterojunction Photocatalysts: Design, Construction, and Photocatalytic Performances. *Chem. Soc. Rev.* **2014,** *43*, 5234–5244.

(5) Sonntag, M. D.; Pozzi, E. A.; Jiang, N.; Hersam, M. C.; Van Duyne, R. P. Recent Advances in Tip-Enhanced Raman Spectroscopy. *J. Phys. Chem. Lett.* **2014,** *5*, 3125–3130.

(6) Willets, K. A.; Duyne, R. P. V. Localized Surface Plasmon Resonance Spectroscopy and Sensing. *Annu. Rev. Phys. Chem.* **2007,** *58*, 267–297.

(7) Kamat, P. V. Meeting the Clean Energy Demand: Nanostructure Architectures for Solar Energy Conversion. *J. Phys. Chem. C* **2007,** *111*, 2834–2860.

(8) Gratzel, M. Recent Advances in Sensitized Mesoscopic Solar Cells. *Acc. Chem. Res.* **2009,** *42*, 1788–1798.

(9) Mishra, A.; Baeuerle, P. Small Molecule Organic Semiconductors on the Move: Promises for Future Solar Energy Technology. *Angew. Chem. Int. Ed.* **2012,** *51*, 2020–2067.

(10) Lin, Y. Z.; Li, Y. F.; Zhan, X. W. Small Molecule Semiconductors for High-Efficiency Organic Photovoltaics. *Chem. Soc. Rev.* **2012,** *41*, 4245–4272.

(11) Kuhnke, K.; Grosse, C.; Merino, P.; Kern, K. Atomic-Scale Imaging and Spectroscopy of Electroluminescence at Molecular Interfaces. *Chem. Rev.* **2017,** *117*, 5174–5222.

(12) Bumm, L. A.; Arnold, J. J.; Dunbar, T. D.; Allara, D. L.; Weiss, P. S. Electron Transfer through Organic Molecules. *J. Phys. Chem. B* **1999,** *103*, 8122–8127.

(13) Wassel, R. A.; Credo, G. M.; Fuierer, R. R.; Feldheim, D. L.; Gorman, C. B. Attenuating Negative Differential Resistance in an Electroactive Self-Assembled Monolayer-Based Junction. *J. Am. Chem. Soc.* **2004,** *126*, 295–300.

(14) Monnell, J. D.; Stapleton, J. J.; Dirk, S. M.; Reinerth, W. A.; Tour, J. M.; Allara, D. L.; Weiss, P. S. Relative Conductances of Alkaneselenolate and Alkanethiolate Monolayers on Au{111}. *J. Phys. Chem. B* **2005,** *109*, 20343–20349.

(15) Tao, N. J. Electron Transport in Molecular Junctions. *Nat. Nanotech.* **2006,** *1*, 173–181.

(16) Schmid, T.; Opilik, L.; Blum, C.; Zenobi, R. Nanoscale Chemical Imaging Using Tip-Enhanced Raman Spectroscopy: A Critical Review. *Angew. Chem. Int. Ed.* **2013,** *52*, 5940–5954.

(17) Battacharyya, S.; Kibel, A.; Kodis, G.; Liddell, P. A.; Gervaldo, M.; Gust, D.; Lindsay, S. Optical Modulation of Molecular Conductance. *Nano Lett.* **2011,** *11*, 2709–2714.

(18) Aradhya, S. V.; Venkataraman, L. Single-Molecule Junctions beyond Electronic Transport. *Nat. Nanotech.* **2013,** *8*, 399–410.

(19) Aram, T. N.; Ernzerhof, M.; Asgari, A.; Mayou, D. The Impact of Long-Range Electron-Hole Interaction on the Charge Separation Yield of Molecular Photocells. *J. Chem. Phys.* **2017,** *146*, 034103.

(20) Zhou, J.; Wang, K.; Xu, B.; Dubi, Y. Photoconductance from Exciton Binding in Molecular Junctions. *J. Am. Chem. Soc.* **2018,** *140*, 70–73.

(21) Moore, A. M.; Weiss, P. S. Functional and Spectroscopic Measurements with Scanning Tunneling Microscopy. *Annu. Rev. Anal. Chem.* **2008,** *1*, 857–882.

(22) Gerstner, V.; Knoll, A.; Pfeiffer, W.; Thon, A.; Gerber, G. Femtosecond Laser Assisted Scanning Tunneling Microscopy. *J. Appl. Phys.* **2000,** *88*, 4851–4859.

(23) Gaffney, K. J.; Miller, A. D.; Liu, S. H.; Harris, C. B. Femtosecond Dynamics of Electrons Photoinjected into Organic Semiconductors at Aromatic-Metal Interfaces. *J. Phys. Chem. B* **2001,** *105*, 9031–9039.

(24) Wu, S. W.; Ho, W. Two-Photon-Induced Hot-Electron Transfer to a Single Molecule in a Scanning Tunneling Microscope. *Phys. Rev. B* **2010,** *82*, 085444.

(25) Berndt, R.; Gimzewski, J. K. Photon Emission in Scanning Tunneling Microscopy: Interpretation of Photon Maps of Metallic Systems. *Phys. Rev. B* **1993,** *48*, 4746–4754.

(26) McCarty, G. S.; Weiss, P. S. Scanning Probe Studies of Single Nanostructures. *Chem. Rev.* **1999,** *99*, 1983–1990.

(27) Bumm, L. A.; Arnold, J. J.; Cygan, M. T.; Dunbar, T. D.; Burgin, T. P.; Jones, L.; Allara, D. L.; Tour, J. M.; Weiss, P. S. Are Single Molecular Wires Conducting? *Science* **1996,** *271*, 1705–1707.

(28) Moore, A. M.; Yeganeh, S.; Yao, Y.; Claridge, S. A.; Tour, J. M.; Ratner, M. A.; Weiss, P. S. Polarizabilities of Adsorbed and Assembled Molecules: Measuring the Conductance through Buried Contacts. *ACS Nano* **2010,** *4*, 7630–7636.

(29) Feenstra, R. M.; Stroscio, J. A.; Fein, A. P. Tunneling Spectroscopy of the Si(111)2×1 Surface. *Surf. Sci.* **1987,** *181*, 295–306.

(30) Feenstra, R. M.; Stroscio, J. A.; Tersoff, J.; Fein, A. P. Atom-Selective Imaging of The GaAs(110) Surface. *Phys. Rev. Lett.* **1987,** *58*, 1192–1195.

(31) Hamers, R. J.; Hovis, J. S.; Lee, S.; Liu, H. B.; Shan, J. Formation of Ordered, Anisotropic Organic Monolayers on the Si(001) Surface. *J. Phys. Chem. B* **1997,** *101*, 1489–1492.

(32) Hamers, R. J.; Coulter, S. K.; Ellison, M. D.; Hovis, J. S.; Padowitz, D. F.; Schwartz, M. P.; Greenlief, C. M.; Russell, J. N. Cycloaddition Chemistry of Organic Molecules with Semiconductor Surfaces. *Acc. Chem. Res.* **2000,** *33*, 617–624.

(33) Strother, T.; Cai, W.; Zhao, X. S.; Hamers, R. J.; Smith, L. M. Synthesis and Characterization of DNA-Modified Silicon (111) Surfaces. *J. Am. Chem. Soc.* **2000,** *122*, 1205–1209.

(34) Donhauser, Z. J.; Mantooth, B. A.; Kelly, K. F.; Bumm, L. A.; Monnell, J. D.; Stapleton, J. J.; Price, D. W.; Rawlett, A. M.; Allara, D. L.; Tour, J. M.; Weiss, P. S. Conductance Switching in Single Molecules through Conformational Changes. *Science* **2001,** *292*, 2303–2307.

(35) Yang, W. S.; Auciello, O.; Butler, J. E.; Cai, W.; Carlisle, J. A.; Gerbi, J.; Gruen, D. M.; Knickerbocker, T.; Lasseter, T. L.; Russell, J. N.; Smith, L. M.; Hamers, R. J. DNA-Modified Nanocrystalline Diamond Thin-Films as Stable, Biologically Active Substrates. *Nat. Mater.* **2002,** *1*, 253–257.

(36) Reddick, R. C.; Warmack, R. J.; Ferrell, T. L. New Form of Scanning Optical Microscopy. *Phys. Rev. B* **1989,** *39*, 767–770.

(37) Vigoureux, J. M.; Girard, C.; Courjon, D. General Principles of Scanning Tunneling Optical Microscopy. *Opt. Lett.* **1989,** *14*, 1039–1041.

(38) Reddick, R. C.; Warmack, R. J.; Chilcott, D. W.; Sharp, S. L.; Ferrell, T. L. Photon Scanning Tunneling Microscopy. *Rev. Sci. Instrum.* **1990,** *61*, 3669–3677.

(39) Jiang, S.; Tomita, N.; Ohsawa, H.; Ohtsu, M. A Photon Scanning Tunneling Microscope Using an AlGaAs Laser. *Jpn. J. Appl. Phys.* **1991,** *30*, 2107–2111.

(40) Dawson, P.; de Fornel, F.; Goudonnet, J. P. Imaging of Surface Plasmon Propagation and Edge Interaction Using a Photon Scanning Tunneling Microscope. *Phys. Rev. Lett.* **1994,** *72*, 2927–2930.

(41) Meixner, A. J.; Bopp, M. A.; Tarrach, G. Direct Measurement of Standing Evanescent Waves with a Photon-Scanning Tunneling Microscope. *Appl. Opt.* **1994,** *33*, 7995–8000.

(42) Feldstein, M. J.; Vohringer, P.; Wang, W.; Scherer, N. F. Femtosecond Optical Spectroscopy and Scanning Probe Microscopy. *J. Phys. Chem.* **1996,** *100*, 4739–4748.

(43) Takahashi, S.; Fujimoto, T.; Kato, K.; Kojima, I. High Resolution Photon Scanning Tunneling Microscope. *Nanotechnology* **1997,** *8*, A54–A57.

(44) Kim, H.; Lee, J.; Kahng, S. J.; Son, Y. W.; Lee, S. B.; Lee, C. K.; Ihm, J.; Kuk, Y. Direct Observation of Localized Defect States in Semiconductor Nanotube Junctions. *Phys. Rev. Lett.* **2003,** *90*, 216107.

(45) Ballard, J. B.; Carmichael, E. S.; Shi, D.; Lyding, J. W.; Gruebele, M. Laser Absorption Scanning Tunneling Microscopy of Carbon Nanotubes. *Nano Lett.* **2006,** *6*, 45–49.

(46) Shigekawa, H.; Yoshida, S.; Takeuchi, O.; Aoyama, M.; Terada, Y.; Kondo, H.; Oigawa, H. Nanoscale Dynamics Probed by Laser-Combined Scanning Tunneling Microscopy. *Thin Solid Films* **2008,** *516*, 2348–2357.

(47) Kim, M.; Hohman, J. N.; Cao, Y.; Houk, K. N.; Ma, H.; Jen, A. K. Y.; Weiss, P. S. Creating Favorable Geometries for Directing Organic Photoreactions in Alkanethiolate Monolayers. *Science* **2011,** *331*, 1312–1315.

(48) Atkin, J. M.; Berweger, S.; Jones, A. C.; Raschke, M. B. Nano-Optical Imaging and Spectroscopy of Order, Phases, and Domains in Complex Solids. *Adv. Phys.* **2012,** *61*, 745–842.

(49) Bonnell, D. A.; Basov, D. N.; Bode, M.; Diebold, U.; Kalinin, S. V.; Madhavan, V.; Novotny, L.; Salmeron, M.; Schwarz, U. D.; Weiss, P. S. Imaging Physical Phenomena with Local Probes: From Electrons to Photons. *Rev. Mod. Phys.* **2012,** *84*, 1343–1381.

(50) Nienhaus, L.; Wieghold, S.; Nguyen, D.; Lyding, J. W.; Scott, G. E.; Gruebele, M. Optoelectronic Switching of a Carbon Nanotube Chiral Junction Imaged with Nanometer Spatial Resolution. *ACS Nano* **2015,** *9*, 10563–10570.

(51) Cocker, T. L.; Peller, D.; Yu, P.; Repp, J.; Huber, R. Tracking the Ultrafast Motion of a Single Molecule by Femtosecond Orbital Imaging. *Nature* **2016,** *539*, 263–267.

(52) Nguyen, D.; Nguyen, H. A.; Lyding, J. W.; Gruebele, M. Imaging and Manipulating Energy Transfer Among Quantum Dots at Individual Dot Resolution. *ACS Nano* **2017,** *11*, 6328–6335.

(53) Wang, S.; Wattanatorn, N.; Chiang, N.; Zhao, Y.; Kim, M.; Ma, H.; Jen, A. K. Y.; Weiss, P. S. Photoinduced Charge Transfer in Single-Molecule *p*–*n* Junctions. *J. Phys. Chem. Lett.* **2019,** *10*, 2175–2181.

(54) Eigler, D. M.; Weiss, P. S.; Schweizer, E. K.; Lang, N. D. Imaging Xe with a Low-Temperature Scanning Tunneling Microscope. *Phys. Rev. Lett.* **1991,** *66*, 1189–1192.

(55) Pascual, J. I.; Jackiw, J. J.; Song, Z.; Weiss, P. S.; Conrad, H.; Rust, H. P. Adsorbate-Substrate Vibrational Modes of Benzene on Ag(110) Resolved with Scanning Tunneling Spectroscopy. *Phys. Rev. Lett.* **2001,** *86*, 1050–1053.

(56) Sautet, P.; Joachim, C. Interpretation of STM Images: Copper-Phthalocyanine on Copper. *Surf. Sci.* **1992,** *271*, 387–394.

(57) Chavy, C.; Joachim, C.; Altibelli, A. Interpretation of STM Images: C_{60} on the Gold (110) Surface. *Chem. Phys. Lett.* **1993,** *214*, 569–575.

(58) Vion, D.; Orfila, P. F.; Joyez, P.; Esteve, D.; Devoret, M. H. Miniature Electrical Filters for Single Electron Devices. *J. Appl. Phys.* **1995,** *77*, 2519–2524.

(59) Pascual, J. I.; Gómez-Herrero, J.; Rogero, C.; Baró, A. M.; Sánchez-Portal, D.; Artacho, E.; Ordejón, P.; Soler, J. M. Seeing Molecular Orbitals. *Chem. Phys. Lett.* **2000,** *321*, 78–82.

(60) Villagomez, C. J.; Zambelli, T.; Gauthier, S.; Gourdon, A.; Stojkovic, S.; Joachim, C. STM Images of a Large Organic Molecule Adsorbed on a Bare Metal Substrate or on a Thin Insulating Layer: Visualization of HOMO and LUMO. *Surf. Sci.* **2009,** *603*, 1526–1532.

(61) Puschnig, P.; Boese, A. D.; Willenbockel, M.; Meyer, M.; Lüftner, D.; Reinisch, E. M.; Ules, T.; Koller, G.; Soubatch, S.; Ramsey, M. G.; Tautz, F. S. Energy Ordering of Molecular Orbitals. *J. Phys. Chem. Lett.* **2017,** *8*, 208–213.

(62) Lewis, A.; Isaacson, M.; Harootunian, A.; Muray, A. Development of a 500 Å Spatial Resolution Light Microscope: I. Light is Efficiently Transmitted Through λ/16 Diameter Apertures. *Ultramicroscopy* **1984,** *13*, 227–231.

(63) Pohl, D. W.; Denk, W.; Lanz, M. Optical Stethoscopy: Image Recording with Resolution λ/20. *Appl. Phys. Lett.* **1984,** *44*, 651–653.

(64) Betzig, E.; Trautman, J. K. Near-Field Optics: Microscopy, Spectroscopy, and Surface Modification Beyond the Diffraction Limit. *Science* **1992,** *257*, 189–195.

(65) Novotny, L.; van Hulst, N. Antennas for Light. *Nature Photonics* **2011,** *5*, 83–90.

(66) Pettinger, B.; Schambach, P.; Villagómez, C. J.; Scott, N. Tip-Enhanced Raman Spectroscopy: Near-Fields Acting on a Few Molecules. *Annu. Rev. Phys. Chem.* **2012,** *63*, 379–399.

(67) Alexander, K. D.; Schultz, Z. D. Tip-Enhanced Raman Detection of Antibody Conjugated Nanoparticles on Cellular Membranes. *Anal. Chem.* **2012,** *84*, 7408–7414.

(68) Kazemi-Zanjani, N.; Chen, H.; Goldberg, H. A.; Hunter, G. K.; Grohe, B.; Lagugné-Labarthet, F. Label-Free Mapping of Osteopontin Adsorption to Calcium Oxalate Monohydrate Crystals by Tip-Enhanced Raman Spectroscopy. *J. Am. Chem. Soc.* **2012,** *134*, 17076–17082.

(69) Paulite, M.; Blum, C.; Schmid, T.; Opilik, L.; Eyer, K.; Walker, G. C.; Zenobi, R. Full Spectroscopic Tip-Enhanced Raman Imaging of Single Nanotapes Formed from β-Amyloid(1–40) Peptide Fragments. *ACS Nano* **2013,** *7*, 911–920.

(70) Georgi, C.; Hartschuh, A. Tip-Enhanced Raman Spectroscopic Imaging of Localized Defects in Carbon Nanotubes. *Appl. Phys. Lett.* **2010,** *97*, 143117.

(71) Stadler, J.; Schmid, T.; Zenobi, R. Nanoscale Chemical Imaging of Single-Layer Graphene. *ACS Nano* **2011,** *5*, 8442–8448.

(72) Böhmler, M.; Hartschuh, A. Tip-Enhanced Near-Field Optical Microscopy of Quasi-1 D Nanostructures. *ChemPhysChem* **2012,** *13*, 927–929.

(73) Yano, T.-a.; Ichimura, T.; Kuwahara, S.; H'Dhili, F.; Uetsuki, K.; Okuno, Y.; Verma, P.; Kawata, S. Tip-Enhanced Nano-Raman Analytical Imaging of Locally Induced Strain Distribution in Carbon Nanotubes. *Nat. Commun.* **2013,** *4*, 2592.

(74) Ogawa, Y.; Toizumi, T.; Minami, F.; Baranov, A. V. Nanometer-Scale Mapping of the Strain and Ge Content of Ge/Si Quantum Dots Using Enhanced Raman Scattering by the Tip of an Atomic Force Microscope. *Phys. Rev. B* **2011,** *83*, 081302.

(75) Tallarida, N.; Rios, L.; Apkarian, V. A.; Lee, J. Isomerization of One Molecule Observed through Tip-Enhanced Raman Spectroscopy. *Nano Lett.* **2015,** *15*, 6386–6394.

(76) Lee, J.; Tallarida, N.; Chen, X.; Liu, P.; Jensen, L.; Apkarian, V. A. Tip-Enhanced Raman Spectromicroscopy of Co(II)-Tetraphenylporphyrin on Au(111): Toward the Chemists' Microscope. *ACS Nano* **2017,** *11*, 11466–11474.

(77) Nienhaus, L.; Goings, J. J.; Nguyen, D.; Wieghold, S.; Lyding, J. W.; Li, X. S.; Gruebele, M. Imaging Excited Orbitals of Quantum Dots: Experiment and Electronic Structure Theory. *J. Am. Chem. Soc.* **2015,** *137*, 14743–14750.

(78) Nguyen, D.; Wallum, A.; Nguyen, H. A.; Nguyen, N. T.; Lyding, J. W.; Gruebele, M. Imaging of Carbon Nanotube Electronic States Polarized by the Field of an Excited Quantum Dot. *ACS Nano* **2019,** *13*, 1012–1018.

(79) Nguyen, D.; Goings, J. J.; Nguyen, H. A.; Lyding, J.; Li, X. S.; Gruebele, M. Orientation-Dependent Imaging of Electronically Excited Quantum Dots. *J. Chem. Phys.* **2018,** *148*, 064701.

(80) Nguyen, H. A.; Banerjee, P.; Nguyen, D.; Lyding, J. W.; Gruebele, M.; Jain, P. K. STM Imaging of Localized Surface Plasmons on Individual Gold Nanoislands. *J. Phys. Chem. Lett.* **2018,** *9*, 1970–1976.

(81) Yasuhiko, T.; Masahiro, A.; Hiroyuki, K.; Atsushi, T.; Osamu, T.; Hidemi, S. Ultrafast Photoinduced Carrier Dynamics in GaNAs Probed Using Femtosecond Time-Resolved Scanning Tunnelling Microscopy. *Nanotechnology* **2007,** *18*, 044028.

(82) Shoji, Y.; Yuya, K.; Ryuji, O.; Yoshitaka, O.; Osamu, T.; Hidemi, S. Nanoscale Mapping of Built-in Potential in GaAs p–n Junction Using Light-Modulated Scanning Tunneling Microscopy. *Jpn. J. Appl. Phys.* **2008,** *47*, 6117–6120.

(83) Yoshida, S.; Terada, Y.; Oshima, R.; Takeuchi, O.; Shigekawa, H. Nanoscale Probing of Transient Carrier Dynamics Modulated in a GaAs-PIN Junction by Laser-Combined Scanning Tunneling Microscopy. *Nanoscale* **2012,** *4*, 757–761.

(84) Amer, N. M.; Skumanich, A.; Ripple, D. Photothermal Modulation of the Gap Distance in Scanning Tunneling Microscopy. *Appl. Phys. Lett.* **1986,** *49*, 137–139.

(85) Lyubinetsky, I.; Dohnálek, Z.; Ukraintsev, V. A.; Jr., J. T. Y. Transient Tunneling Current in Laser-Assisted Scanning Tunneling Microscopy. *J. Appl. Phys.* **1997,** *82*, 4115–4117.

(86) Smith, D. A.; Owens, R. W. Laser-Assisted Scanning Tunnelling Microscope Detection of a Molecular Adsorbate. *Appl. Phys. Lett.* **2000,** *76*, 3825–3827.

(87) Gerstner, V.; Thon, A.; Pfeiffer, W. Thermal Effects in Pulsed Laser Assisted Scanning Tunneling Microscopy. *J. Appl. Phys.* **2000,** *87*, 2574–2580.

(88) Grafström, S. Photoassisted Scanning Tunneling Microscopy. *J. Appl. Phys.* **2002,** *91*, 1717–1753.

(89) Dubois, L. H.; Zegarski, B. R.; Nuzzo, R. G. The Chemisorption of Organosulfur Compounds on Gold Surfaces: Construction of Well-Defined Organic Solids. *J. Vac. Sci. Technol., A* **1987,** *5*, 634–635.

(90) Nuzzo, R. G.; Zegarski, B. R.; Dubois, L. H. Fundamental Studies of the Chemisorption of Organosulfur Compounds on Au(111). Implications for Molecular Self-Assembly on Gold Surfaces. *J. Am. Chem. Soc.* **1987,** *109*, 733–740.

(91) Dubois, L. H.; Nuzzo, R. G. Synthesis, Structure, and Properties of Model Organic-Surfaces. *Annu. Rev. Phys. Chem.* **1992,** *43*, 437–463.

(92) Laibinis, P. E.; Nuzzo, R. G.; Whitesides, G. M. Structure of Monolayers Formed by Coadsorption of Two *n*-Alkanethiols of Different Chain Lengths on Gold and Its Relation to Wetting. *J. Phys. Chem.* **1992,** *96*, 5097–5105.

(93) Poirier, G. E.; Tarlov, M. J. The c(4×2) Superlatice of *n*-Alkanethiol Monolayers Self-Assembled on Au(111). *Langmuir* **1994,** *10*, 2853–2856.

(94) Poirier, G. E. Characterization of Organosulfur Molecular Monolayers on Au(111) using Scanning Tunneling Microscopy. *Chem. Rev.* **1997,** *97*, 1117–1128.

(95) Srinivasan, C.; Mullen, T. J.; Hohman, J. N.; Anderson, M. E.; Dameron, A. A.; Andrews, A. M.; Dickey, E. C.; Horn, M. W.; Weiss, P. S. Scanning Electron Microscopy of Nanoscale Chemical Patterns. *ACS Nano* **2007,** *1*, 191–201.

(96) Ulman, A. Formation and Structure of Self-Assembled Monolayers. *Chem. Rev.* **1996,** *96*, 1533–1554.

(97) Gooding, J. J.; Ciampi, S. The Molecular Level Modification of Surfaces: From Self-Assembled Monolayers to Complex Molecular Assemblies. *Chem. Soc. Rev.* **2011,** *40*, 2704–2718.

(98) Claridge, S. A.; Liao, W.-S.; Thomas, J. C.; Zhao, Y.; Cao, H. H.; Cheunkar, S.; Serino, A. C.; Andrews, A. M.; Weiss, P. S. From the Bottom Up: Dimensional Control and Characterization in Molecular Monolayers. *Chem. Soc. Rev.* **2013,** *42*, 2725–2745.

(99) Smith, R. K.; Lewis, P. A.; Weiss, P. S. Patterning Self-Assembled Monolayers. *Prog. Surf. Sci.* **2004,** *75*, 1–68.

(100) Love, J. C.; Estroff, L. A.; Kriebel, J. K.; Nuzzo, R. G.; Whitesides, G. M. Self-Assembled Monolayers of Thiolates on Metals as a Form of Nanotechnology. *Chem. Rev.* **2005,** *105*, 1103–1169.

(101) Saavedra, H. M.; Mullen, T. J.; Zhang, P. P.; Dewey, D. C.; Claridge, S. A.; Weiss, P. S. Hybrid Strategies in Nanolithography. *Rep. Prog. Phys.* **2010,** *73*, 036501.

(102) Venkataraman, L.; Klare, J. E.; Nuckolls, C.; Hybertsen, M. S.; Steigerwald, M. L. Dependence of Single-Molecule Junction Conductance on Molecular Conformation. *Nature* **2006,** *442*, 904–907.

(103) Bent, S. F. Heads or Tails: Which Is More Important in Molecular Self-Assembly? *ACS Nano* **2007,** *1*, 10–12.

(104) McGuiness, C. L.; Blasini, D.; Masejewski, J. P.; Uppili, S.; Cabarcos, O. M.; Smilgies, D.; Allara, D. L. Molecular Self-Assembly at Bare Semiconductor Surfaces: Characterization of a Homologous Series of *n*-Alkanethiolate Monolayers on GaAs(001). *ACS Nano* **2007,** *1*, 30–49.

(105) Scholz, F.; Kaletová, E.; Stensrud, E. S.; Ford, W. E.; Kohutová, A.; Mucha, M.; Stibor, I.; Michl, J.; von Wrochem, F. Formation of *n*-Alkyl Monolayers by Organomercury Deposition on Gold. *J. Phys. Chem. Lett.* **2013,** *4*, 2624–2629.

(106) Liao, K.-C.; Yoon, H. J.; Bowers, C. M.; Simeone, F. C.; Whitesides, G. M. Replacing $Ag^{TS}SCH_2$-R with $Ag^{TS}O_2C$-R in EGaIn-Based Tunneling Junctions Does Not Significantly Change Rates of Charge Transport. *Angew. Chem. Int. Ed.* **2014,** *53*, 3889–3893.

(107) De Feyter, S.; De Schryver, F. C. Two-Dimensional Supramolecular Self-Assembly Probed by Scanning Tunneling Microscopy. *Chem. Soc. Rev.* **2003,** *32*, 139–150.

(108) Theobald, J. A.; Oxtoby, N. S.; Phillips, M. A.; Champness, N. R.; Beton, P. H. Controlling Molecular Deposition and Layer Structure with Supramolecular Surface Assemblies. *Nature* **2003,** *424*, 1029–1031.

(109) Desiraju, G. R. Crystal Engineering: From Molecule to Crystal. *J. Am. Chem. Soc.* **2013,** *135*, 9952–9967.

(110) Barth, J. V. Molecular Architectonic on Metal Surfaces. *Annu. Rev. Phys. Chem.* **2007,** *58*, 375–407.

(111) Georgakilas, V.; Tiwari, J. N.; Kemp, K. C.; Perman, J. A.; Bourlinos, A. B.; Kim, K. S.; Zboril, R. Noncovalent Functionalization of Graphene and Graphene Oxide for Energy Materials, Biosensing, Catalytic, and Biomedical Applications. *Chem. Rev.* **2016,** *116*, 5464–5519.

(112) Bumm, L. A.; Arnold, J. J.; Charles, L. F.; Dunbar, T. D.; Allara, D. L.; Weiss, P. S. Directed Self-Assembly to Create Molecular Terraces with Molecularly Sharp Boundaries in Organic Monolayers. *J. Am. Chem. Soc.* **1999,** *121*, 8017–8021.

(113) Weiss, P. S. Functional Molecules and Assemblies in Controlled Environments: Formation and Measurements. *Acc. Chem. Res.* **2008,** *41*, 1772–1781.

(114) Zheng, Y. B.; Pathem, B. K.; Hohman, J. N.; Thomas, J. C.; Kim, M.; Weiss, P. S. Photoresponsive Molecules in Well-Defined Nanoscale Environments. *Adv. Mater.* **2013,** *25*, 302–312.

(115) Donhauser, Z. J.; Price, D. W.; Tour, J. M.; Weiss, P. S. Control of Alkanethiolate Monolayer Structure Using Vapor-Phase Annealing. *J. Am. Chem. Soc.* **2003,** *125*, 11462–11463.

(116) Cygan, M. T.; Dunbar, T. D.; Arnold, J. J.; Bumm, L. A.; Shedlock, N. F.; Burgin, T. P.; Jones, L.; Allara, D. L.; Tour, J. M.; Weiss, P. S. Insertion, Conductivity, and Structures of Conjugated Organic Oligomers in Self-Assembled Alkanethiol Monolayers on Au{111}. *J. Am. Chem. Soc.* **1998,** *120*, 2721–2732.

(117) Moore, A. M.; Mantooth, B. A.; Donhauser, Z. J.; Maya, F.; Price, D. W.; Yao, Y. X.; Tour, J. M.; Weiss, P. S. Cross-Step Place-Exchange of Oligo(phenylene-ethynylene) Molecules. *Nano Lett.* **2005,** *5*, 2292–2297.

(118) Kumar, A. S.; Ye, T.; Takami, T.; Yu, B. C.; Flatt, A. K.; Tour, J. M.; Weiss, P. S. Reversible Photo-Switching of Single Azobenzene Molecules in Controlled Nanoscale Environments. *Nano Lett.* **2008,** *8*, 1644–1648.

(119) Kim, M.; Hohman, J. N.; Morin, E. I.; Daniel, T. A.; Weiss, P. S. Self-Assembled Monolayers of 2-Adamantanethiol on Au{111}: Control of Structure and Displacement. *J. Phys. Chem. A* **2009,** *113*, 3895–3903.

(120) Lewis, P. A.; Inman, C. E.; Yao, Y.; Tour, J. M.; Hutchison, J. E.; Weiss, P. S. Mediating Stochastic Switching of Single Molecules Using Chemical Functionality. *J. Am. Chem. Soc.* **2004,** *126*, 12214–12215.

(121) Moore, A. M.; Mantooth, B. A.; Donhauser, Z. J.; Yao, Y.; Tour, J. M.; Weiss, P. S. Real-Time Measurements of Conductance Switching and Motion of Single Oligo(phenylene ethynylene) Molecules. *J. Am. Chem. Soc.* **2007,** *129*, 10352–10353.

(122) Zheng, Y. B.; Payton, J. L.; Chung, C.-H.; Liu, R.; Cheunkar, S.; Pathem, B. K.; Yang, Y.; Jensen, L.; Weiss, P. S. Surface-Enhanced Raman Spectroscopy to Probe Reversibly Photoswitchable Azobenzene in Controlled Nanoscale Environments. *Nano Lett.* **2011,** *11*, 3447–3452.

(123) Zhao, Y. Interface Properties of Functional Molecules on Au{111}: From Photoinduced Charge Transfer to Exchange Reactions. Ph.D. Dissertation, University of California, Los Angeles, CA, 2014.

(124) Ferris, J. H.; Kushmerick, J. G.; Johnson, J. A.; Youngquist, M. G. Y.; Kessinger, R. B.; Kingsbury, H. F.; Weiss, P. S. Design, Operation, and Housing of an Ultrastable, Low

Temperature, Ultrahigh Vacuum Scanning Tunneling Microscope. *Rev. Sci. Instrum.* **1998,** *69*, 2691–2695.

(125) Kästle, G.; Boyen, H. G.; Koslowski, B.; Plettl, A.; Weigl, F.; Ziemann, P. Growth of Thin, Flat, Epitaxial (111) Oriented Gold Films on c-Cut Sapphire. *Surf. Sci.* **2002,** *498*, 168–174.

(126) Wildes, A. R.; Mayer, J.; Theis-Bröhl, K. The Growth and Structure of Epitaxial Niobium on Sapphire. *Thin Solid Films* **2001,** *401*, 7–34.

(127) Wagner, T. High Temperature Epitaxial Growth and Structure of Nb Films on α–Al_2O_3(0001). *J. Mater. Res.* **2011,** *13*, 693–702.

(128) Gutekunst, G.; Mayer, J.; Rühle, M. Atomic Structure of Epitaxial Nb-Al_2O_3 Interfaces I. Coherent Regions. *Philos. Mag. A* **1997,** *75*, 1329–1355.

(129) Wildes, A. R.; Cowley, R. A.; Ward, R. C. C.; Wells, M. R.; Jansen, C.; Wireen, L.; Hill, J. P. The Structure of Epitaxially Grown Thin Films: A Study of Niobium on Sapphire. *J. Phys.: Condens. Matter* **1998,** *10*, L631–L637.

(130) Kitada, M. Reactions in Au/Nb Bilayer Thin Films. *Thin Solid Films* **1994,** *250*, 111–114.

CHAPTER 2

Photo-Induced Charge Transfer in Single Molecule *p-n* Junctions

(Adapted From: Wang, S.; Wattanatorn, N.; Chiang, N.; Zhao, Y.; Kim, M.; Ma, H.; Jen, A. K. Y.; Weiss, P. S. Photoinduced Charge Transfer in Single-Molecule *p–n* Junctions. *J. Phys. Chem. Lett.* **2019,** *10*, 2175–2181.)

2.1 Introduction

Fullerenes and their derivatives are promising components of photovoltaics due to their high degree of π-electron delocalization.[1-3] A number of molecular dyads, triads, and tetrads of fullerenes covalently linked to electron donors, such as porphyrins, phthalocyanines, tetrathiafulvalenes, ferrocenes, and other moieties, have been synthesized and intensively studied.[4-7] These fullerene donor-linked compounds exhibit excellent photovoltaic efficiencies upon illumination.[8-10] Furthermore, enhancements of nonlinear optical responses were observed for fullerene dyads compared to those of pristine fullerenes.[6,7] C_{60}-tethered 2,5-dithienylpyrrole triad (C_{60} triad, Figure 2.1a) has C_{60} groups attached to both ends of an electron-rich chromophore and a rigid backbone provides a stable and conducting tether.[9] This donor-acceptor triad structure makes light harvesting more efficient, resulting in large photocurrents, as observed in photoelectrochemical cells. Here, we used our custom-built laser-assisted STM (photon STM)[11] to measure photoinduced charge generation and separation in single-molecule triads isolated in *n*-dodecanethiolate self-assembled monolayers under ambient conditions. Built-in control experiments test that the observed signals are due to photoconductance. These controls include measuring the photoconductance of the (non-absorbing) matrix and "dummy" inserted chromophores with similar chemical structures but no significant absorption spectra at the excitation wavelength. In this way, we consistently test for the thermal effects of sample and STM tip heating (without changing samples[11]), either or both of which could affect the tunneling current and spectra. With the submolecular resolution of STM, we can detect local spectral changes rather than integrating over large areas. Thus, we are able to elucidate the effects

of the local environment and ultimately target optimized supramolecular assemblies that maximize photon absorption and energy conversion efficiency.

2.2 Experimental Methods

We used vapor-deposited *n*-dodecanethiolate (C12) self-assembled monolayers (SAMs) on sapphire-prism-supported Au{111} as the two-dimensional matrix, and inserted photoactive molecules into the defects in C12 SAMs so that they can be studied at the single molecular level.[12,13] The C_{60}-tethered 2,5-dithienylpyrrole triads (C_{60} triads, Figure 2.1a) and the control molecules without the C_{60} moieties (DTP, Figure 2.1b) were synthesized following previously reported procedures[9] and were inserted into the defects in C12 SAMs through solution deposition.[14,15]

2.2.1 Preparation of *n*-Dodecanethiolate Self-Assembled Monolayer Matrices

Freshly flame-annealed Au{111}/Al_2O_3(0001) substrates were placed in the airspace in a vial over gravimetrically prepared 1 mM *n*-dodecanethiol (Sigma Aldrich, St. Louis, MO) ethanolic solution for 3 h at 78 ℃. Substrates were then rinsed thoroughly with ethanol and were blown dry using nitrogen.

2.2.2 Insertion of C_{60}-tethered 2,5-dithienylpxyrrole triads (C_{60} triads) and control molecules without C_{60} (DTP) into *n*-dodecanethiolate self-assembled monolayer matrices.

With ultrasonication to speed up the dissolution, the solution of 2,5-dithienylpyrrole with conjugated tether (DTP, 0.05 mM, 10 mL) in toluene (HPLC purity) was prepared and purged with dry nitrogen. Ammonium hydroxide (28.0-30.0% NH_3, 5 μL) was added to 1 mL of the solution. The aqueous ammonia hydrolyzed the thioacetyl protecting group, generating the thiolate *in situ*. After 2 min ultrasonication to mix ammonium hydroxide with toluene solution, the mixture was

let stand for 30 min for deprotection before use. Monolayers with DTP inserted were prepared by submerging the gold substrate with vapor-deposited dodecanethiol SAM matrix into solution of deprotected DTP molecules overnight at room temperature. The solution of C_{60} triad (0.05 mM, 10 mL) in toluene (HPLC purity) was ultrasonicated and bubbled with dry nitrogen. The partial solution (2 mL) were transferred into a vial and diluted with 0.25 mL of ethanol to ease the dissolution of ammonium hydroxide. Two doses of ammonium hydroxide (28.0-30.0% NH_3, 25 μL) were added with 3 min sonication in between. After the solution was stirred for 0.5 h, the Au substrates were immersed into the solution for 24 h, followed by rinsing with toluene and ethanol, and drying with a nitrogen stream. The color of the solution turning to light brown indicates that the acetate protecting group has been removed.

2.3 Results and Discussion

2.3.1 Photo-Response of the C_{60} Triad

Consecutively obtained topographic images of the same region and simultaneously acquired spectroscopic images are shown in Figure 2.2. The chopper wheel was turned on throughout the data collection process to ensure that all phase-sensitive signals were acquired with the same reference frequency of 4.8 kHz. The laser illumination was blocked for Figure 2.2a,b and was on for Figure 2.2c-f. The lattice structures in Figure 2.2a,c,e reflect the C12 matrix molecules and the protrusions represent C_{60} moieties in C_{60} triad molecules. Each C_{60} triad molecule has two C_{60} groups, but they are not symmetrically arranged because of the conformations of the molecules (even though the molecules are *topologically* symmetric), so that in each molecule, one of C_{60} feature appears less protruding or does not even appear in the topographic images. This difference is the result of STM images being convolutions of geometric and electronic structure.[16-19]

For example, in the area shown in Figure 2.2a,c,e, we observe five C_{60} triad molecules, as labeled in Figure 2.2c. The lattice structures of C12 SAMs in Figure 2.2a,c,e are not observed in the spectroscopic images under these conditions. This result is consistent with C12 not absorbing incident photons at this energy, leading to no detectable photocurrent corresponding to the excitation. By comparing Figure 2.2b,d,f we can see that there are large positive and negative signals in the lower regions of Figure 2.2d,f (illuminated) that were *not* observed in Figure 2.2b (no illumination). Such positive and negative signals are much larger than the background and *only* present under illumination.

Schemes showing the experimental setup are shown in Figure 2.3a. We use phase-sensitive detection with mechanical chopping of the laser illumination to record the photo-induced tunneling current change (Figs. 2b,d,f and 3b). In Figure 2.3b, while under illumination, the average values of the in-phase signals calculated from Figure 2.2d,f (and other consecutively collected spectroscopic images not shown here) are more negative than those without illumination. The number n in Figure 2.3b represents the number of spectroscopic images we used to calculate the average values. The average values of Figure 2.2d,f and other spectroscopic images collected under illumination were calculated from the regions corresponding to dodecanethiol molecules only (highlighted in Figure 2.4). The error bars represent the deviation of average values between different images. When we change the sample bias from -1 V to +1 V, we observe that, under illumination, the average in-phase signal is more positive than that without illumination. That is, the phase shift for photo-induced signal changes 180° when we change the polarity of the bias. We attribute the negative shift of *average* in-phase signal under illumination in Figure 2.3b to tunneling of photo-induced hot electrons from the surface to the tip. Since photo-induced electrons

generated in C_{60} triad molecules should have the same phase shift as hot electrons, in Figure 2.2, we conclude that local positive signals in the spectroscopic images indicate that the position has higher densities of photo-induced holes and negative signals in the spectroscopic images indicate that the position has higher densities of photo-generated electrons.[20-23] Our results in Figure 2.2 and related data enable us to characterize the distribution of photo-induced charges *within* C_{60} triad molecules.

Photoinduced signals in the phase-sensitive spectroscopic images in Figure 2.2d,f were extracted from the background through a height thresholding method. Height thresholds were determined based on the data intensity range of the area corresponding to *n*-dodecanethiol matrix molecules in phase-sensitive spectroscopic images, as highlighted in Figure 2.4. Figure 2.4a,b is reproduced from Figure 2.2d,f. For Figure 2.2d, data points with value smaller than -1.2 pA and larger than 0.9 pA and their adjacent areas with slope larger than 20% of the whole image and curvature larger than 60% of the whole image were conserved. The rest of the data points in Figure 2.2d were replaced by the mean value of the whole image. For Figure 2.2f, data points with values smaller than -0.9 pA and larger than 0.8 pA and their adjacent areas with slope larger than 20% of the whole image and curvature larger than 60% of the whole image were conserved. The rest of the data points in Figure 2.2f were replaced by the mean value of the entire image.

Extracted photo-induced signals from Figure 2.2d,f are shown in Figure 2.5b,e separately and corresponding topographic images Figure 2.2c,e are shown as Figure 2.5a,d for analysis. In the data in Figure 2.5b, we find that the three regions of signals highlighted by black, green, and red boxes correspond to the C_{60} triad molecules labeled 2, 3, and 5, respectively, in Figure 2.5a. While in Figure 2.5e, the two regions of signals highlighted by green and red boxes correspond to the

C_{60} triad molecules labeled 3, 4, and 5, respectively, in Figure 2.5d. The relative intensities of the photo-induced signals can also be seen in Figure 2.5c,f, which are displays of Figure 2.5b,e in the yz plane. The signals corresponding to the molecule labeled 2 (black box) in Figure 2.5c disappear in Figure 4f and the signal corresponding to the molecule labeled 3 (green box) in Figure 2.5c only have positive signal left in Figure 2.5f and the intensity has greatly decreased. However, the signal corresponding to the molecule labeled 5 (red box) in Figure 2.5c greatly increased in Figure 2.5f. We tentatively attribute the differences in the intensities of photo-induced signals and the observations that photo-induced signals were not observed for all C_{60} triad molecules as likely due to (dynamic) differences in conformations of C_{60} triad molecules.

We observed that in Figures 2.2 and 2.5, the regions with large phase-sensitive signals in the spectroscopic images correspond to the regions with strips with significant signal fluctuations in the topographic images. The strips in the topographic images were caused by the conformational changes and motion of C_{60} triad molecules during scanning. In order to test whether the phase-sensitive signals we observed were related to motion of the molecules, we collected another set of images of the same region when the surface was not under illumination, shown in Figure 2.6. In Figure 2.6a, we observe signal fluctuations near one of the C_{60} triad molecules, which we interpret as conformational changes and motion of the C_{60} triad molecules not being caused (exclusively) by illumination. In the corresponding spectroscopic image, Figure 2.6b, we do not observe significant phase-sensitive signals in the region corresponding to the fluctuations, indicating that the movement of the C_{60} triad molecules will not generate “mechanical” noise in the spectroscopic images as recorded (which would have to be phase-sensitive to be observed).

Such results suggest that the phase-sensitive signals we observed in Figures 2.2 and 2.5 were caused by the photo-induced charges.

In order to test whether we can detect the distribution of photo-induced charges on different C_{60} triad molecules, we also collected topographic and spectroscopic images for different regions on different samples. Two typical sets of data are shown in Figures 2.7 and 2.8. Figure 2.7a,b was collected without any illumination and Figure 2.7c,d was collected when the surface was illuminated by a 405 nm laser. In Figure 2.7d, we observe positive and negative in-phase signals (highlighted by the black box) corresponding to the position of a C_{60} triad molecule in Figure 2.7c. Such signals were *not* observed in Figure 2.7b. All images in Figure 2.8 were collected with a +1.00 V sample bias, which is different from all the other STM images shown in the main text and the supporting information. Figure 2.8a,b was collected without any illumination and Figure 2.8c,d was collected when the surface was illuminated by a 405 nm laser. Photo-induced signals were observed in Figure 2.8d (highlighted by the black box) and their positions correlate to the positions of C_{60} triad molecules in Figure 2.8c.

We also collected the 90° phase offset images for Figure 2.2c,e, shown as Figure 2.9c,f, separately. Figure 2.2c,d,e,f is reproduced as Figure 2.9a,b,d,e for comparison. In Figure 2.9c,f, we observe positive and negative phase-sensitive signals at the same positions as Figure 2.9b,e. The phase shift of the phase-sensitive signal only depends on the electronic delays of the system and is constant as long as the settings of the chopper encoder and lock-in amplifier are kept the same. It can vary within a small range due electronic noise and small uncertainties of the instruments (vibrations *etc.*) resulting in small signals in the 90° phase offset images. The purpose of this work is to test if we can map the distributions of photo-induced charges at the sub-molecular

level. We have the potential to obtain more valuable information after further engineering of the instrument and the systems.

2.3.2 Photo-Response of the Control Molecule (DTP)

We also performed control experiments in which molecules *without* C_{60} groups (DTP, Figure 1b) were inserted into the defects in C12 SAMs and the surface was characterized by laser-assisted STM. Figure 2.10a,b shows simultaneously obtained topographic and spectroscopic images without illumination. Figure 2.10c,d shows simultaneously obtained topographic and spectroscopic images with evanescent laser illumination. We attribute the protrusions in Figure 2.10a,c highlighted by the circles as DTP molecules. The DTP molecules cannot be characterized as clearly as C_{60} triad molecules even though the lattice of C12 matrix molecules is still observed. We attribute this difference to DTP molecules being substantially smaller than C_{60} triad molecules, which makes them more mobile under ambient conditions and room temperature.[24] When the laser was blocked to stop illumination, some signals near the background level were observed in Figure 2.10b at the same position as the DTP molecule in Figure 2.10a. After illumination, the signal corresponding to the DTP molecule (highlighted by the circle) in the spectroscopic image Figure 2.10d did *not* increase significantly beyond the background (matrix) level. These and similar results on DTP and other molecules indicate that the charge separation observed in Figure 2.2d,f is only observed in molecular *p-n* junctions when both electron donor and electron acceptors are present.

2.4 Conclusions and Prospects

In summary, we have successfully detected photoinduced charge separation in single molecular *p-n* junctions with laser-assisted STM. This method can serve as a diagnostic tool to measure the

intrinsic photovoltaic efficiency of single molecules and assemblies for solar cell applications. By investigating candidate molecules and assemblies with this laser-assisted STM, we can quantitatively compare the photovoltaic efficiency with submolecular resolution and provide direct figures of merit for energy conversion. We can use these measurements to optimize photoabsorption, charge separation, and connections of the molecules or assemblies to the contact. The critical details of the orientations and contacts can be extracted in a way inaccessible to ensemble measurements of photovoltaics. These studies will provide important design principles and feedback for synthetic chemists, and help to determine key molecular components for efficient light conversion. Further experiments will focus on extending our method to other photoactive molecules with different electron donors and acceptors and molecules/assemblies with different structures.

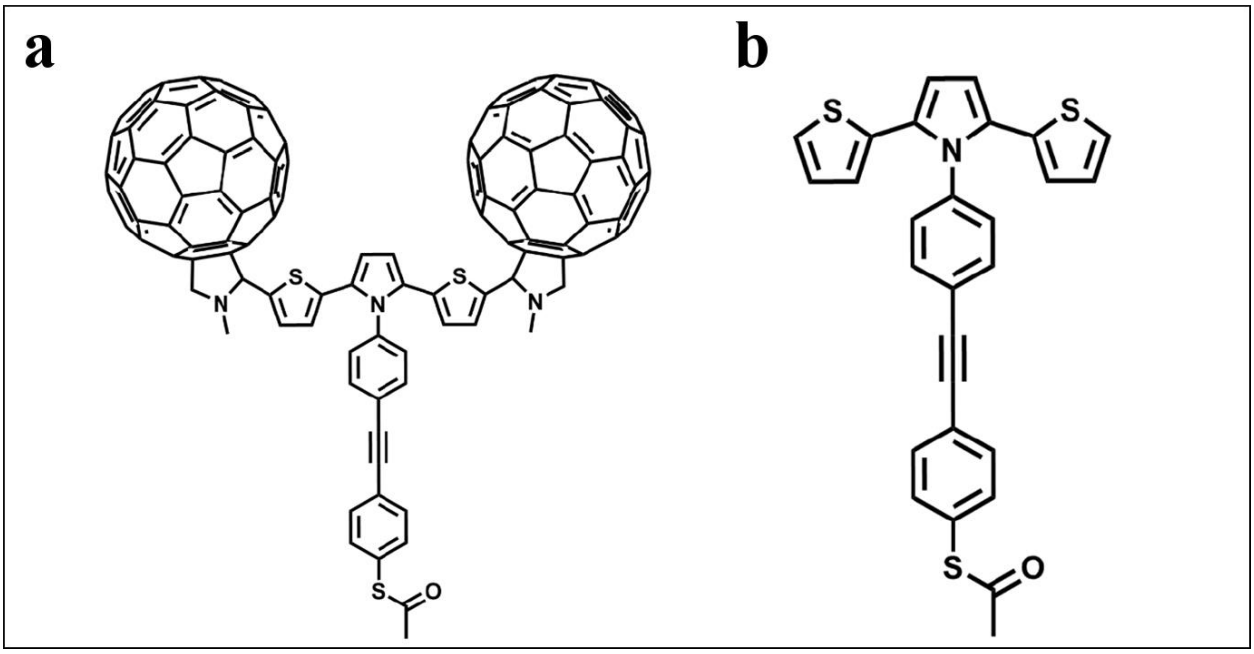

Figure 2.1. Chemical structure of (a) C_{60}-tethered 2,5-dithienylpyrrole triad and (b) the control that has no C_{60} attached (DTP).

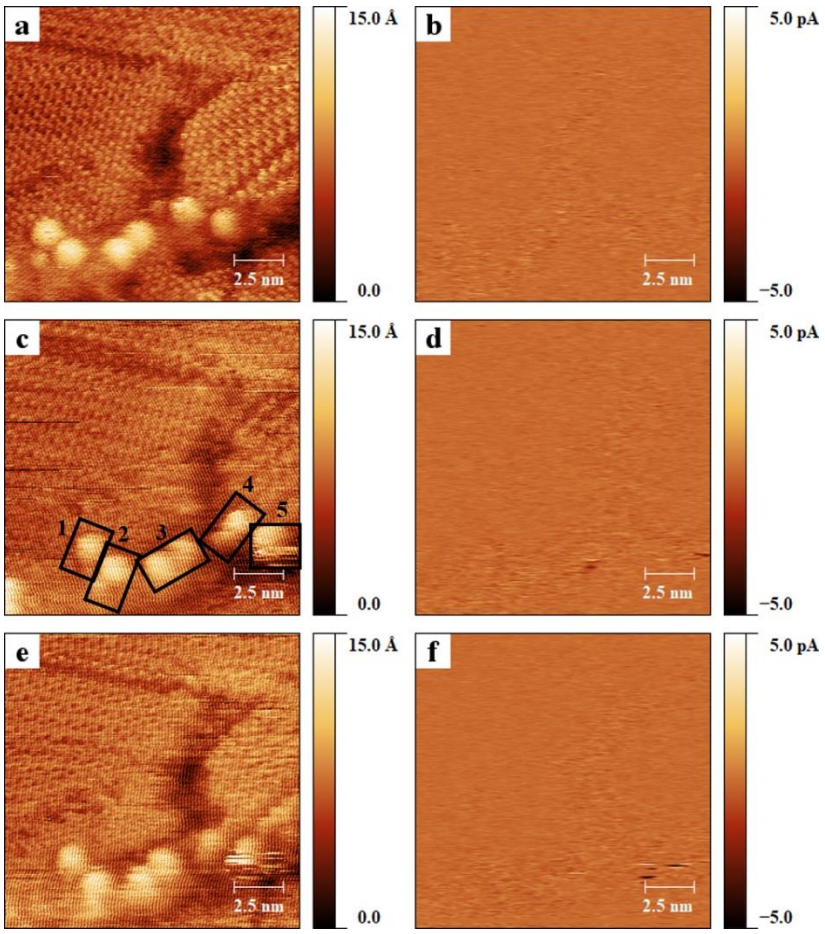

Figure 2.2. Consecutively collected scanning tunneling microscopy images showing C_{60} triad molecules inserted in dodecanethiolate monolayer matrix on Au{111}. (a) Topographic and (b) spectroscopic (see text) images were simultaneously obtained when the laser was not illuminating the sample. (c) Topographic and (d) spectroscopic images were simultaneously obtained when the laser illuminated the sample evanescently. (e) Topographic and (f) spectroscopic images were simultaneously obtained immediately after (c) and (d). All images were collected at a sample bias of -1.00 V and a tunneling current of 12.0 pA. All spectroscopic images were collected phase-sensitively with a reference frequency of 4.8 kHz created by a chopper wheel that was used to modulate the evanescent sample illumination.

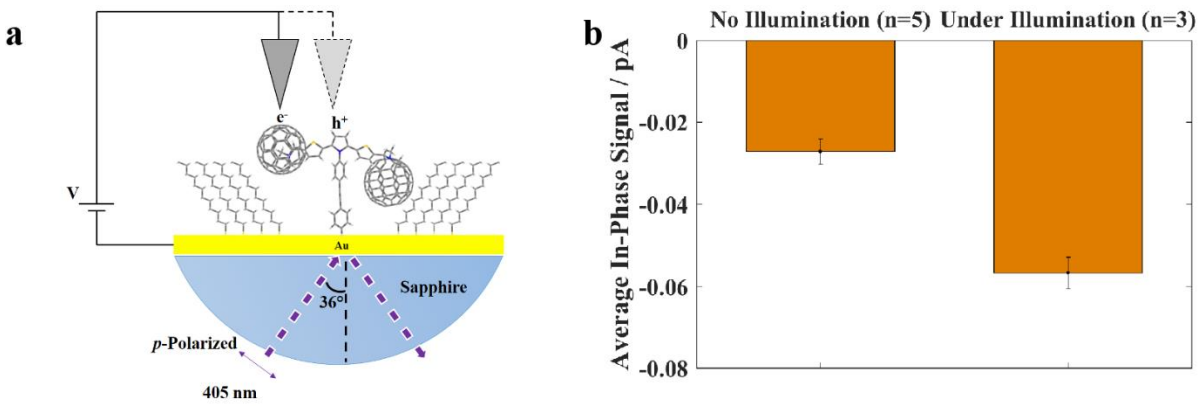

Figure 2.3. (a) Scheme of evanescent illumination and photo-generation of charge separation, measured in submolecular resolution spectroscopic images. (b) Average of the in-phase signals calculated from spectroscopic images in Figure 2.2 and consecutively collected data.

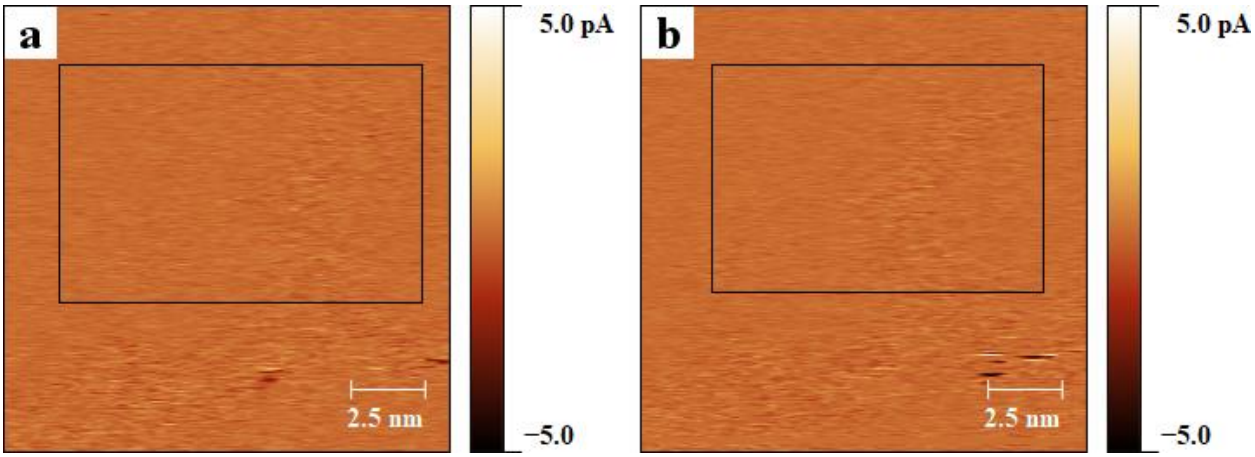

Figure 2.4. (a) Phase-sensitive spectroscopic image reproduced from Figure 2.2d. (b) Phase-sensitive spectroscopic image reproduced from Figure 2.2f.

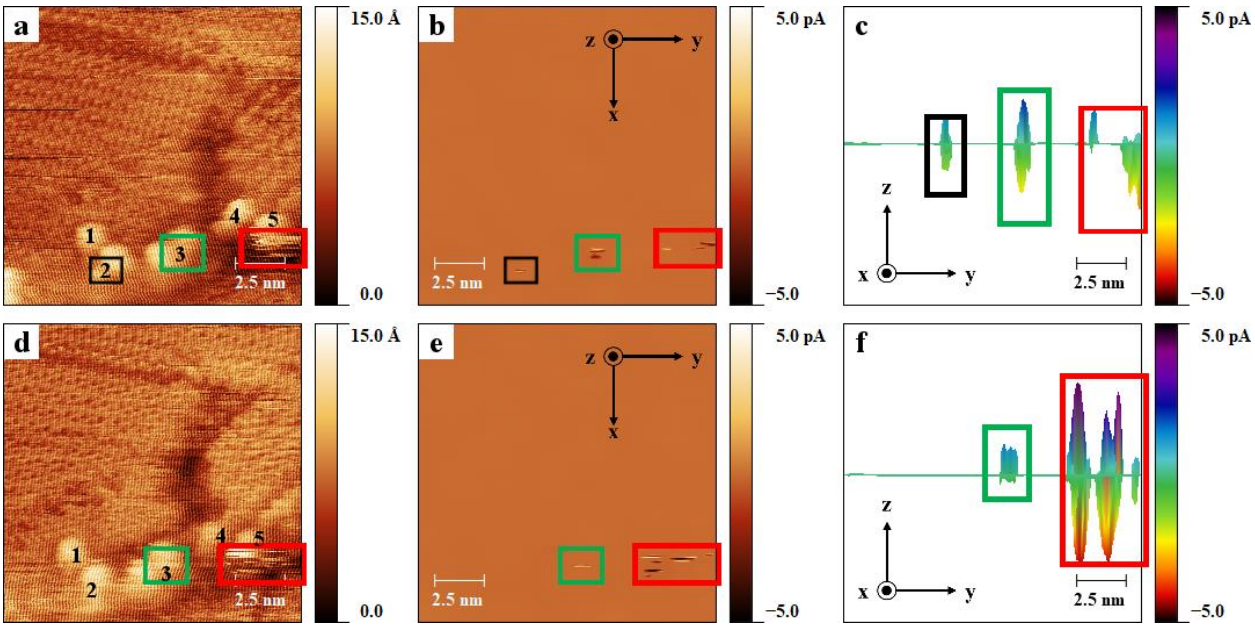

Figure 2.5. Consecutively collected scanning tunneling microscopy images under evanescent laser illumination, showing C_{60} triad molecules inserted in a dodecanethiolate monolayer matrix on Au{111}. (a) Topographic image reproduced from Figure 2.2c. (b) Photo-induced charge separation extracted from Figure 2.2d. (c) Projection of image (b) on the yz plane. (d) Topographic image reproduced from Figure 2.2e. (e) Photo-induced charge separation extracted from Figure 2.2f. (d) Projection of image (e) in the yz plane. All images were collected at a sample bias of -1.00 V and a tunneling current of 12.0 pA. All spectroscopic images were collected phase-sensitively with a reference frequency of 4.8 kHz created by a chopper wheel that was used to modulate the sample illumination.

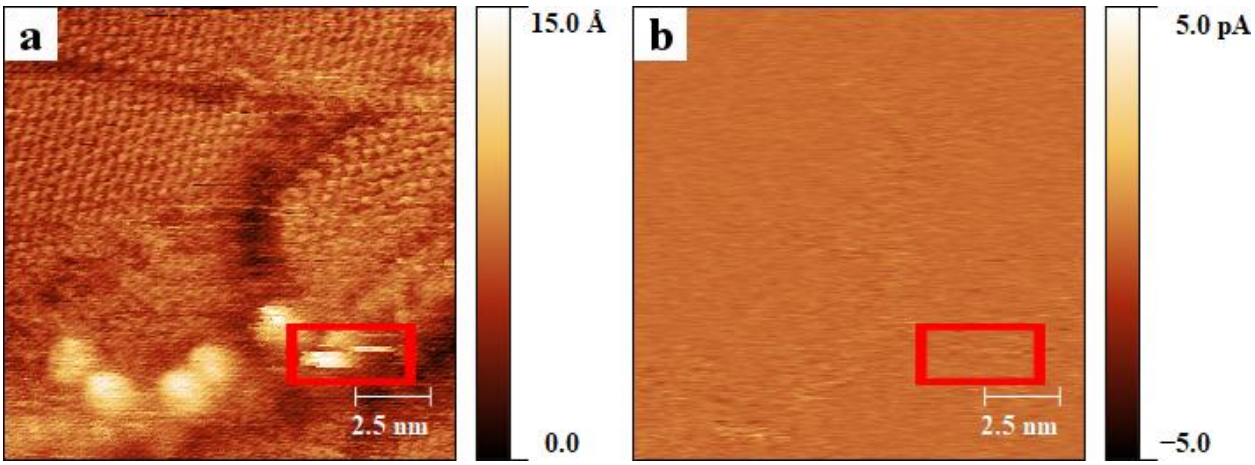

Figure 2.6. (a) Topographic and (b) spectroscopic images showing C_{60} triad molecules inserted in dodecanethiolate monolayer matrix on Au{111}. Images were collected without any illumination of the surface. All images were collected at a sample bias of -1.00 V and a tunneling current of 12.0 pA.

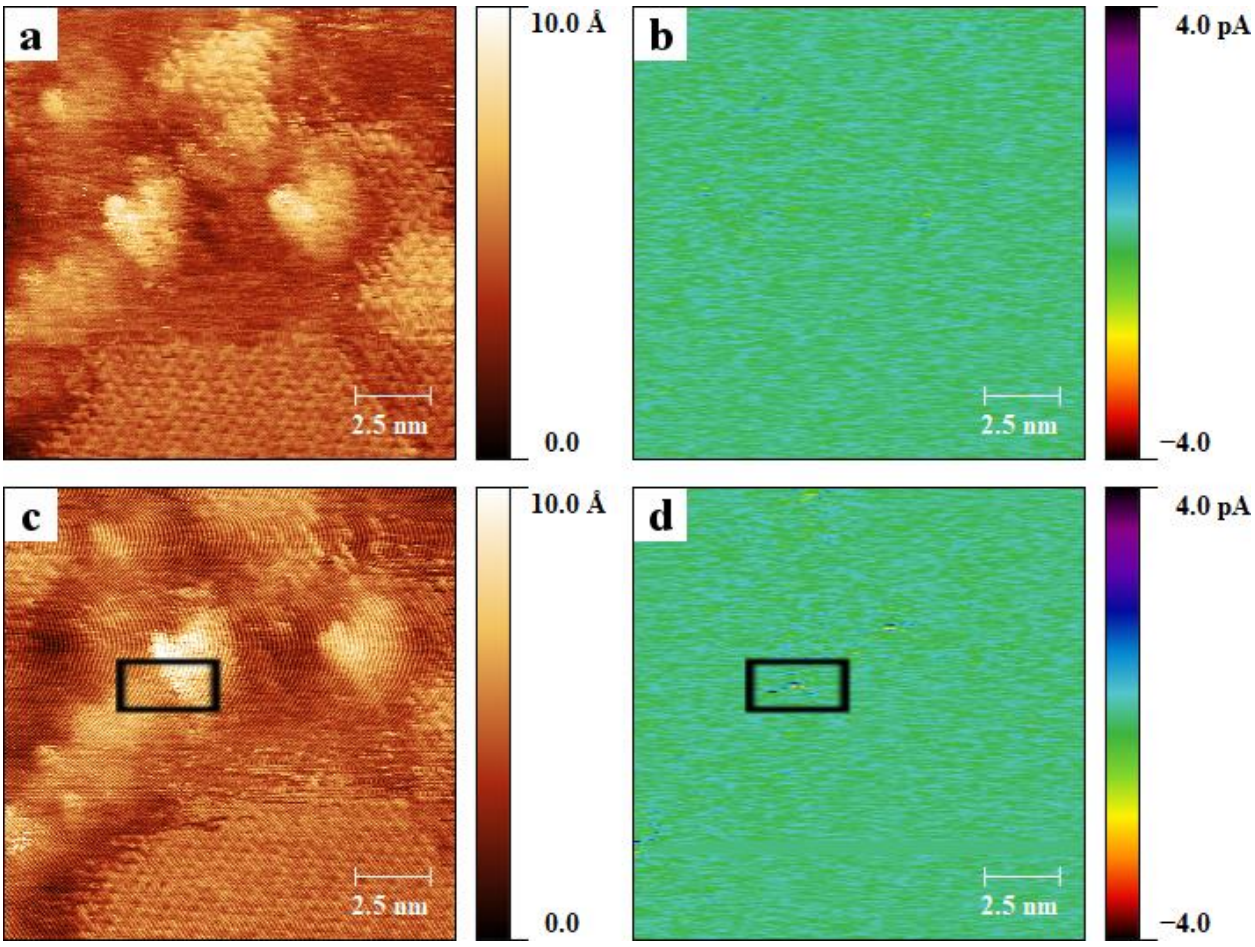

Figure 2.7. Scanning tunneling microscopy images showing C_{60} triad molecules inserted in a dodecanethiolate monolayer matrix on Au{111}. (a) Topographic and (b) spectroscopic images were simultaneously obtained when the laser was not illuminating the sample. (c) Topographic and (d) spectroscopic images were simultaneously obtained when the laser (405 nm) illuminated the sample evanescently. All images were collected at a sample bias of -1.00 V and a tunneling current of 12.0 pA. All spectroscopic images were collected phase-sensitively with a reference frequency of 4.8 kHz created by a chopper wheel that was used to modulate the evanescent sample illumination.

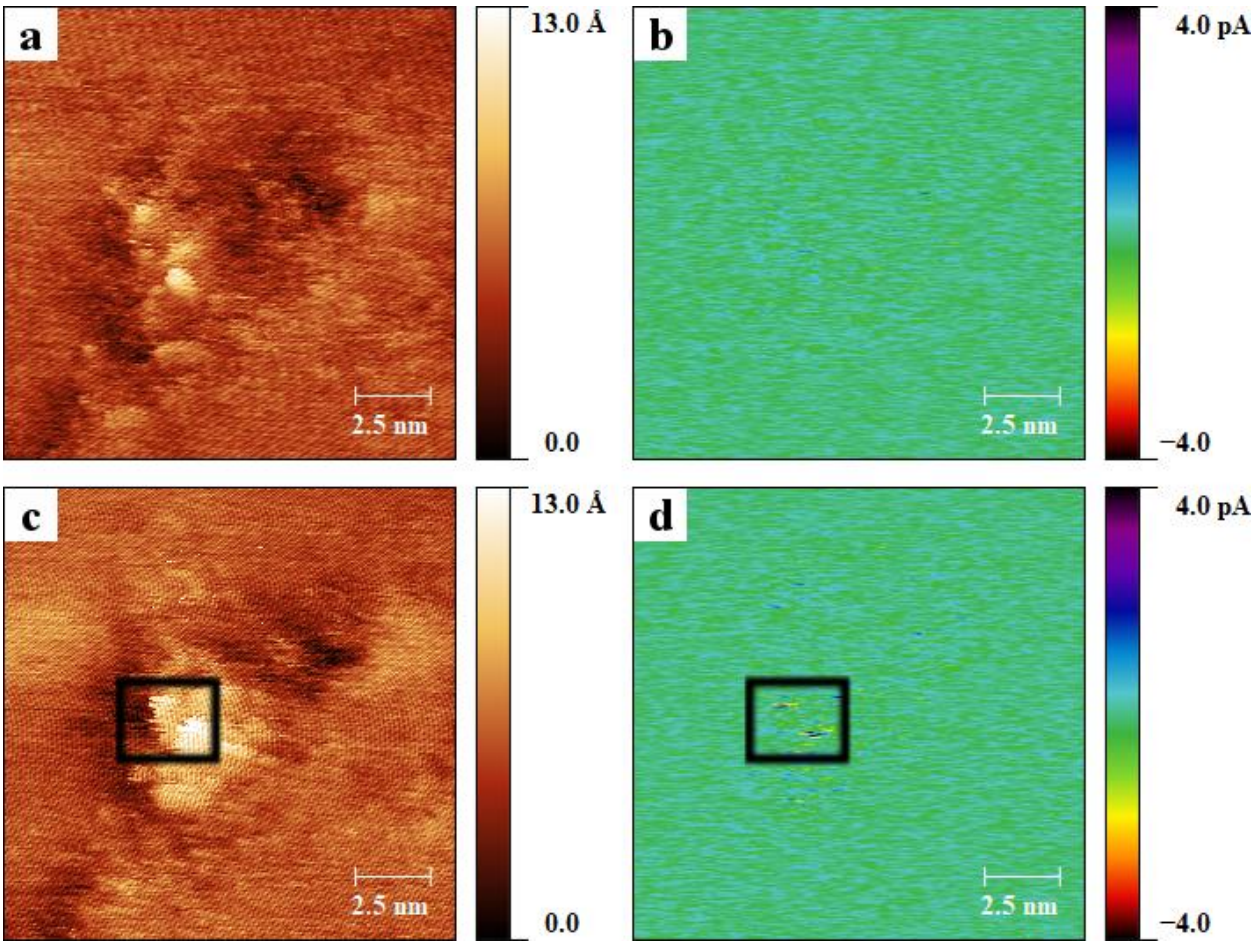

Figure 2.8. Scanning tunneling microscopy images showing C_{60} triad molecules inserted in a dodecanethiolate monolayer matrix on Au{111}. (a) Topographic and (b) spectroscopic images were simultaneously obtained when the laser was not illuminating the sample. (c) Topographic and (d) spectroscopic images were simultaneously obtained when the laser (405 nm) illuminated the sample evanescently. All images were collected at a sample bias of +1.00 V and a tunneling current of 12.0 pA. All spectroscopic images were collected phase-sensitively with a reference frequency of 4.8 kHz created by a chopper wheel that was used to modulate the evanescent sample illumination.

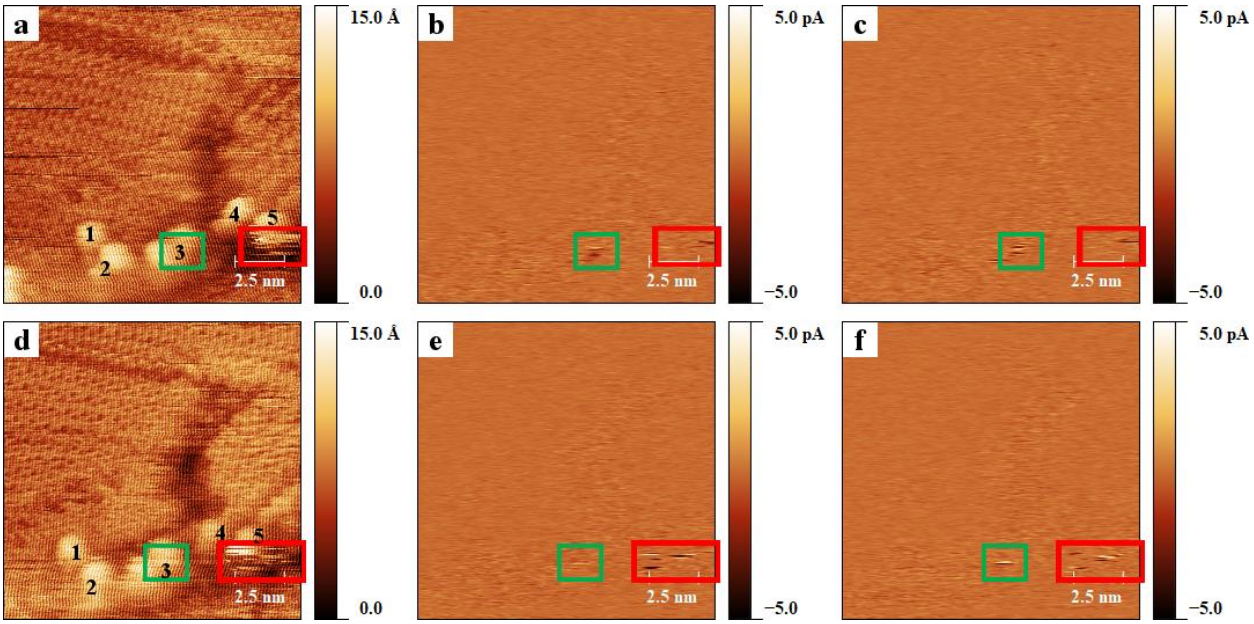

Figure 2.9. Consecutively collected scanning tunneling microscopy images under evanescent laser illumination, showing C_{60} triad molecules inserted in a dodecanethiolate monolayer matrix on Au{111}. (a) Topographic image reproduced from Figure 2.2c. (b) Spectroscopic image reproduced from Figure 2.2d. (c) 90° phase offset image collected simultaneously with (a) and (b). (d) Topographic image reproduced from Figure 2.2e. (e) Spectroscopic image reproduced from Figure 2.2f. (f) 90° phase offset image collected simultaneously with (d) and (e). All images were collected at a sample bias of -1.00 V and a tunneling current of 12.0 pA. All spectroscopic images were collected phase-sensitively with a reference frequency of 4.8 kHz created by a chopper wheel that was used to modulate the sample illumination.

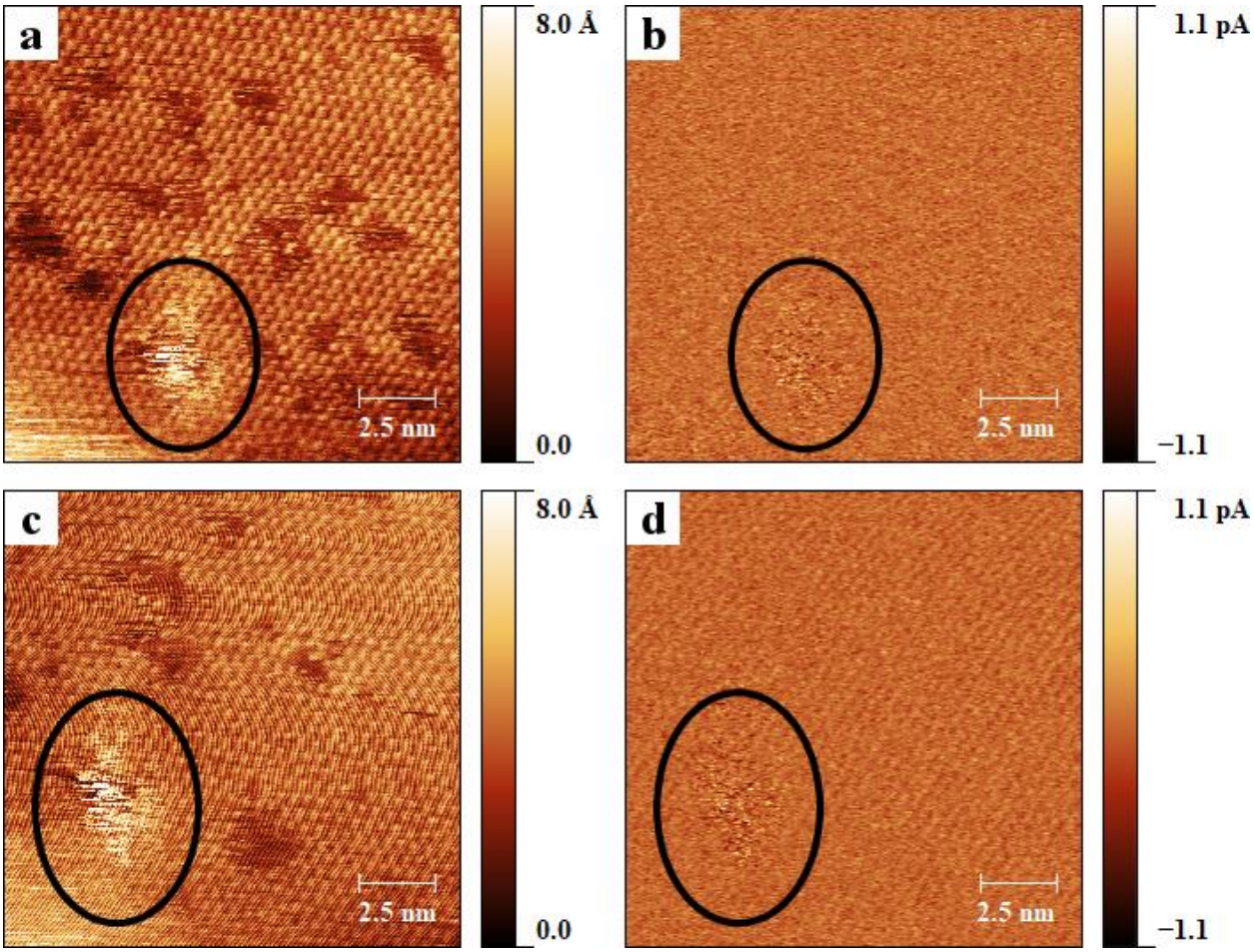

Figure 2.10. Scanning tunneling microscopy images showing 2,5-dithienylpyrrole control molecules inserted in a dodecanethiolate self-assembled monolayer matrix on Au{111}. (a,b) Simultaneously obtained topographic and spectroscopic images without illumination. (c,d) Simultaneously obtained topographic and spectroscopic images with evanescent illumination. All images were collected at a sample bias of -1.00 V and a tunneling current of 12.0 pA. All spectroscopic images were collected phase-sensitively with a reference frequency of 4.8 kHz created by a chopper wheel that was used to modulate the evanescent sample illumination.

REFERENCES

(1) Guldi, D. M. Fullerenes: Three Dimensional Electron Acceptor Materials. *Chem. Commun.* **2000**, 321–327.

(2) D'Souza, F.; Ito, O. Supramolecular Donor-Acceptor Hybrids of Porphyrins/Phthalocyanines with Fullerenes/Carbon Nanotubes: Electron Transfer, Sensing, Switching, and Catalytic Applications. *Chem. Commun.* **2009**, 4913–4928.

(3) Gayathri, S. S.; Wielopolski, M.; Perez, E. M.; Fernandez, G.; Sanchez, L.; Viruela, R.; Orti, E.; Guldi, D. M.; Martin, N. Discrete Supramolecular Donor-Acceptor Complexes. *Angew. Chem. Int. Ed.* **2009,** *48*, 815–819.

(4) Hirayama, D.; Yamashiro, T.; Takimiya, K.; Aso, Y.; Otsubo, T.; Norieda, H.; Imahori, H.; Sakata, Y. Preparation and Photoelectrochemical Properties of Gold Electrodes Modified with [60]Fullerene-Linked Oligothiophenes. *Chem. Lett.* **2000,** *29*, 570–571.

(5) Imahori, H.; Tamaki, K.; Guldi, D. M.; Luo, C. P.; Fujitsuka, M.; Ito, O.; Sakata, Y.; Fukuzumi, S. Modulating Charge Separation and Charge Recombination Dynamics in Porphyrin Fullerene Linked Dyads and Triads: Marcus-Normal versus Inverted Region. *J. Am. Chem. Soc.* **2001,** *123*, 2607–2617.

(6) Tsuboya, N.; Hamasaki, R.; Ito, M.; Mitsuishi, M.; Miyashita, T.; Yamamoto, Y. Nonlinear Optical Properties of Novel Fullerene-Ferrocene Hybrid Molecules. *J. Mater. Chem.* **2003,** *13*, 511–513.

(7) Xenogiannopoulou, E.; Medved, M.; Iliopoulos, K.; Couris, S.; Papadopoulos, M. G.; Bonifazi, D.; Sooambar, C.; Mateo-Alonso, A.; Prato, M. Nonlinear Optical Properties of Ferrocene- and Porphyrin-[60]Fullerene Dyads. *ChemPhysChem* **2007,** *8*, 1056–1064.

(8) Yamada, H.; Imahori, H.; Nishimura, Y.; Yamazaki, I.; Ahn, T. K.; Kim, S. K.; Kim, D.; Fukuzumi, S. Photovoltaic Properties of Self-Assembled Monolayers of Porphyrins and Porphyrin-Fullerene Dyads on ITO and Gold Surfaces. *J. Am. Chem. Soc.* **2003,** *125*, 9129–9139.

(9) Kim, K.-S.; Kang, M.-S.; Ma, H.; Jen, A. K. Y. Highly Efficient Photocurrent Generation from a Self-Assembled Monolayer Film of a Novel C_{60}-Tethered 2,5-Dithienylpyrrole Triad. *Chem. Mater.* **2004,** *16*, 5058–5062.

(10) Roncali, J. Linear π-Conjugated Systems Derivatized with C_{60}-Fullerene as Molecular Heterojunctions for Organic Photovoltaics. *Chem. Soc. Rev.* **2005,** *34*, 483–495.

(11) Kim, M.; Hohman, J. N.; Cao, Y.; Houk, K. N.; Ma, H.; Jen, A. K. Y.; Weiss, P. S. Creating Favorable Geometries for Directing Organic Photoreactions in Alkanethiolate Monolayers. *Science* **2011,** *331*, 1312–1315.

(12) Bumm, L. A.; Arnold, J. J.; Charles, L. F.; Dunbar, T. D.; Allara, D. L.; Weiss, P. S. Directed Self-Assembly to Create Molecular Terraces with Molecularly Sharp Boundaries in Organic Monolayers. *J. Am. Chem. Soc.* **1999,** *121*, 8017–8021.

(13) Donhauser, Z. J.; Price, D. W.; Tour, J. M.; Weiss, P. S. Control of Alkanethiolate Monolayer Structure Using Vapor-Phase Annealing. *J. Am. Chem. Soc.* **2003,** *125*, 11462–11463.

(14) Cygan, M. T.; Dunbar, T. D.; Arnold, J. J.; Bumm, L. A.; Shedlock, N. F.; Burgin, T. P.; Jones, L.; Allara, D. L.; Tour, J. M.; Weiss, P. S. Insertion, Conductivity, and Structures of Conjugated Organic Oligomers in Self-Assembled Alkanethiol Monolayers on Au{111}. *J. Am. Chem. Soc.* **1998,** *120*, 2721–2732.

(15) Claridge, S. A.; Liao, W.-S.; Thomas, J. C.; Zhao, Y.; Cao, H. H.; Cheunkar, S.; Serino, A. C.; Andrews, A. M.; Weiss, P. S. From the Bottom Up: Dimensional Control and Characterization in Molecular Monolayers. *Chem. Soc. Rev.* **2013,** *42*, 2725–2745.

(16) Feenstra, R. M.; Stroscio, J. A.; Tersoff, J.; Fein, A. P. Atom-Selective Imaging of The GaAs(110) Surface. *Phys. Rev. Lett.* **1987,** *58*, 1192–1195.

(17) Eigler, D. M.; Weiss, P. S.; Schweizer, E. K.; Lang, N. D. Imaging Xe with a Low-Temperature Scanning Tunneling Microscope. *Phys. Rev. Lett.* **1991,** *66*, 1189–1192.

(18) Pascual, J. I.; Jackiw, J. J.; Song, Z.; Weiss, P. S.; Conrad, H.; Rust, H. P. Adsorbate-Substrate Vibrational Modes of Benzene on Ag(110) Resolved with Scanning Tunneling Spectroscopy. *Phys. Rev. Lett.* **2001,** *86*, 1050–1053.

(19) Bonnell, D. A.; Basov, D. N.; Bode, M.; Diebold, U.; Kalinin, S. V.; Madhavan, V.; Novotny, L.; Salmeron, M.; Schwarz, U. D.; Weiss, P. S. Imaging Physical Phenomena with Local Probes: From Electrons to Photons. *Rev. Mod. Phys.* **2012,** *84*, 1343–1381.

(20) Ballard, J. B.; Carmichael, E. S.; Shi, D.; Lyding, J. W.; Gruebele, M. Laser Absorption Scanning Tunneling Microscopy of Carbon Nanotubes. *Nano Lett.* **2006,** *6*, 45–49.

(21) Nienhaus, L.; Wieghold, S.; Nguyen, D.; Lyding, J. W.; Scott, G. E.; Gruebele, M. Optoelectronic Switching of a Carbon Nanotube Chiral Junction Imaged with Nanometer Spatial Resolution. *ACS Nano* **2015,** *9*, 10563–10570.

(22) Cocker, T. L.; Peller, D.; Yu, P.; Repp, J.; Huber, R. Tracking the Ultrafast Motion of a Single Molecule by Femtosecond Orbital Imaging. *Nature* **2016,** *539*, 263–267.

(23) Nguyen, D.; Nguyen, H. A.; Lyding, J. W.; Gruebele, M. Imaging and Manipulating Energy Transfer Among Quantum Dots at Individual Dot Resolution. *ACS Nano* **2017,** *11*, 6328–6335.

(24) Moore, A. M.; Mantooth, B. A.; Donhauser, Z. J.; Maya, F.; Price, D. W.; Yao, Y. X.; Tour, J. M.; Weiss, P. S. Cross-Step Place-Exchange of Oligo(phenylene-ethynylene) Molecules. *Nano Lett.* **2005,** *5*, 2292–2297.

CHAPTER 3

Photoinduced Carrier Distribution in Titanyl Phthalocyanine Monolayers

(**Adapted from: Wang, S.**; Chiang, N.; Guo, H.; Wattanatorn, N.; Barr, K.; Alexandrova, A.; Weiss, P. S., Photoinduced Carrier Distribution in Titanyl Phthalocyanine Monolayers. *Submitted*.)

3.1 Introduction

Titanyl phthalocyanine (TiOPc, Figure 3.1a) has been widely studied as a potential candidate for organic photovoltaic solar cells,[1-6] organic light emitting diodes,[7] and field effect transistors[8-10] due to its efficient photoelectric activities in the visible and near-IR regions.[11] Titanyl phthalocyanine is a nonplanar molecule with the titanyl group located perpendicular to the phthalocyanine plane (Figure 3.1a), resulting in various crystal structures. Three major polymorphs have been reported for TiOPc, including monoclinic phases I (β-TiOPc) and Y, and a triclinic phase II (α-TiOPc).[12] The optical responses of different TiOPc polymorphs are significantly different from each other since their carrier generation efficiencies greatly depend on intermolecular interactions.[3,4,12] Understanding the relationships between the arrangements of the TiOPc molecules and their photoelectric properties is critical for optimizing the performance of TiOPc based optoelectronic devices. More generally, optimizing the structures and relative orientations of components of solar cells and other energy harvesting devices has the potential to increase the efficiencies of photoexcitation, charge separation, and the overall devices. Thus, as a community, we have developed new multimodal nanoscale analysis tools that enable us to elucidate structures while simultaneously measuring local spectra and function.[13-25]

Scanning tunneling microscopy (STM) has been used to study the adsorption of TiOPc molecules on various surfaces.[10,26-32] In most of these studies, the deposition of TiOPc molecules was conducted in ultra-high vacuum (UHV) and therefore the arrangements of the molecules are significantly different from TiOPc crystals. When approaching low surface coverages (*i.e.*, < 1 monolayer), TiOPc molecules adsorb on metal surfaces with their phthalocyanine plane

parallel to the substrates.[32] In monolayers prepared *in vacuo*, TiOPc molecules are distorted and their arrangements depends strongly on the structure of the substrates.[10,27-31]

Incorporating laser irradiation into the tunneling junction extends the capabilities of STM and enables us to probe photoinduced carrier dynamics at the nanoscale.[14,16,18,33-37] The photo excited orbitals of a variety of photoactive nanostructures and molecules have been visualized with submolecular resolution and studied by local spectroscopic methods.[38-45] Here, we used a custom-built laser-assisted STM[23,25] to measure the photo-responses of TiOPc monolayers that were prepared through solution deposition,[26,46] to reproduce real-life applications more realistically. We observed two types of lattice structures, which are different from those reported for UHV deposition or at liquid/solid interfaces. The lattice parameters we observed are different from bulk TiOPc crystals but the molecules are densely packed in both lattices. Three lasers with wavelengths of 405 nm, 633nm, and 780 nm were used for interrogating the optical responses of TiOPc monolayers. Both 633 nm and 780 nm falls in the Q band of TiOPc, and 405 nm laser was used in a control experiment to test the thermal expansion effect of the STM tip-sample junction since TiOPc does not absorb 405 nm light efficiently.[12] The laser beams were modulated by a chopper wheel at 4.8 kHz and were introduced into the tunneling junction through total internal reflection, as illustrated in Figure 3.1b. Different photo-responses were observed for the two lattice structures. Density functional theory (DFT) calculations of the ground state and excited state molecular orbitals were compared to and used to interpret the data. Our results indicate that the photoinduced carrier generation within TiOPc monolayers depends on the arrangement of TiOPc molecules and local environment.

3.2 Experimental Methods

3.2.1 Preparation of titanyl phthalocyanine (TiOPc) monolayers.

Freshly flame-annealed Au{111}/Al_2O_3(0001) substrates were immersed in a saturated ethanolic solution of TiOPc (Sigma Aldrich, St. Louis, MO) for 10 min. We note that TiOPc does not completely dissolve in ethanol. Substrates were then rinsed thoroughly with ethanol and blown dry using nitrogen.

3.2.2 Theoretical Analyses.

Density functional theory (DFT) calculations with periodic boundary conditions were performed to obtain the geometries for the TiOPc monolayers and compute the band-decomposed charge densities. All calculations were performed for gas-phase structures.

All the electronic structure calculations were performed using the plane-wave DFT-based Vienna *ab initio* simulation package (VASP).[47-50] The interactions between the ionic cores and the electrons were described by fully nonlocal optimized projector augmented-wave (PAW) potentials[51,52], and exchange and correlation effects were treated within the generalized gradient approximation (GGA) using the Perdew-Burke-Ernzerhof (PBE) functional[53,54]. We used a vacuum space of 6.2 Å between the monolayers to avoid spurious interactions between repeated images in the z direction. A $2 \times 4 \times 1$ Monkhorst-Pack *k*-point grid and a cutoff energy of 400 eV for the plane-wave basis set were chosen for all calculations.

To consider different orientations of the molecules in the monolayers, the monomer was first packed and optimized in one dimension with different initial orientations about the Ti-O bond. The optimized one-dimensional structures were then packed in the other dimension and relaxed to give the optimized structures for the monolayers. We also compute the band-decomposed charge

density for HOMO and excited bands, as well as their differences, using VASP. The charge density differences between HOMO and excited bands were computed by subtracting the band-decomposed charge density of HOMO from the charge density of the excited band, and plotted by VESTA[55]. All charge density images are plotted with an isodensity value of 0.001. The constant-current STM images were simulated using the Tersoff-Hamann method.[56]

3.3 Results and Discussions

3.3.1 Titanyl phthalocyanine monolayers

We observed two types of lattice structures in TiOPc monolayers. The first lattice has unit cell parameters a = 1.21 ± 0.02 nm, b = 0.64 ± 0.01 nm, and α = 123 ± 1° (Figure 3.2a). The unit cell parameters for the second structure are c = 1.18 ± 0.02 nm, d = 0.40 ± 0.01 nm, and β = 89 ± 3° (Figure 3.2b). We tentatively name these structures hexagonal and rectangular lattices, respectively. The unit cell parameters reported here suggest that in the observed monolayers, TiOPc molecules are densely packed and stand nearly normal to the Au{111} surface, so the interactions between the molecules and the substrates should be weak. Therefore, in DFT calculations, we neglected the effects of the surface-molecule interactions and all calculations on the geometry optimization for TiOPc molecules and the band-decomposed charge density were performed for gas-phase molecules.

To optimize the structures of the molecules in two types of lattice structures in the TiOPc monolayers, we first packed and optimized the molecules in one dimension. For hexagonal lattice structure, the molecules were first packed along the lattice vector b, and b = 0.64 nm, α = 123° from experimental measurement. For rectangular lattice structure, experimental values b = 0.40 nm and α = 90 ° were used. Since the molecules are densely packed, we set lattice vector a to

be 1.50 nm for both lattice structures to allow full relaxation of the molecular orientation. To consider different orientations of the molecules, we rotated the gas-phase structure about the Ti-O bond by an angle θ (Figure 3.3), and chose $\theta = 10, 20, \ldots, 80°$ as the initial orientations for both lattice structures.

The optimized one-dimensional structures were used as the initial configurations for two-dimensional optimization. We gradually decreased the length of the lattice vector a to match the experimental value a = 1.21 nm for hexagonal lattice and a = 1.18 nm for rectangular lattice. The optimized structure in one unit cell for the hexagonal lattice is shown in Figure 3.4.

The electron density of the highest occupied molecular orbital (HOMO) of TiOPc is shown in Figure 3.5a, and the proposed packing arrangements for hexagonal and rectangular lattices are shown in Figure 3.5b,c, respectively. We simulated STM images for TiOPc hexagonal and rectangular lattices from E_F (Fermi energy) – 1.0 eV to E_F based on the band decomposed charge density we calculated using DFT calculations, as shown in Figure 3.6. Figure 3.6 is similar to the STM images we obtained using our laser-assisted STM (Figure 3.2), which suggests that the optimized geometry we used for our calculation matches the real geometry of TiOPc in monolayers. The intermolecular distances in the hexagonal and rectangular lattices are close to those reported in TiOPc crystals and liquid/solid interface[11,12,26] and are significantly smaller than those previously reported for STM data in UHV.[27-29,32]

3.3.2 Photo-responses of titanyl phthalocyanine in monolayers

We investigated the photo-responses of molecules in the TiOPc hexagonal lattice using laser-assisted STM with 633 nm (3.5 mW) laser illumination. Consecutively obtained STM topographic images of the same region and simultaneously acquired spectroscopic images are

shown in Figure 3.7. Figure 3.7b,d are spectroscopic images of in-phase lock-in signals with a reference frequency of 4.8 kHz created by a chopper wheel that was used to modulate the evanescent sample illumination. The blue and green boxes, which highlight the same area in Figure 3.7a,b and Figure 3.7c,d, respectively, represent the unit cell of the hexagonal lattice; they contain a single TiOPc molecule. In Figure 3.7b,d, there are protrusions directly corresponding to the positions of TiOPc molecules in Figure 3.7a,c. In our experimental setup, the increase of tunneling current caused by laser-induced thermal expansion of the tunneling junction results in negative in-phase lock-in signals, as indicated by the color bar in Figure 3.7b,d. On the other hand, the protrusions in Figure 3.7b,d suggest that the corresponding positions have lower electron density during the illumination interval compared to the surrounding area.[25] Such distributions of lower photoelectron densities are attributed to the excitation of TiOPc molecules at 633 nm and relate to the differences in electron density between the exited state and ground state molecular orbitals.[42,45,57] Furthermore, as shown in Figure 3.7b,d, the probability for TiOPc molecules to be excited at 633 nm is different between molecules. For some TiOPc molecules, there are no corresponding protrusions in the spectroscopic images, indicating that those molecules have lower excitation probabilities. The local environment in this area can affect the distribution of the evanescent field and results in differences in excitation probabilities.

We also excited the TiOPc molecules in the hexagonal lattice with 780 nm (7.7 mW) laser illumination. Figure 3.8a,b are topographic and simultaneously collected spectroscopic images obtained under evanescent 780 nm laser illumination at the same area as Figure 3.7. The yellow boxes in Figure 3.8 represent the shape of a unit cell of the hexagonal lattice and highlight the same area in corresponding images. From Figure 3.8b, we can see that under 780 nm illumination,

the excitation of TiOPc molecules results in low photoelectron density in the local area, similar to 633 nm illumination. The distribution of photoelectrons in Figure 3.8b is not homogeneous across this area, indicating that this area may not be perfectly perpendicular to the polarization direction of the laser.

In order to interpret the photoelectron distributions that we observed in Figures 3.7 and 3.8, we calculated the charge density differences between excited states and ground state molecular orbitals of TiOPc in hexagonal lattice. Charge density differences between the lowest unoccupied molecular orbital (LUMO) and HOMO of TiOPc are shown in Figure 3.9a,b. Charge density differences between LUMO+1 and HOMO of TiOPc are shown in Figure 3.9c,d. According to our calculations, the LUMO is doubly degenerate in the gas phase, but the energy band splits into two sub-bands in the hexagonal lattice, due to interactions between adjacent molecules. The excitation of TiOPc from HOMO to LUMO and LUMO+1 correspond to the Q band of TiOPc. In Figure 3.9, the yellow color represents increases in charge density when molecules are excited from the ground state to excited states, while the blue color represents decreases in charge density. We can see that there are decreases in charge density on the phenyl rings when TiOPc is excited from HOMO to LUMO or LUMO+1. This result is consistent with the spectroscopic images in Figure 3.7 and 3.8, and that the laser-assisted STM characterizes the distribution of photoelectrons in TiOPc hexagonal lattice. The slight differences between Figure 3.7b,d and Figure 3.8b may be due to the fact that TiOPc molecules are excited predominantly to the LUMO by 780 nm light and to the LUMO+1 by 633 nm light. However, since our experiments were carried out at room temperature under ambient conditions, the topographic and spectroscopic images are likely to be

convoluted results of different energy levels of the entire system,[58-67] and the calculated results are not expected to match the experimental data precisely.

In order to test whether moving the STM tip can introduce mechanical noise to the in-phase signals we collect, we simultaneously obtained topographic and spectroscopic images on TiOPc rectangular lattice when there was no illumination of the surface but the chopper wheel and the rest of the electronics were working under otherwise identical conditions. From the images we obtained in dark in Figure 3.10, we can see that there is no such mechanical noise in Figure 3.10b. Such results indicate that the patterns we see in spectroscopic images collected under laser illuminations in this chapter are due to the excitation of TiOPc molecules or thermal expansion of the tunneling junction.

In order to test the effects of thermal expansion and hot electron tunneling in the STM junction on the in-phase lock-in signal, we performed a control experiment by characterizing the hexagonal lattice under 405 nm laser (5 mW) illumination. Figure 3.11a,b are topographic and simultaneously collected spectroscopic images showing the hexagonal lattice obtained under 405 nm laser illumination. The pink boxes represent the shape of a unit cell for hexagonal lattice and highlight the same area in corresponding images. From Figure 3.11b we can see that TiOPc molecules correspond to more negative in-phase signals, which means that the corresponding positions have higher photoelectron densities than the surrounding area. Figure 3.11b is significantly different from the spectroscopic images collected under 633 or 780 nm laser illumination, and the increase of photoelectron density on top of the molecules does not match our DFT calculation results. Since TiOPc should not absorb 405 nm light as efficiently as 633 nm and 780 nm light,[12] we tentatively attribute such negative in-phase signals to the thermal expansion of the tunneling junction.

We also studied the photo-responses of molecules assembled into rectangular lattices using our laser-assisted STM with 633 nm and 780 nm laser illumination. Figure 3.12a,b shows simultaneously obtained topographic and spectroscopic images with 633 nm excitation. The white boxes represent the shape of a unit cell for rectangular lattice and highlight the same area in corresponding images. Figure 3.12c,d are simultaneously obtained topographic and spectroscopic images with 780 nm excitation. The black boxes represent the shape of a unit cell for the rectangular lattice and highlight the same area in corresponding images. From Figure 3.12, we see that under both 633 nm and 780 nm excitation, TiOPc molecules correspond to higher photoelectron densities than the surrounding areas. This result indicates that the photo-responses of molecules in the rectangular lattices are different than those in the hexagonal lattices. We calculated the charge density differences between excited states and ground state molecular orbitals of TiOPc and the results are shown in Figure 3.13. By comparing Figure 3.13 with Figure 3.9, we can see that in the rectangular lattice, when TiOPc molecules are excited from HOMO to LUMO or LUMO+1, there are more charge density increases at the center of the macro ring than that for the hexagonal lattice, but the general distribution of charge density changes is similar to those for the hexagonal lattice. However, the photoelectron distribution in rectangular lattice does not match the theoretical prediction well, which indicates that TiOPc molecules may have low excitation probabilities in the rectangular lattice. The patterns we see in Figure 3.12 may have been caused by thermal expansion of the tunneling junction. Our data suggest that different packing arrangements of TiOPc in monolayers lead to different photo-responses. The density of states (DOS) and projected density of states (PDOS) of TiOPc in hexagonal and rectangular lattices are calculated and plotted in Figure 3.14. The HSE06 hybrid functional was used for DOS and PDOS

calculations.[68] From Figure 3.14 we can see that the energy gaps between HOMO and LUMO or LUMO+1 for TiOPc molecules in *hexagonal* lattices are calculated to be 1.5-2.0 eV (excluding the effects of the substrate), which matches the 633 nm and 780 nm photon energies. However, the energy gaps between HOMO and LUMO or LUMO+1 for TiOPc molecules in *rectangular* lattices are calculated to be at or below 1.5 eV (excluding the effects of the substrate), indicating that 633 nm and 780 nm photons may not be absorbed strongly by TiOPc molecules packed in rectangular lattices. We note that the conjugated backbones of TiOPc molecules are stacked more directly and densely in rectangular lattices than in hexagonal lattices. The π-π stacking between TiOPc molecules in rectangular lattices is rather large (4.0 Å) for strong coupling, but could nonetheless increase carrier mobility in the monolayers, reducing the observed local effects of the photoexcitation on single TiOPc molecules in laser-assisted STM measurements.[69-72] More detailed study is needed to correlate our results to the optoelectronic properties of TiOPc crystals and thin films.

3.4 Conclusions and Prospects

Using laser assisted STM, we have characterized the photo-responses of TiOPc molecules in two lattice structures we observed in solution deposited TiOPc monolayers on Au{111}. In hexagonal lattices, when TiOPc molecules are activated from HOMO to LUMO or LUMO+1 by 633 nm or 780 nm lasers, we observed lower photoelectron density on top of the molecules. Such results match the charge density differences between excited states and ground state molecular orbitals of TiOPc obtained by DFT calculations. The DFT predicted photo-responses of TiOPc molecules in rectangular lattices are similar to those in hexagonal lattices, but the photoelectron distributions that we observed experimentally in spectroscopic images are different from those

predictions. Our data suggest that TiOPc molecules have lower excitation probabilities at 633 nm or 780 nm when organized in rectangular lattices than when in hexagonal lattices, and that the local environments can affect the absorption. By using the laser assisted STM, we have elucidated photoelectron distributions with submolecular resolution that cannot otherwise be extracted. Our results provide insight into the importance of packing arrangements in photoexcitation and carrier generation efficiencies in bulk crystals, thin films, and smaller assemblies.

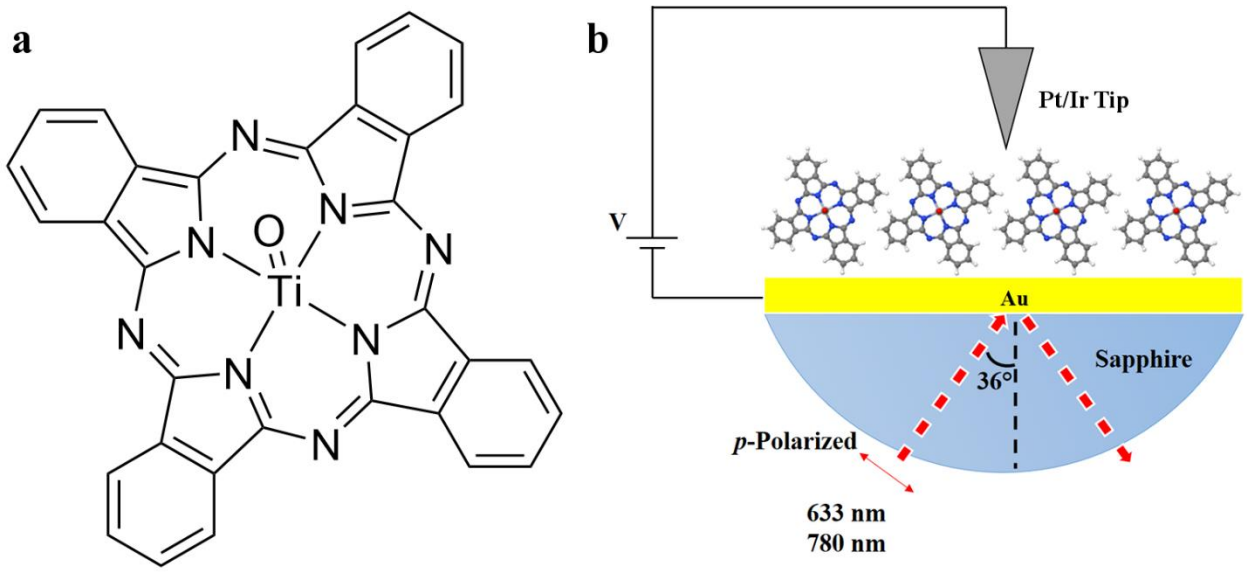

Figure 3.1. (a) Chemical structure of titanyl phthalocyanine (TiOPc). (b) Schematic illustration of TiOPc monolayers photoexcited evanescently and studied by laser-assisted scanning tunneling microscopy.

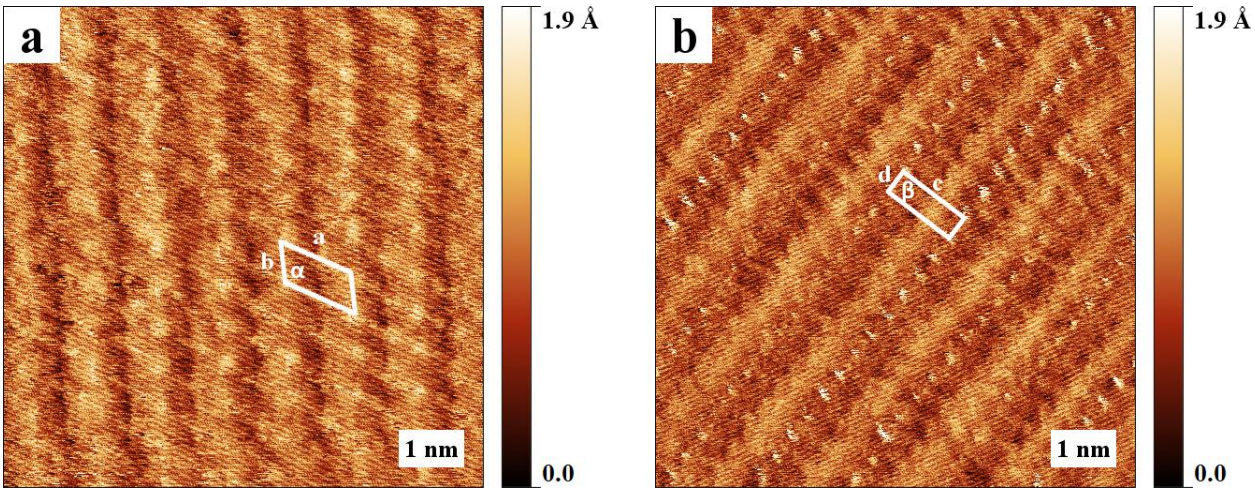

Figure 3.2. Scanning tunneling microscopy (STM) images of titanyl phthalocyanine (TiOPc) monolayers on Au{111}. (a) Hexagonal lattice. Unit cell parameters are a = 1.21 ± 0.02 nm, b = 0.64 ± 0.01 nm, α = 123 ± 1°. (b) Rectangular lattice. Unit cell parameters are c = 1.18 ± 0.02 nm, d = 0.40 ± 0.01 nm, β = 89 ± 3°. All images were collected at a sample bias of −1.00 V and a tunneling current of 70.0 pA.

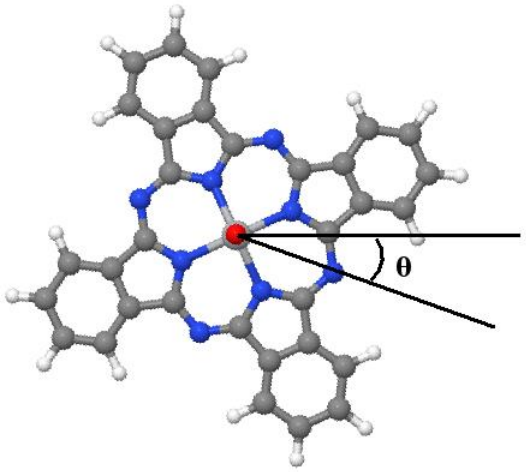

Figure 3.3. Single TiOPc molecule configuration. The molecule is rotated about the Ti-O bond by an angle of θ.

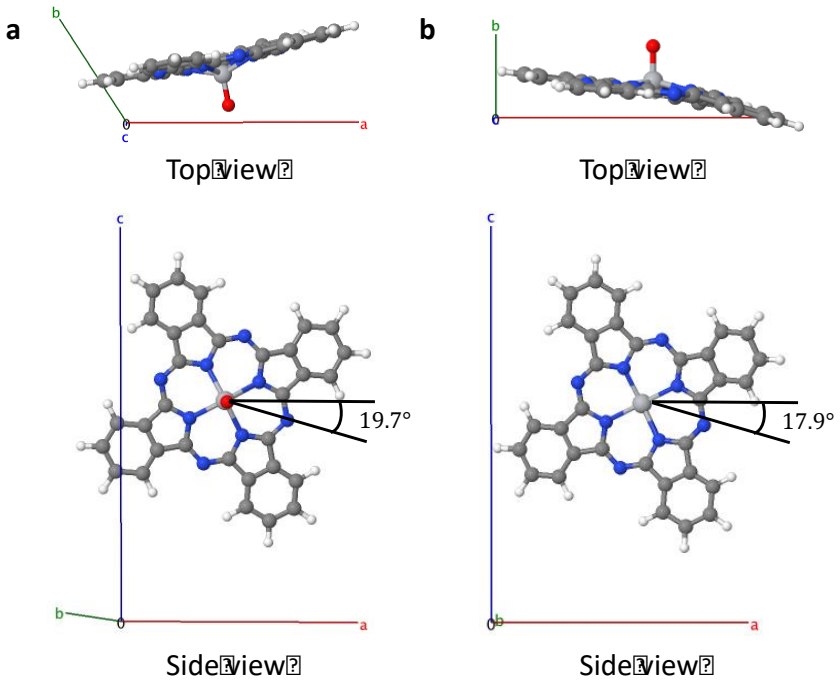

Figure 3.4. Optimized geometries for (a) hexagonal lattice structure and (b) rectangular lattice structure.

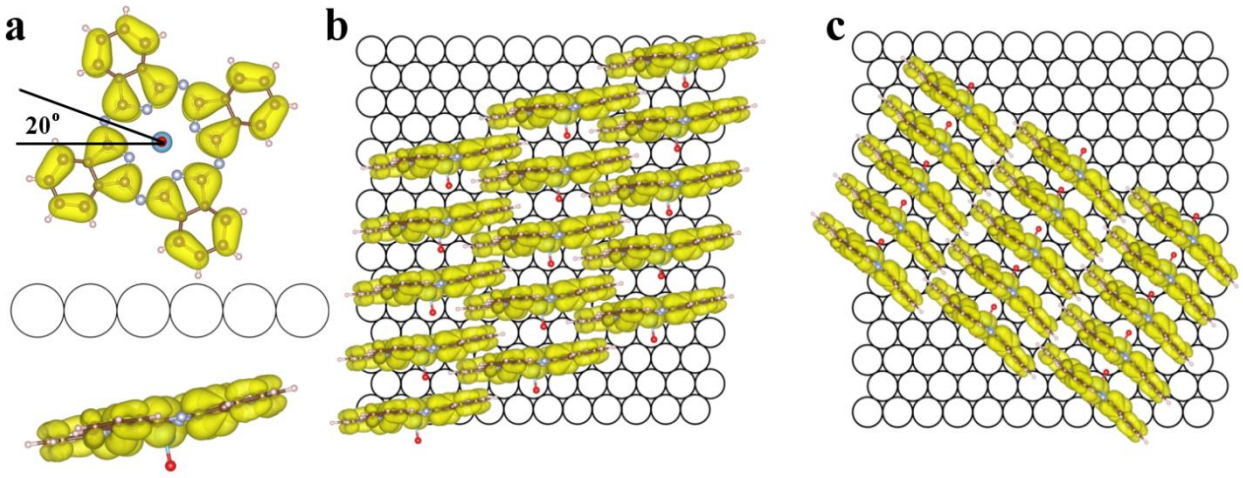

Figure 3.5. (a) Electron density of the highest occupied molecular orbital (HOMO) of titanyl phthalocyanine (TiOPc) viewed from directions perpendicular (upper image) and parallel (lower image) to the phthalocyanine ring. (b) Proposed packing arrangement of TiOPc molecules in hexagonal lattice on Au{111}. (c) Proposed packing arrangement of TiOPc molecules in rectangular lattice on Au{111}.

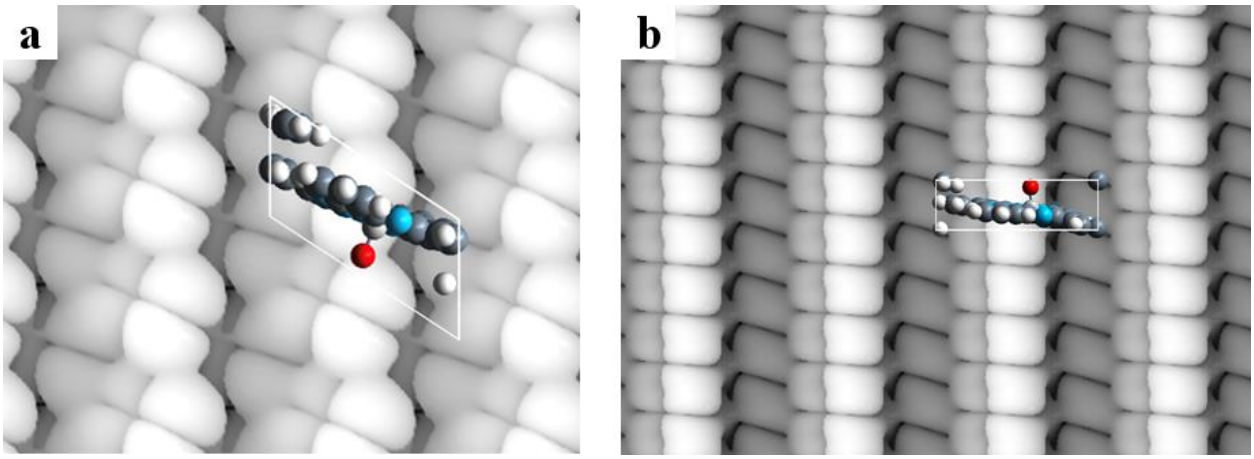

Figure 3.6. Simulated scanning tunneling microscope images for (a) hexagonal and (b) rectangular lattice structures. The images are generated for energy between E_F – 0.1 eV and E_F, with an isodensity value of 0.005.

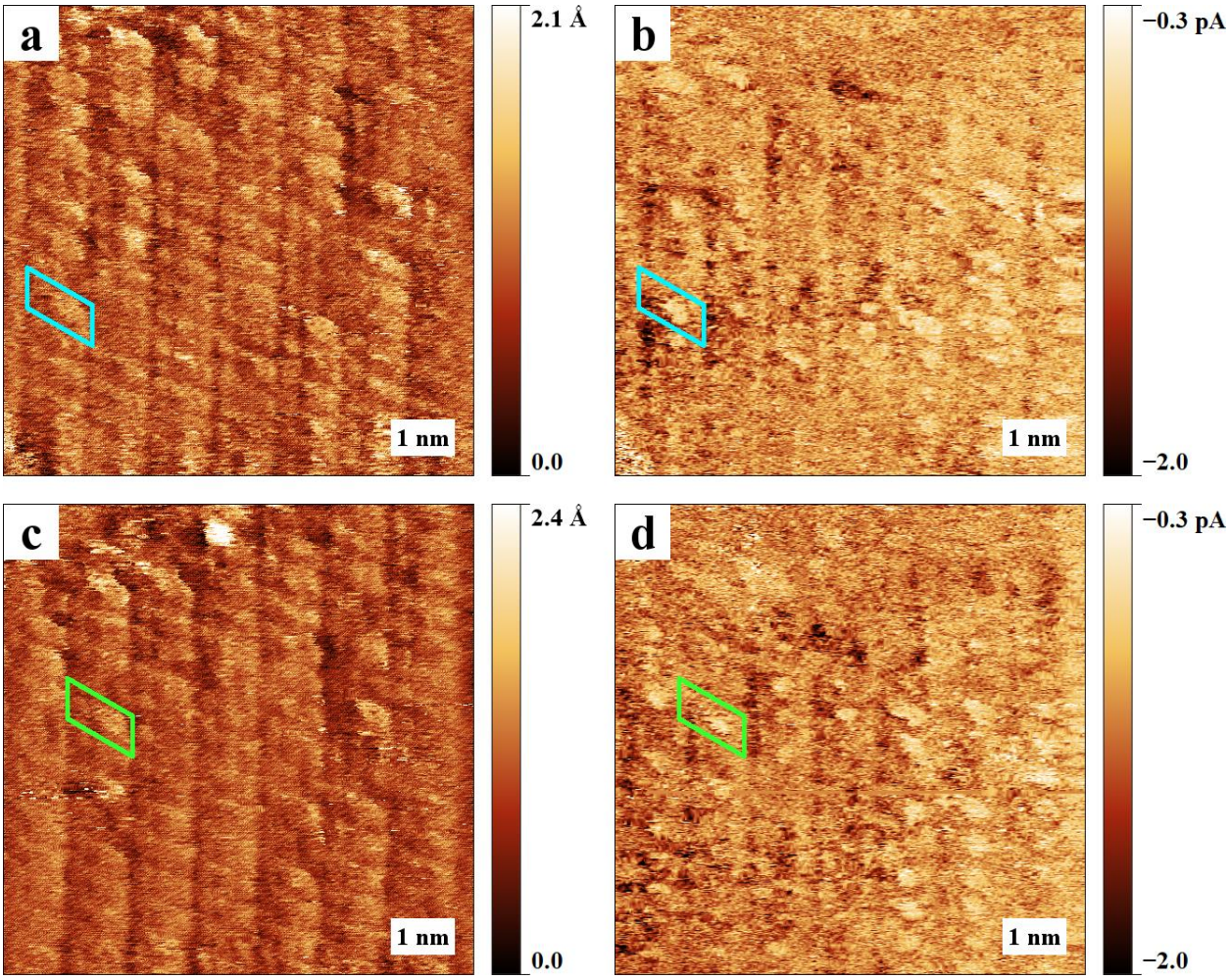

Figure 3.7. Consecutively collected scanning tunneling microscopy (STM) images under evanescent 633 nm laser (3.5 mW) illumination, showing titanyl phthalocyanine (TiOPc) monolayers (with a hexagonal lattice) on Au{111}. (a) Topographic and (b) spectroscopic images were simultaneously obtained. The blue boxes highlight the same area in corresponding images. (c) Topographic and (d) spectroscopic images were simultaneously obtained immediately after (a) and (b). The green boxes highlight the same area in corresponding images. All images were collected at a sample bias of −1.00 V and a tunneling current of 70.0 pA. All spectroscopic images were collected phase sensitively with a reference frequency of 4.8 kHz created by a chopper wheel that was used to modulate the evanescent sample illumination.

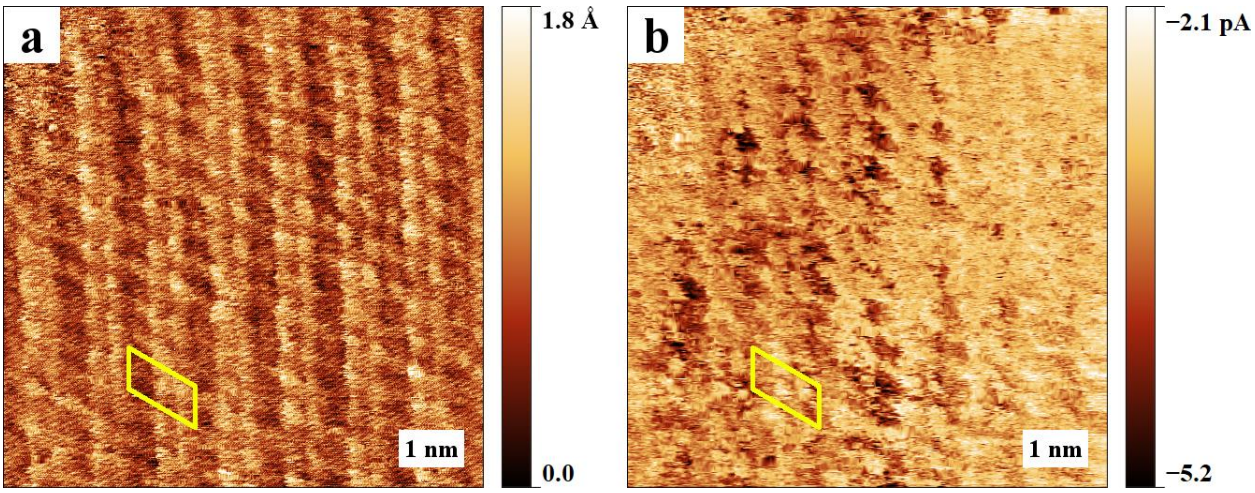

Figure 3.8. Scanning tunneling microscopy (STM) images collected under evanescent 780 nm laser (7.7 mW) illumination, showing titanyl phthalocyanine (TiOPc) monolayers (with a hexagonal lattice) on Au{111}. (a) Topographic and (b) spectroscopic images were simultaneously obtained. The yellow boxes highlight the same area in corresponding images. All images were collected at a sample bias of −1.00 V and a tunneling current of 70.0 pA. Spectroscopic images were collected phase sensitively with a reference frequency of 4.8 kHz created by a chopper wheel that was used to modulate the evanescent sample illumination.

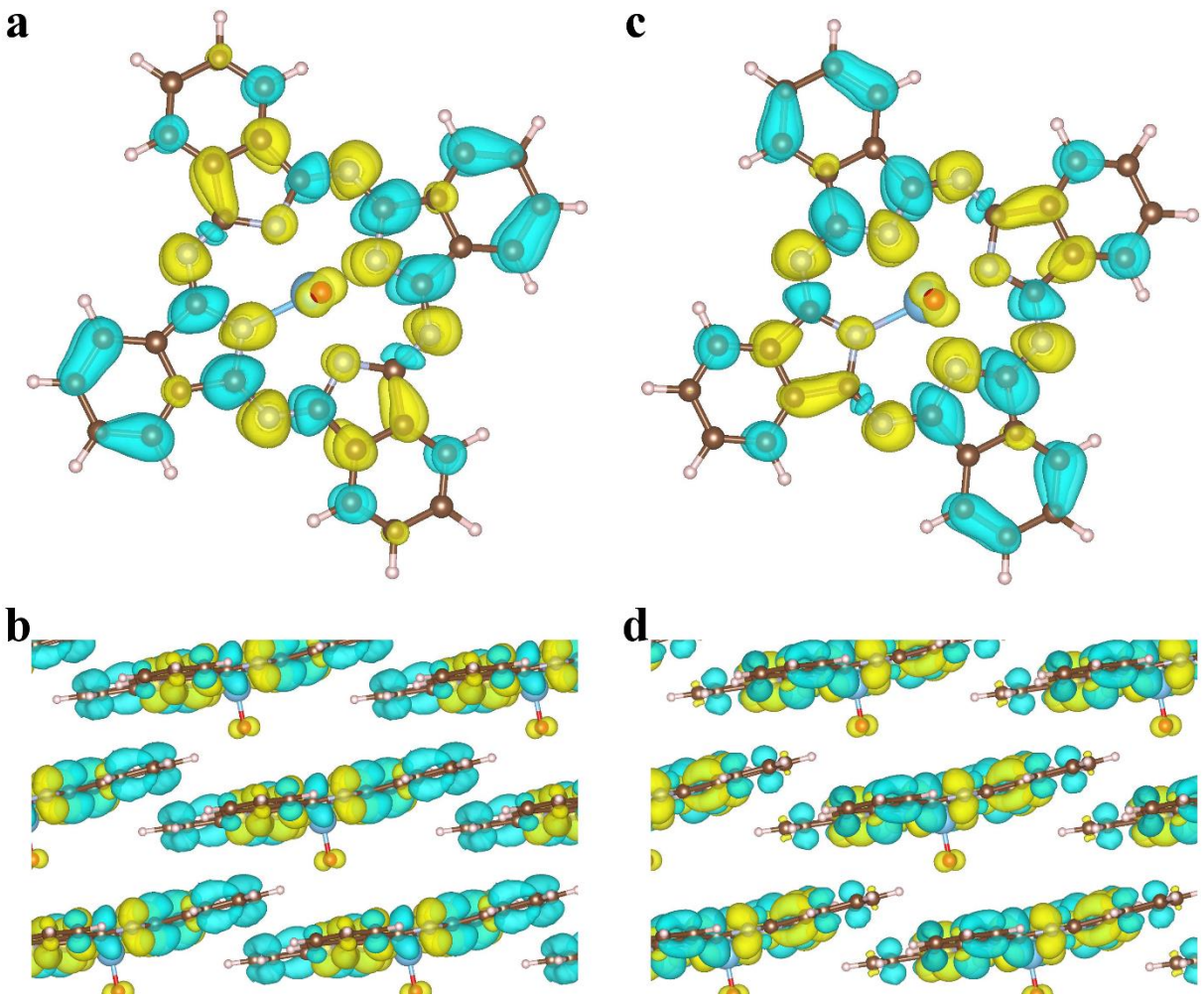

Figure 3.9. (a,b) Charge density differences between the lowest unoccupied molecular orbital (LUMO) and highest occupied molecular orbital (HOMO) of titanyl phthalocyanine (TiOPc) in hexagonal lattice. (c,d) Charge density differences between LUMO+1 and HOMO of TiOPc in the hexagonal lattice. The yellow color represents increases in charge density when molecules are excited from the ground state to excited states, while the blue color represents corresponding decreases in charge density.

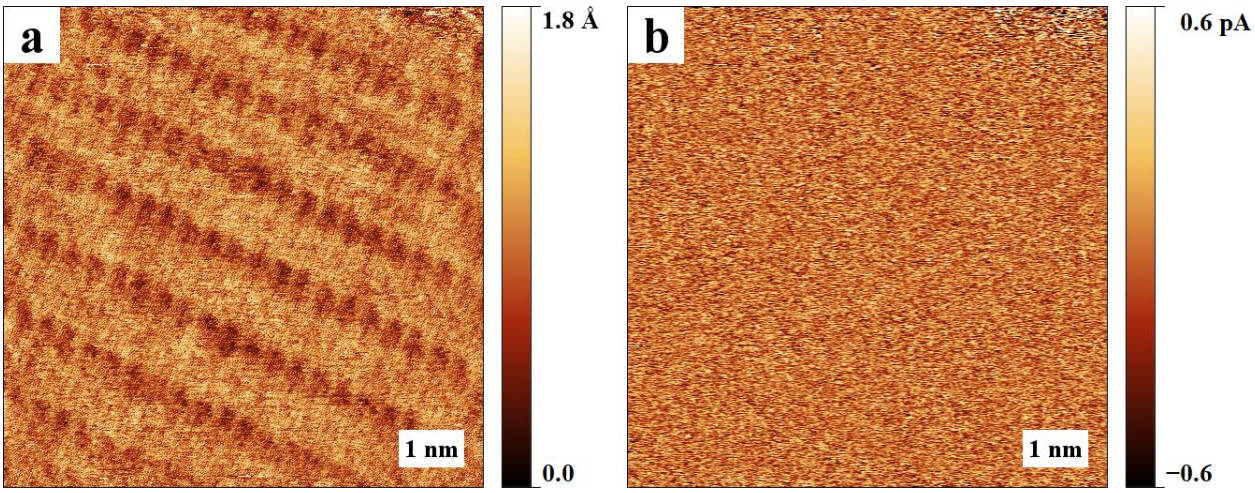

Figure 3.10. Scanning tunneling microscopy images showing titanyl phthalocyanine monolayers on Au{111}. (a) Topographic and (b) spectroscopic images were simultaneously obtained without illumination. All images were collected at a sample bias of −1.00 V and a tunneling current of 70.0 pA. The spectroscopic image was collected phase sensitively with a reference frequency of 4.8 kHz generated by a chopper wheel.

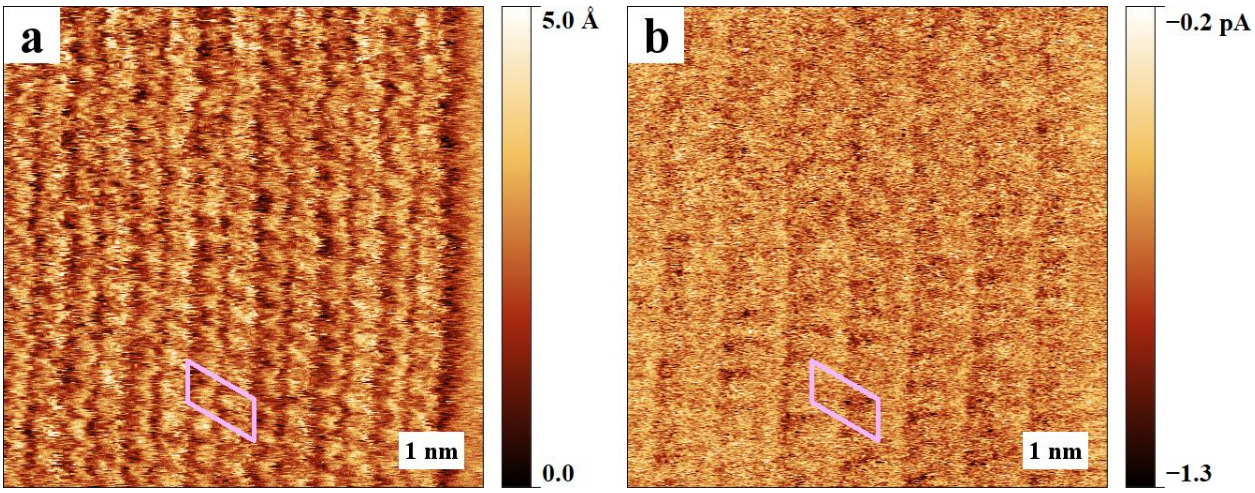

Figure 3.11. Scanning tunneling microscopy (STM) images collected under evanescent 405 nm laser (5 mW) illumination, showing titanyl phthalocyanine (TiOPc) monolayers (with a hexagonal lattice) on Au{111}. (a) Topographic and (b) spectroscopic images were simultaneously obtained. The pink boxes highlight the same area in corresponding images. All images were collected at a sample bias of −1.00 V and a tunneling current of 70.0 pA. Spectroscopic image was collected phase sensitively with a reference frequency of 4.8 kHz created by a chopper wheel that was used to modulate the evanescent sample illumination.

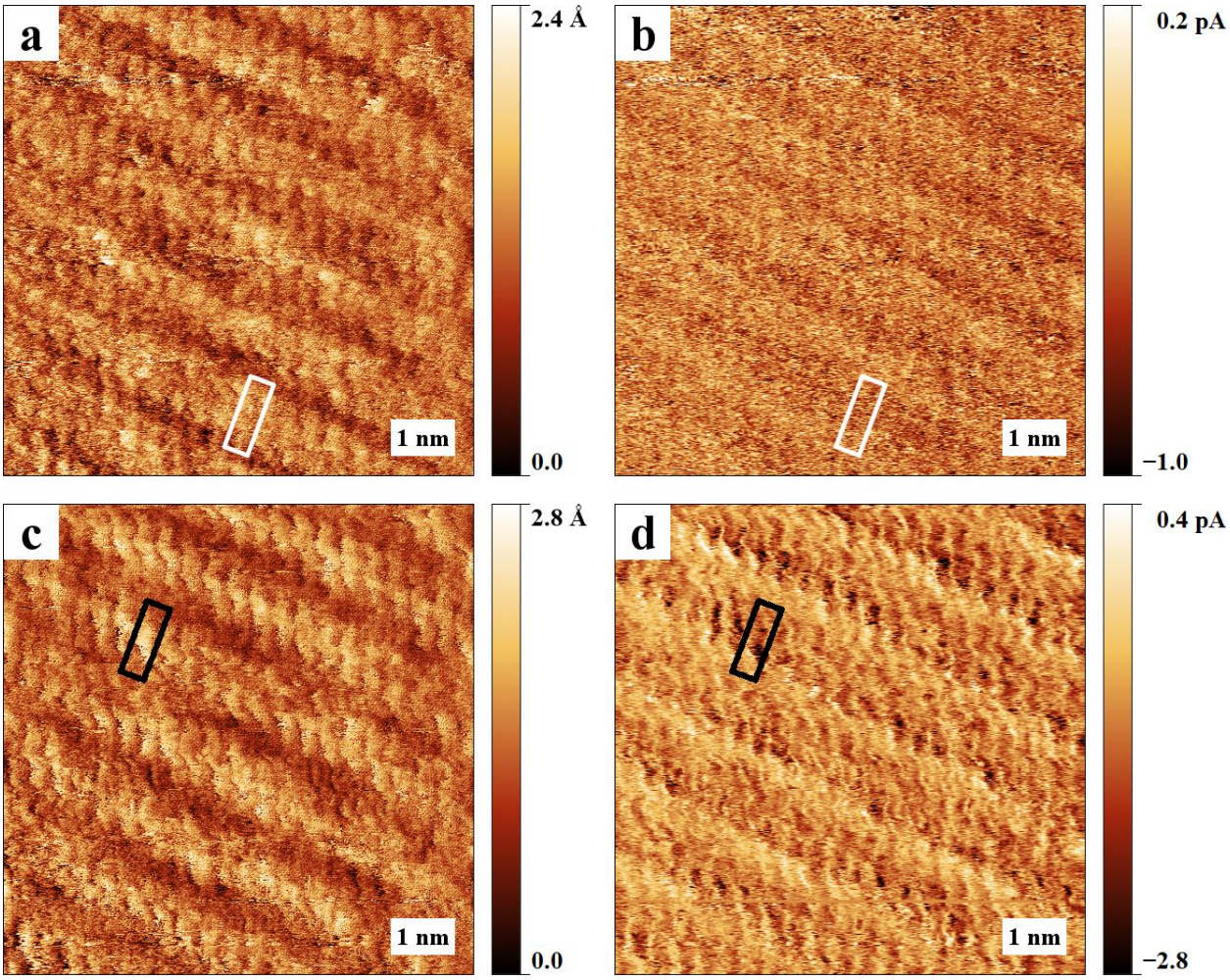

Figure 3.12. Scanning tunneling microscopy (STM) images collected under evanescent laser illumination, showing titanyl phthalocyanine (TiOPc) monolayers (with a rectangular lattice) on Au{111}. (a) Topographic and (b) spectroscopic images were simultaneously obtained when a 633 nm laser illuminated the sample evanescently. The white boxes highlight the same area in corresponding images. (c) Topographic and (d) spectroscopic images were simultaneously obtained when a 780 nm laser illuminated the sample evanescently. The black boxes highlight the same area in corresponding images. All images were collected at a sample bias of −1.00 V and a tunneling current of 70.0 pA. All spectroscopic images were collected phase sensitively with a

reference frequency of 4.8 kHz created by a chopper wheel that was used to modulate the evanescent sample illumination.

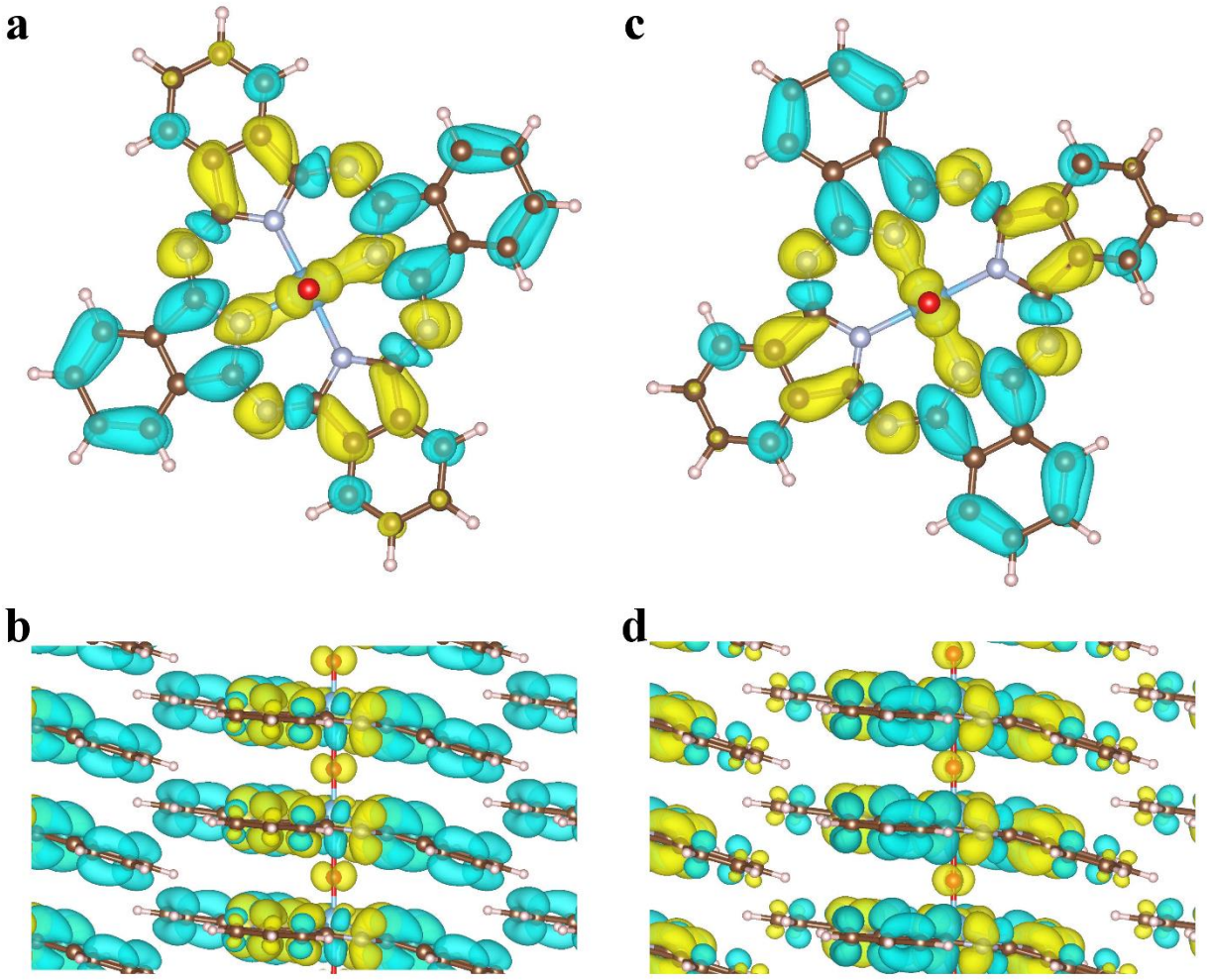

Figure 3.13. (a,b) Charge density differences between the lowest unoccupied molecular orbital (LUMO) and highest occupied molecular orbital (HOMO) of titanyl phthalocyanine (TiOPc) in a rectangular lattice. (c,d) Charge density differences between LUMO+1 and HOMO of TiOPc in a rectangular lattice. The yellow color represents increases in charge density when molecules are excited from ground state to excited states, while the blue color represents corresponding decreases in charge density.

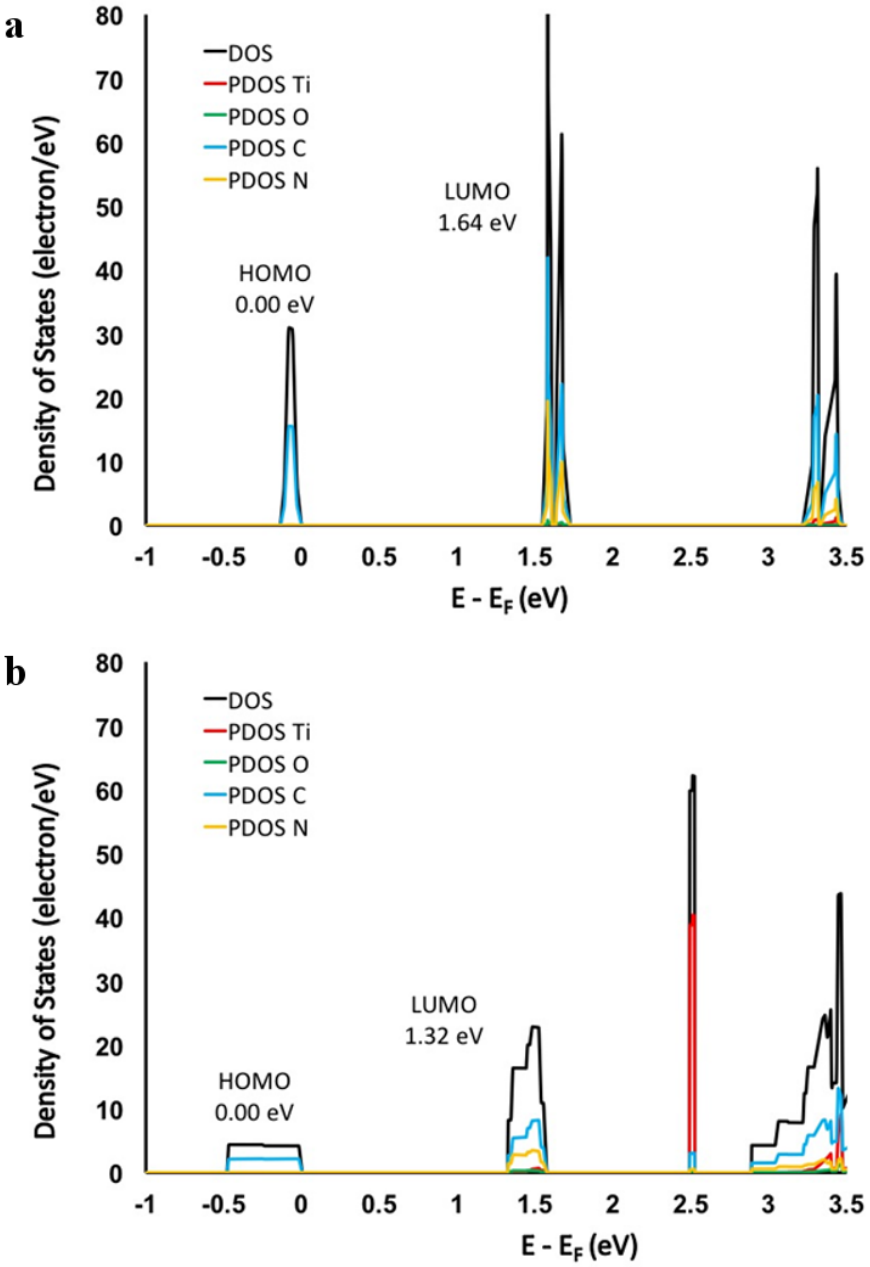

Figure 3.14. Density of states (DOS) and projected density of states (PDOS) for (a) hexagonal and (b) rectangular lattices. The grey color represents the DOS, and the PDOS for Ti, O, C and N atoms are represented in red, green, blue and yellow colors, respectively. Simulations were performed in gas phase.

REFERENCES

(1) Brumbach, M.; Placencia, D.; Armstrong, N. R. Titanyl Phthalocyanine/C_{60} Heterojunctions: Band-Edge Offsets and Photovoltaic Device Performance. *J. Phys. Chem. C* **2008,** *112*, 3142–3151.

(2) Placencia, D.; Wang, W.; Shallcross, R. C.; Nebesny, K. W.; Brumbach, M.; Armstrong, N. R. Organic Photovoltaic Cells Based On Solvent-Annealed, Textured Titanyl Phthalocyanine/C_{60} Heterojunctions. *Adv. Funct. Mater.* **2009,** *19*, 1913–1921.

(3) Placencia, D.; Wang, W.; Gantz, J.; Jenkins, J. L.; Armstrong, N. R. Highly Photoactive Titanyl Phthalocyanine Polymorphs as Textured Donor Layers in Organic Solar Cells. *J. Phys. Chem. C* **2011,** *115*, 18873–18884.

(4) Vasseur, K.; Rand, B. P.; Cheyns, D.; Temst, K.; Froyen, L.; Heremans, P. Correlating the Polymorphism of Titanyl Phthalocyanine Thin Films with Solar Cell Performance. *J. Phys. Chem. Lett.* **2012,** *3*, 2395–2400.

(5) Mayukh, M.; Macech, M. R.; Placencia, D.; Cao, Y.; Armstrong, N. R.; McGrath, D. V. Solution Processed Titanyl Phthalocyanines as Donors in Solar Cells: Photoresponse to 1000 nm. *ACS Appl. Mater. Interfaces* **2015,** *7*, 23912–23919.

(6) Sun, M.; Wang, S.; Xiao, Y.; Song, Z.; Li, X. Titanylphthalocyanine as Hole Transporting Material for Perovskite Solar Cells. *Journal of Energy Chemistry* **2015,** *24*, 756–761.

(7) Ramar, M.; Tyagi, P.; Suman, C. K.; Srivastava, R. Enhanced Carrier Transport in Tris(8-Hydroxyquinolinate) Aluminum by Titanyl Phthalocyanine Doping. *RSC Adv.* **2014,** *4*, 51256–51261.

(8) Li, L.; Tang, Q.; Li, H.; Yang, X.; Hu, W.; Song, Y.; Shuai, Z.; Xu, W.; Liu, Y.; Zhu, D. An Ultra Closely π-Stacked Organic Semiconductor for High Performance Field-Effect Transistors. *Adv. Mater.* **2007,** *19*, 2613–2617.

(9) Dong, S.; Bao, C.; Tian, H.; Yan, D.; Geng, Y.; Wang, F. ABAB-Symmetric Tetraalkyl Titanyl Phthalocyanines for Solution Processed Organic Field-Effect Transistors with Mobility Approaching 1 $cm^2\ V^{-1}\ s^{-1}$. *Adv. Mater.* **2013,** *25*, 1165–1169.

(10) Park, J. H.; Movva, H. C. P.; Chagarov, E.; Sardashti, K.; Chou, H.; Kwak, I.; Hu, K.-T.; Fullerton-Shirey, S. K.; Choudhury, P.; Banerjee, S. K.; Kummel, A. C. In Situ Observation of Initial Stage in Dielectric Growth and Deposition of Ultrahigh Nucleation Density Dielectric on Two-Dimensional Surfaces. *Nano Lett.* **2015,** *15*, 6626–6633.

(11) Law, K. Y. Organic Photoconductive Materials: Recent Trends and Developments. *Chem. Rev.* **1993,** *93*, 449–486.

(12) Mizuguchi, J.; Rihs, G.; Karfunkel, H. R. Solid-State Spectra of Titanylphthalocyanine As Viewed from Molecular Distortion. *J. Phys. Chem.* **1995,** *99*, 16217–16227.

(13) Feenstra, R. M.; Stroscio, J. A.; Tersoff, J.; Fein, A. P. Atom-Selective Imaging of The GaAs(110) Surface. *Phys. Rev. Lett.* **1987,** *58*, 1192–1195.

(14) Reddick, R. C.; Warmack, R. J.; Ferrell, T. L. New Form of Scanning Optical Microscopy. *Phys. Rev. B* **1989,** *39*, 767–770.

(15) Hamers, R. J. Atomic-Resolution Surface Spectroscopy with the Scanning Tunneling Microscope. *Annu. Rev. Phys. Chem.* **1989,** *40*, 531–559.

(16) Meixner, A. J.; Bopp, M. A.; Tarrach, G. Direct Measurement of Standing Evanescent Waves with a Photon-Scanning Tunneling Microscope. *Appl. Opt.* **1994,** *33*, 7995–8000.

(17) Berndt, R.; Gaisch, R.; Schneider, W. D.; Gimzewski, J. K.; Reihl, B.; Schlittler, R. R.; Tschudy, M. Atomic Resolution in Photon Emission Induced by a Scanning Tunneling Microscope. *Phys. Rev. Lett.* **1995,** *74*, 102–105.

(18) Takahashi, S.; Fujimoto, T.; Kato, K.; Kojima, I. High Resolution Photon Scanning Tunneling Microscope. *Nanotechnology* **1997,** *8*, A54–A57.

(19) Stipe, B. C.; Rezaei, M. A.; Ho, W. Single-Molecule Vibrational Spectroscopy and Microscopy. *Science* **1998,** *280*, 1732–1735.

(20) McCarty, G. S.; Weiss, P. S. Scanning Probe Studies of Single Nanostructures. *Chem. Rev.* **1999,** *99*, 1983–1990.

(21) Donhauser, Z. J.; Mantooth, B. A.; Kelly, K. F.; Bumm, L. A.; Monnell, J. D.; Stapleton, J. J.; Price, D. W.; Rawlett, A. M.; Allara, D. L.; Tour, J. M.; Weiss, P. S. Conductance Switching in Single Molecules through Conformational Changes. *Science* **2001,** *292*, 2303–2307.

(22) Claridge, S. A.; Schwartz, J. J.; Weiss, P. S. Electrons, Photons, and Force: Quantitative Single-Molecule Measurements from Physics to Biology. *ACS Nano* **2011,** *5*, 693–729.

(23) Kim, M.; Hohman, J. N.; Cao, Y.; Houk, K. N.; Ma, H.; Jen, A. K. Y.; Weiss, P. S. Creating Favorable Geometries for Directing Organic Photoreactions in Alkanethiolate Monolayers. *Science* **2011,** *331*, 1312–1315.

(24) Bonnell, D. A.; Basov, D. N.; Bode, M.; Diebold, U.; Kalinin, S. V.; Madhavan, V.; Novotny, L.; Salmeron, M.; Schwarz, U. D.; Weiss, P. S. Imaging Physical Phenomena with Local Probes: From Electrons to Photons. *Rev. Mod. Phys.* **2012,** *84*, 1343–1381.

(25) Wang, S.; Wattanatorn, N.; Chiang, N.; Zhao, Y.; Kim, M.; Ma, H.; Jen, A. K. Y.; Weiss, P. S. Photoinduced Charge Transfer in Single-Molecule *p–n* Junctions. *J. Phys. Chem. Lett.* **2019,** *10*, 2175–2181.

(26) Kong, X.-H.; Yang, Y.-L.; Lei, S.-B.; Wang, C. On the Topography Multiplicity of Non-Planar Titanyl (IV) Phthalocyanine Molecules and the STM Imaging Mechanism. *Surf. Sci.* **2008,** *602*, 684–692.

(27) Wei, Y.; Robey, S. W.; Reutt-Robey, J. E. TiOPc Molecular Dislocation Networks as Nanotemplates for C_{60} Cluster Arrays. *J. Am. Chem. Soc.* **2009,** *131*, 12026–12027.

(28) Wei, Y. Y.; Reutt-Robey, J. E. Directed Organization of C_{70} Kagome Lattice by Titanyl Phthalocyanine Monolayer Template. *J. Am. Chem. Soc.* **2011,** *133*, 15232–15235.

(29) Wei, Y. Y.; Reutt-Robey, J. E. Molecular Interface Formation in Titanyl Phthalocyanine-C_{60} Monolayer Films. *J. Phys. Chem. C* **2012,** *116*, 23773–23778.

(30) Liu, X.; Wei, Y.; Reutt-Robey, J. E.; Robey, S. W. Dipole–Dipole Interactions in TiOPc Adlayers on Ag. *J. Phys. Chem. C* **2014,** *118*, 3523–3532.

(31) Park, J. H.; Fathipour, S.; Kwak, I.; Sardashti, K.; Ahles, C. F.; Wolf, S. F.; Edmonds, M.; Vishwanath, S.; Xing, H. G.; Fullerton-Shirey, S. K.; Seabaugh, A.; Kummel, A. C. Atomic Layer Deposition of Al_2O_3 on WSe_2 Functionalized by Titanyl Phthalocyanine. *ACS Nano* **2016,** *10*, 6888–6896.

(32) Zhao, W.; Zhu, H.; Song, H.; Liu, J.; Chen, Q.; Wang, Y.; Wu, K. Adsorption and Assembly of Photoelectronic TiOPc Molecules on Coinage Metal Surfaces. *J. Phys. Chem. C* **2018,** *122*, 7695–7701.

(33) Vigoureux, J. M.; Girard, C.; Courjon, D. General Principles of Scanning Tunneling Optical Microscopy. *Opt. Lett.* **1989,** *14*, 1039–1041.

(34) Reddick, R. C.; Warmack, R. J.; Chilcott, D. W.; Sharp, S. L.; Ferrell, T. L. Photon Scanning Tunneling Microscopy. *Rev. Sci. Instrum.* **1990,** *61*, 3669–3677.

(35) Jiang, S.; Tomita, N.; Ohsawa, H.; Ohtsu, M. A Photon Scanning Tunneling Microscope Using an AlGaAs Laser. *Jpn. J. Appl. Phys.* **1991,** *30*, 2107–2111.

(36) Dawson, P.; de Fornel, F.; Goudonnet, J. P. Imaging of Surface Plasmon Propagation and Edge Interaction Using a Photon Scanning Tunneling Microscope. *Phys. Rev. Lett.* **1994,** *72*, 2927–2930.

(37) Feldstein, M. J.; Vohringer, P.; Wang, W.; Scherer, N. F. Femtosecond Optical Spectroscopy and Scanning Probe Microscopy. *J. Phys. Chem.* **1996,** *100*, 4739–4748.

(38) Ballard, J. B.; Carmichael, E. S.; Shi, D.; Lyding, J. W.; Gruebele, M. Laser Absorption Scanning Tunneling Microscopy of Carbon Nanotubes. *Nano Lett.* **2006,** *6*, 45–49.

(39) Shigekawa, H.; Yoshida, S.; Takeuchi, O.; Aoyama, M.; Terada, Y.; Kondo, H.; Oigawa, H. Nanoscale Dynamics Probed by Laser-Combined Scanning Tunneling Microscopy. *Thin Solid Films* **2008,** *516*, 2348–2357.

(40) Wu, S. W.; Ho, W. Two-Photon-Induced Hot-Electron Transfer to a Single Molecule in a Scanning Tunneling Microscope. *Phys. Rev. B* **2010,** *82*, 085444.

(41) Atkin, J. M.; Berweger, S.; Jones, A. C.; Raschke, M. B. Nano-Optical Imaging and Spectroscopy of Order, Phases, and Domains in Complex Solids. *Adv. Phys.* **2012,** *61*, 745–842.

(42) Nienhaus, L.; Goings, J. J.; Nguyen, D.; Wieghold, S.; Lyding, J. W.; Li, X. S.; Gruebele, M. Imaging Excited Orbitals of Quantum Dots: Experiment and Electronic Structure Theory. *J. Am. Chem. Soc.* **2015,** *137*, 14743–14750.

(43) Nienhaus, L.; Wieghold, S.; Nguyen, D.; Lyding, J. W.; Scott, G. E.; Gruebele, M. Optoelectronic Switching of a Carbon Nanotube Chiral Junction Imaged with Nanometer Spatial Resolution. *ACS Nano* **2015,** *9*, 10563–10570.

(44) Cocker, T. L.; Peller, D.; Yu, P.; Repp, J.; Huber, R. Tracking the Ultrafast Motion of a Single Molecule by Femtosecond Orbital Imaging. *Nature* **2016,** *539*, 263–267.

(45) Nguyen, D.; Nguyen, H. A.; Lyding, J. W.; Gruebele, M. Imaging and Manipulating Energy Transfer Among Quantum Dots at Individual Dot Resolution. *ACS Nano* **2017,** *11*, 6328–6335.

(46) Mazur, U.; Leonetti, M.; English, W. A.; Hipps, K. W. Spontaneous Solution-Phase Redox Deposition of a Dense Cobalt(II) Phthalocyanine Monolayer on Gold. *The Journal of Physical Chemistry B* **2004,** *108*, 17003–17006.

(47) Kresse, G.; Furthmüller, J. Efficient Iterative Schemes for *ab initio* Total-Energy Calculations Using a Plane-Wave Basis Set. *Phys. Rev. B* **1996,** *54*, 11169–11186.

(48) Kresse, G.; Furthmüller, J. Efficiency of *ab-initio* Total Energy Calculations for Metals and Semiconductors using a Plane-Wave Basis Set. *Comput. Mater. Sci.* **1996,** *6*, 15–50.

(49) Kresse, G.; Hafner, J. *Ab initio* Molecular Dynamics for Liquid Metals. *Phys. Rev. B* **1993,** *47*, 558–561.

(50) Kresse, G.; Hafner, J. *Ab initio* Molecular-Dynamics Simulation of the Liquid-Metal--Amorphous-Semiconductor Transition in Germanium. *Phys. Rev. B* **1994,** *49*, 14251–14269.

(51) Blöchl, P. E. Projector Augmented-Wave Method. *Phys. Rev. B* **1994,** *50*, 17953–17979.

(52) Kresse, G.; Joubert, D. From Ultrasoft Pseudopotentials to the Projector Augmented-Wave Method. *Phys. Rev. B* **1999,** *59*, 1758–1775.

(53) Perdew, J. P.; Burke, K.; Ernzerhof, M. Generalized Gradient Approximation Made Simple. *Phys. Rev. Lett.* **1996,** *77*, 3865–3868.

(54) Perdew, J. P.; Burke, K.; Ernzerhof, M. Generalized Gradient Approximation Made Simple [Phys. Rev. Lett. 77, 3865 (1996)]. *Phys. Rev. Lett.* **1997,** *78*, 1396–1396.

(55) Momma, K.; Izumi, F. VESTA 3 for Three-Dimensional Visualization of Crystal, Volumetric and Morphology Data. *J. Appl. Crystallogr.* **2011,** *44*, 1272–1276.

(56) Tersoff, J.; Hamann, D. R. Theory and Application for the Scanning Tunneling Microscope. *Phys. Rev. Lett.* **1983,** *50*, 1998–2001.

(57) Nguyen, D.; Goings, J. J.; Nguyen, H. A.; Lyding, J.; Li, X. S.; Gruebele, M. Orientation-Dependent Imaging of Electronically Excited Quantum Dots. *J. Chem. Phys.* **2018,** *148*, 064701.

(58) Eigler, D. M.; Weiss, P. S.; Schweizer, E. K.; Lang, N. D. Imaging Xe with a Low-Temperature Scanning Tunneling Microscope. *Phys. Rev. Lett.* **1991,** *66*, 1189–1192.

(59) Sautet, P.; Joachim, C. Interpretation of STM Images: Copper-Phthalocyanine on Copper. *Surf. Sci.* **1992,** *271*, 387–394.

(60) Chavy, C.; Joachim, C.; Altibelli, A. Interpretation of STM Images: C_{60} on the Gold (110) Surface. *Chem. Phys. Lett.* **1993,** *214*, 569–575.

(61) Vion, D.; Orfila, P. F.; Joyez, P.; Esteve, D.; Devoret, M. H. Miniature Electrical Filters for Single Electron Devices. *J. Appl. Phys.* **1995,** *77*, 2519–2524.

(62) Bumm, L. A.; Arnold, J. J.; Dunbar, T. D.; Allara, D. L.; Weiss, P. S. Electron Transfer through Organic Molecules. *J. Phys. Chem. B* **1999,** *103*, 8122–8127.

(63) Pascual, J. I.; Gómez-Herrero, J.; Rogero, C.; Baró, A. M.; Sánchez-Portal, D.; Artacho, E.; Ordejón, P.; Soler, J. M. Seeing Molecular Orbitals. *Chem. Phys. Lett.* **2000,** *321*, 78–82.

(64) Pascual, J. I.; Jackiw, J. J.; Song, Z.; Weiss, P. S.; Conrad, H.; Rust, H. P. Adsorbate-Substrate Vibrational Modes of Benzene on Ag(110) Resolved with Scanning Tunneling Spectroscopy. *Phys. Rev. Lett.* **2001,** *86*, 1050–1053.

(65) Villagomez, C. J.; Zambelli, T.; Gauthier, S.; Gourdon, A.; Stojkovic, S.; Joachim, C. STM Images of a Large Organic Molecule Adsorbed on a Bare Metal Substrate or on a Thin Insulating Layer: Visualization of HOMO and LUMO. *Surf. Sci.* **2009,** *603*, 1526–1532.

(66) Pham, B. Q.; Gordon, M. S. Can Orbitals Really Be Observed in Scanning Tunneling Microscopy Experiments? *J. Phys. Chem. A* **2017,** *121*, 4851–4852.

(67) Puschnig, P.; Boese, A. D.; Willenbockel, M.; Meyer, M.; Lüftner, D.; Reinisch, E. M.; Ules, T.; Koller, G.; Soubatch, S.; Ramsey, M. G.; Tautz, F. S. Energy Ordering of Molecular Orbitals. *J. Phys. Chem. Lett.* **2017,** *8*, 208–213.

(68) Krukau, A. V.; Vydrov, O. A.; Izmaylov, A. F.; Scuseria, G. E. Influence of the Exchange Screening Parameter on the Performance of Screened Hybrid Functionals. *J. Chem. Phys.* **2006,** *125*, 224106.

(69) Egbe, D. A. M.; Türk, S.; Rathgeber, S.; Kühnlenz, F.; Jadhav, R.; Wild, A.; Birckner, E.; Adam, G.; Pivrikas, A.; Cimrova, V.; Knör, G.; Sariciftci, N. S.; Hoppe, H. Anthracene Based Conjugated Polymers: Correlation between π−π-Stacking Ability, Photophysical Properties, Charge Carrier Mobility, and Photovoltaic Performance. *Macromolecules* **2010,** *43*, 1261–1269.

(70) Giri, G.; Verploegen, E.; Mannsfeld, S. C. B.; Atahan-Evrenk, S.; Kim, D. H.; Lee, S. Y.; Becerril, H. A.; Aspuru-Guzik, A.; Toney, M. F.; Bao, Z. Tuning Charge Transport in Solution-Sheared Organic Semiconductors Using Lattice Strain. *Nature* **2011,** *480*, 504–508.

(71) Okamoto, T.; Nakahara, K.; Saeki, A.; Seki, S.; Oh, J. H.; Akkerman, H. B.; Bao, Z.; Matsuo, Y. Aryl−Perfluoroaryl Substituted Tetracene: Induction of Face-to-Face π−π Stacking and Enhancement of Charge Carrier Properties. *Chem. Mater.* **2011,** *23*, 1646–1649.

(72) Mei, J.; Diao, Y.; Appleton, A. L.; Fang, L.; Bao, Z. Integrated Materials Design of Organic Semiconductors for Field-Effect Transistors. *J. Am. Chem. Soc.* **2013,** *135*, 6724–6746.

CHAPTER 4

Formation of Highly Ordered Terminal Alkyne Self-Assembled Monolayers on Au{111} Surface through Substitution of 1-Decaboranethiolate

(Adapted from: Wang, S.; Goronzy, D. P.; Young, T. D.; Wattanatorn, N.; Stewart, L.; Baše, T.; Weiss, P. S. Formation of Highly Ordered Terminal Alkyne Self-Assembled Monolayers on the Au{111} Surface through Substitution of 1-Decaboranethiolate. *J. Phys. Chem. C* **2019,** *123*, 1348-1353.)

4.1 Introduction

Terminal alkyne self-assembled monolayers (SAMs) have received increasing attention,[1-6] since they offer a way to form covalent Au-C σ bonds that are an alternative to Au-thiolate and other conventional anchoring groups.[3,7-11] However, reports of highly ordered terminal alkyne SAMs on gold surfaces have been rare since alkynyl groups tend to be oxidized during the formation of the SAMs, resulting in disordered structures.[6] Highly ordered terminal alkyne SAMs have been obtained when assembly was performed in an oxygen-free environment.[4] This oxygen-free constraint for getting high-quality terminal alkyne SAMs restricts such surfaces for further detailed studies and applications.

In an attempt to fabricate SAMs with molecular level mixed electron donor and acceptor molecules, we studied the reactivity of 1-decaboranethiolate (Figure 4.1a) SAMs on Au{111}. However, we find out that the reaction aimed at completing and closing the open cages of 1-decaboranethiolate with 4-phenyl-1-butyne (4p1b, Figure 4.1b) results in highly ordered monolayers of 4-phenyl-1-butyne. 4-Phenyl-1-butyne can react with the bridging hydrogen atoms on the open cage of 1-decaboranethiol under the catalysis of acetonitrile and form *o*-carboranethiol derivatives.[12] The heat released by the reaction caused the desorption of the original 1-decaboranethiol SAM and 4p1b molecules fill in the remaining vacancies and form ordered structures. Exothermic reaction-induced disorder in SAMs has been observed previously for Fischer esterification reactions and was used to make regions of the monolayer labile to displacement.[13] This disorder is important in *enabling* displacement. Defects in SAMs, such as domain boundaries, are necessary as they serve as nucleation sites for displacement (and insertion), as shown both for SAMs of molecules with both linear and rigid-cage backbones.[13-19] The

substitution process was characterized here by scanning tunneling microscopy (STM). 1-Decaboranethiol SAMs are disordered but the SAMs formed by 4p1b after the substitution are consistent with the $(\sqrt{3} \times \sqrt{3})R30°$ lattice on Au{111}. Grazing incidence Fourier transform infrared (FTIR) spectroscopy results indicate that the process occurs gradually and X-ray photoelectron spectroscopy (XPS) confirms the ultimate complete substitution of 1-decaboranethiolate moieties.

4.2 Experimental Methods

4.2.1 Materials

4-Phenyl-1-butyne (Sigma-Aldrich, St. Louis, MO), dichloromethane and acetonitrile were used as received. 1-Decaboranethiol was synthesized and purified as previously described.[20] 1-Decaboranethiol SAMs were prepared by immersing freshly flame-annealed Au{111} on mica and Au{111} on silicon substrates into gravimetrically prepared 1 mM CH_2Cl_2 solutions of 1-decaboranethiol for 24 h at room temperature. Substrates were then rinsed thoroughly with CH_2Cl_2 and were blown dry using nitrogen.

4.2.2 Reaction Between 1-Decaboranethiolate and 4-Phenyl-1-butyne

Substrates with 1-decaboranethiol SAMs were immersed in acetonitrile. The solutions were maintained at 82 ℃ for 2 h before 4-phenyl-1-butyne was added to prepare a 0.02 M solution. The reaction was then allowed to continue at 82 ℃ for another 24 or 48 h and the substrates were then rinsed thoroughly by acetonitrile and blown dry using nitrogen.

4.2.3 Scanning Tunneling Microscopy

All STM measurements were conducted using a custom beetle-style STM under ambient conditions.[21] Piezoelectric scanner gains were calibrated using the lattice spacing of a known

adsorbate, 1-dodecanethiolate on Au{111}. The measured spacings of the alkanethiolate SAMs were measured in a variety of scanning directions. The vertical scale was calibrated using the monatomic step heights of the Au{111} substrate in subsequent images.

4.2.4 Grazing Incidence Fourier Transform Infrared Spectroscopy

Infrared spectra were collected using a Nicolet 6700 FTIR spectrometer (Thermo Electron Corp., Waltham, MA) equipped with a liquid-nitrogen-cooled mercury-cadmium-telluride detector and a Seagull variable-angle reflection accessory (Harrick Scientific, Inc., Ossining, NY). A FTIR Purge Gas Generator (Parker-Balston, Cleveland, OH) removed water and CO_2 from the gas stream used to purge the spectrometer and its accessory. The data were collected at grazing incidence (82° relative to the surface normal) in reflection mode with *p*-polarized light and a mirror speed of 1.27 cm/s, with a resolution of 8 cm^{-1}. All spectra were averaged over 1024 scans. Scans were normalized with spectra of perdeuterated *n*-dodecanethiolate monolayers on Au{111}.

4.3 Results and Discussion

4.3.1 Self-Assembly of 1-Decaboranethiol

Self-assembled monolayers of 1-decaboranethiol were prepared by immersing flame-annealed Au{111} on mica substrates into gravimetrically prepared 1 mM CH_2Cl_2 solutions of 1-decaboranethiol for 24 h at room temperature. The substrates were then characterized by a custom beetle-style STM under ambient conditions.[22] The STM images in Figure 4.2 show that 1-decaboranethiolate molecules in the SAM tend to form small clusters rather than long-range ordered nanostructures, which results in evenly distributed vacancies within the SAMs (displayed as dark regions).

The random cluster pattern on the surface, which is characterized by many disordered and varied protrusions (Figure 4.2b), can be explained by the lower symmetry of the molecules compared to upright, symmetric carboranethiols[23] and their different orientations with regard to the surface. The difference in the interactions between neighboring molecules results in different tilt angles and thus different intermolecular distances (Figure 4.3b). The lack of long-range order and the molecular tilt make it difficult to extract useful information about the assembly structure under ambient conditions at room temperature.

4.3.2 Reaction of 1-Decaboranethiol with the Alkynyl Group

The four acidic bridging hydrogen atoms in decaborane enable it to react with alkynyl groups catalyzed by acetonitrile through the steps shown in Scheme 1.[12]

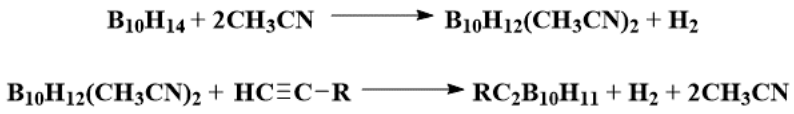

Scheme 1. Reaction of decaborane with alkynyl group catalyzed by acetonitrile.

4-Phenyl-1-butyne (4p1b) was used to study the reactivity of 1-decaboranethiol assembled on the Au surface. A 1-decaboranethiol SAM was prepared on flame-annealed Au{111} on a mica substrate and then the substrate was immersed in acetonitrile to prepare the bis-(acetonitrile)decaborane adduct, which is necessary for the formation of *ortho*-carborane by the insertion of an alkyne moiety in the open decaborane cage. The solution was maintained at 82 ℃ for 2 h before 4-phenyl-1-butyne was added. The reaction was held at 82 ℃ for another 48 h and the substrate was then washed with acetonitrile. Scanning tunneling microscopy images of the surface after the reaction (Figure 4.4a,b) show that the molecules formed ordered structures on the surface, which are *not* observed for 1-decaboranethiol SAMs. We note that the heat of the reaction

on the surface can have a substantial effect on ordering (or disordering) reactions of monolayers or inserted molecules, as we have previously observed in a number of systems.[13,22,24]

Fourier transforms of the images in Figure 4.4a,b yield nearest neighbor spacings of 5.04 ± 0.09 Å. The structure is consistent with the $(\sqrt{3} \times \sqrt{3})R30°$ lattice, which characterizes the structure formed by alkanethiols and ordered terminal alkynes[4] on Au{111}, but is substantially more dense than typical carboranethiolate SAMs.[23] Such results indicate that the ordered SAMs we observed are formed purely by 4p1b and 1-decaboranethiolate molecules were driven away after reaction with 4p1b. The complete removal of 1-decaborane molecules was further confirmed by X-ray photoelectron spectroscopy (XPS) analysis. The XPS data in Figure 4.5a show that there is no boron left on the surface indicating that 1-decaboranethiolates were completely substituted by 4p1b after the reaction.

Detailed analysis of the O 1s spectrum (Figure 4.5b) shows two peaks with binding energies of 533.2 eV and 531.2 eV, indicating that oxidized species (carboxyl group) exist on the surface. Deconvolution of C 1s spectrum (Figure 4.5c) gives two peaks with binding energies of 285.5 eV and 284.3 eV, which we assign to carbon atoms of the aromatic ring. The signal representing carbon atoms in oxidized species at 288 eV is negligible, suggesting that the defects observed in the STM images in Figure 4.4 might be formed by these oxidized species.

In order to test and to understand the substitution process, we immersed a 1-decaboranethiol SAM prepared on Au{111} in pure acetonitrile for 24 h at 82 ℃; the STM images characterizing the surface are shown as Figure 4.6a,b. Also shown in Figure 4.6 are the images for the surfaces where the substitution of 1-decaboranethiolate with 4p1b was carried out for 24 h (Figure 4.6c,d) and 48 h (Figure 4.6e,f), respectively. The roughness of the SAM increased after

1-decaboranethiolate reacted with acetonitrile (Figure 4.6a,b), but the SAM remained disordered (*cf*. Fig. 4.2). We assign the evenly distributed protrusions to the acetonitrile decaborane adducts formed by the reaction between basic acetonitrile and the acidic bridging H atoms of the open decaborane cage.

Figure 4.6c,d shows the surface after 1-decaboranethiol SAM was reacted with 4p1b for 24 h. There are regions of the surface with different apparent heights in STM images, and the shapes of the regions are irregular. Such patterns are *not* observed on the surface after the reaction with 4p1b took place for 48 h (Figure 4.6e,f), where the regions with greater apparent height appear to be relatively intact. The differences in the surface patterns indicate that the substitution of 1-decaboranethiolate by 4p1b starts randomly on the surface and proceeds until all 1-decaboranethiolate molecules have been replaced.[17,18]

In order to test if the ordered structures of 4p1b were formed because of the reaction followed by the substitution of 1-decaboranethiolates, we performed a control experiment where the 1-decaboranethiol SAM was immersed in 0.02 M ethanol solution of 4p1b for 24 h at 78 °C. Scanning tunneling microscopy images characterizing the surface are shown in Figure 4.7a,b. No ordered structure was observed in the STM images, which means that 4p1b molecules can only form ordered SAMs after reacting with 1-decaboranethiol SAMs. We assign the protrusions scattered on the surface in Figure 4.7a,b to 4p1b molecules inserted into the evenly distributed pinhole defects in 1-decaboranethiol SAMs.

We also immersed clean Au{111}/mica substrate in 0.02 M acetonitrile solution of 4p1b for 48 h at 82 ℃ to see if 4p1b itself can form ordered SAMs in air. As seen in the STM images of the surface in Figure 4.7c,d, we observe strip-like structures formed along different directions, which

are *not* found in the STM images of the ordered 4p1b SAMs in Figures 4.4 and 4.6e,f. Such strip structures can be explained by previous reports that the AuC≡CR bond can be oxidized by O_2 during the SAMs formation and the molecules then lie flat on the surface.[4,6] The absence of strip structures in the ordered 4p1b SAMs in Figures 4.4 and 4.6e,f indicates that the gradual reaction and substitution of 1-decaboranethiol SAMs facilitates the formation of highly ordered 4p1b SAMs.

The substitution process was also characterized by grazing incidence FTIR. 1-Decaboranethiol SAMs were prepared on Au{111} on Si substrates and the substitution was carried out by immersing the samples in 0.02 M acetonitrile solution of 4p1b for 24 h and 48 h separately at 82 ℃. Examples of the FTIR spectra for both substrates and for pure 1-decaboranethiol SAM are shown in Figure 4.8a. A spectrum for the surface prepared by immersing clean Au{111}/mica in the same solution at 82 ℃ for 48 h is also shown in Figure 4.8a for comparison. The method we use is more sensitive to the fingerprint region;[6] so, in the 1-decaboranethiol SAM spectrum, the intensity of the peak at 2550 cm^{-1}, which represents the B-H stretching vibration is small compared to the bridging hydrogen peak (B-H-B) at 1450 cm^{-1}.[25] From the spectra characterizing the surfaces after 24 and 48 h substitution, we observe a new peak at 1650 cm^{-1}, and the intensity of the broad peak at 1450 cm^{-1} decreased after 24 h substitution and disappeared after 48 h substitution. Through the 4p1b direct deposition spectrum, we assign the peak at 1650 cm^{-1} to the aromatic ring stretch of 4p1b. The results suggest that the substitution occurs gradually, which corresponds to the STM images characterizing the process in Figure 4.6. 1-Dodecane-d_{25}-thiol SAM was used as the background to obtain the IR spectra, and the negative peaks at ~2200 cm^{-1} are due to the stretches of C-D bonds. However, there is a signal in the 48 h substitution spectrum at ~2200 cm^{-1}

that overlapped with the background C-D stretching. In order to extract the information, we used 1-decaboranethiol SAM as background to obtain the same spectrum again, shown in Figure 8b. We assign the two peaks at 2206 and 2163 cm^{-1} as the stretch of the alkynyl group, suggesting that most of the alkynyl groups are *not* oxidized during the substitution of 1-decaboranethiolate, which results in the highly ordered SAMs observed by the STM.

4.4 Conclusions and Prospects

In this study, we characterized the reaction between 1-decaboranethiol SAM and 4-phenyl-1-butyne on Au{111} surface by STM, XPS, and FTIR. We observed a $(\sqrt{3} \times \sqrt{3})R30°$ lattice on Au{111} after exposure of 1-decaboranethiol SAMs to 4p1b. X-ray photoelectron spectroscopy results suggest that 1-decaboranethiolate molecules were completely substituted by 4p1b molecules after the reaction; control experiments indicate that the complete substitution of 1-decaboranethiolate only happens in acetonitrile solution so the reaction between 1-decaboranethiolate and alkynyl group is necessary for the displacement process. Scanning tunneling microscopy results and IR spectra also show that the substitution of 1-decaboranethiolate moieties by 4p1b starts at random sites on the surface and proceeds until all the 1-decaboranethiolate molecules are completely removed. This process provides a facile way to fabricate highly ordered terminal alkyne SAMs in air that cannot be achieved through direct deposition of alkynes. The 4p1b solution after the substitution is also worth testing further since our results indicate that *o*-carboranethiolate molecules were desorbed from the surface after the reaction and should be in solution. Furthermore, the evenly distributed defects in the 1-decaboranethiol SAM provides the possibility of inserting other molecules and fabricating blended SAMs on the surface.[14,16,19,26,27]

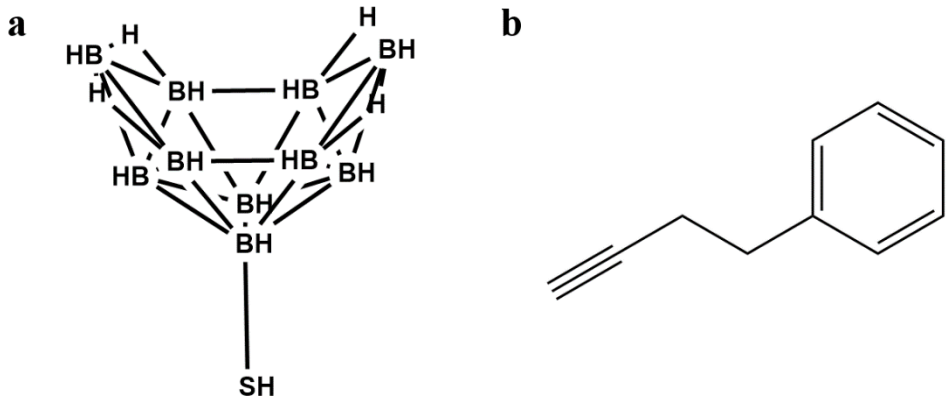

Figure 4.1. Molecular structure of (a) 1-decaboranethiol and (b) 4-phenyl-1-butyne.

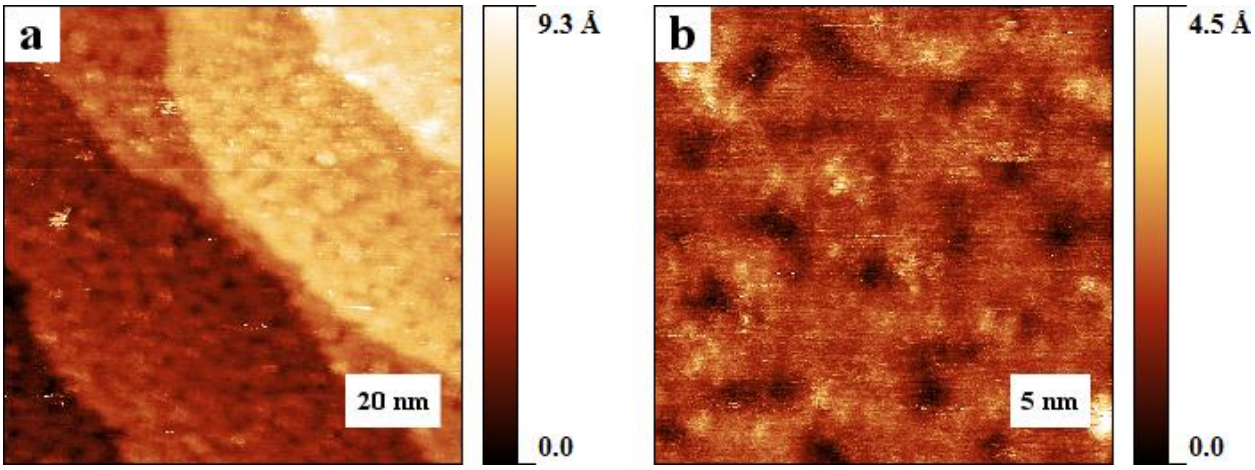

Figure 4.2. Scanning tunneling microscopy images of 1-decaboranethiol self-assembled monolayers at the scales of (a) 100 nm × 100 nm and (b) 30 nm × 30 nm on Au{111}. All images were collected at a sample bias of +1.00 V and a tunneling current of 12.0 pA.

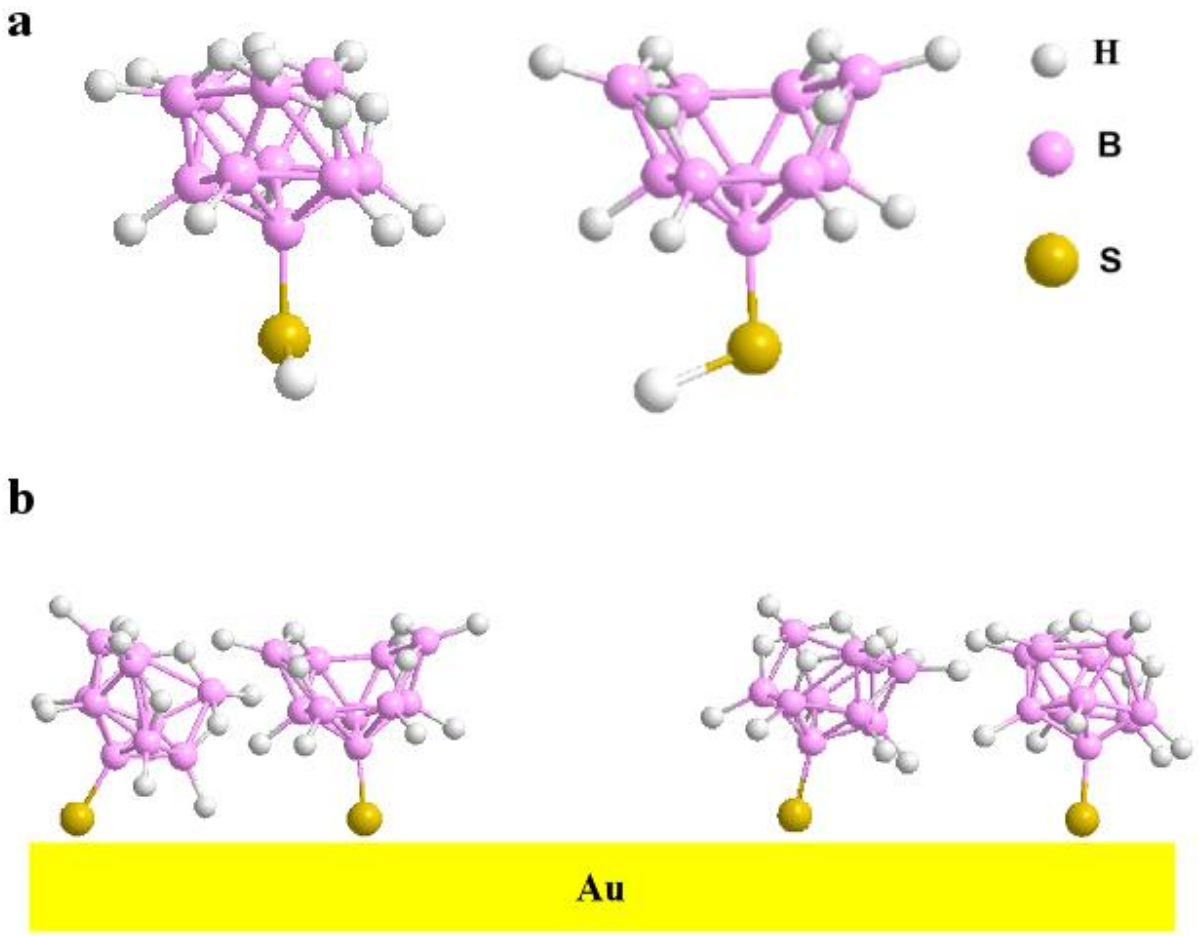

Figure 4.3. (a) Molecular structure of 1-decaboranethiol viewed from different angles. (b) Diagram explaining the formation of vacancies in self-assembled monolayers of 1-decaboranethiol.

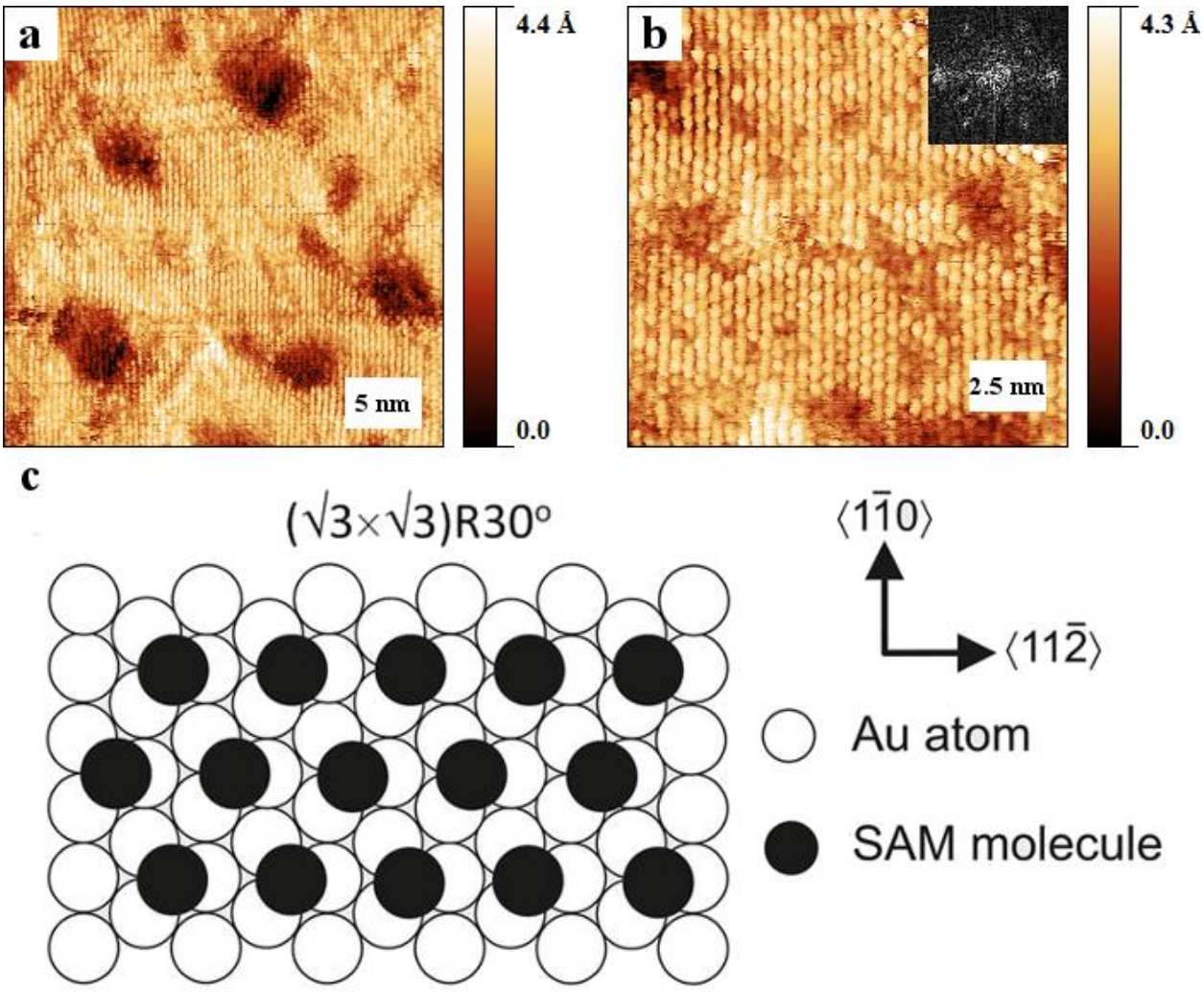

Figure 4.4. Scanning tunneling microscopy images of 1-decaboranethiol self-assembled monolayer after reaction with 4-phenyl-1-butyne in acetonitrile at the scale of (a) 30 nm × 30 nm and (b) 15 nm × 15 nm. The inset shows the Fourier transform of (b) from which the nearest neighbor spacing was calculated. All images were collected at a sample bias of +1.00 V and a tunneling current of 12.0 pA. (c) Scheme of the (√3 × √3)*R*30° lattice.

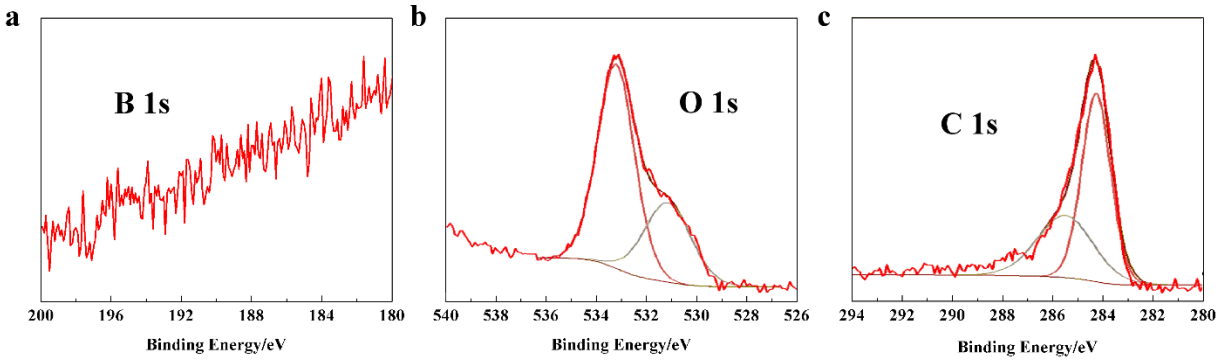

Figure 4.5. X-ray photoelectron spectra of 1-decaboranethiol self-assembled monolayer after reaction with 4-phenyl-1-butyne for 48 h in acetonitrile for (a) B 1s, (b) O 1s, and (c) C 1s.

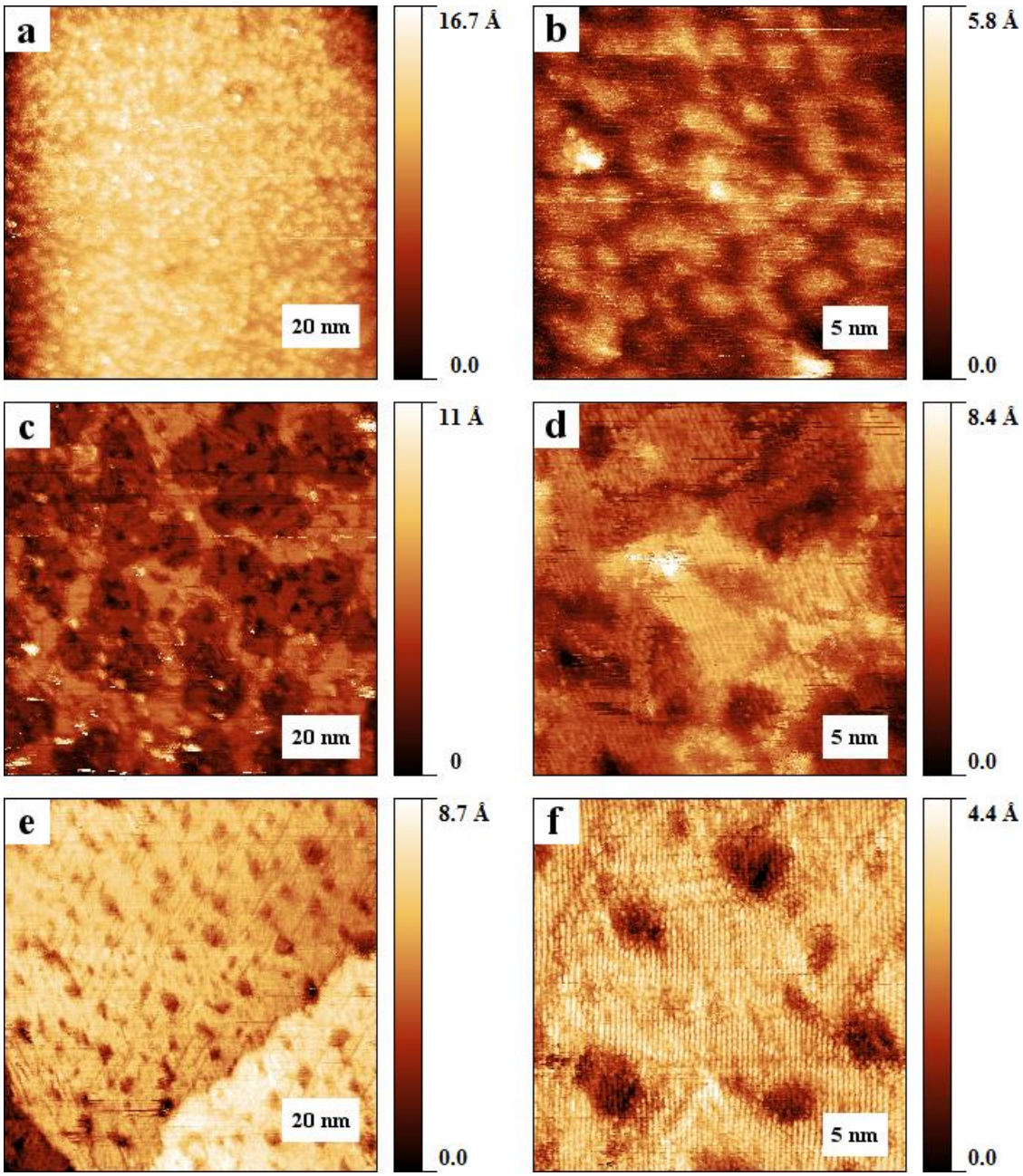

Figure 4.6. (a,b) 1-decaboranethiol self-assembled monolayer (SAM) reacted with acetonitrile at 82 ℃ for 24 h. (c,d) 1-decaboranethiol SAM reacted with 4p1b at 82 ℃ for 24 h. (e,f) 1-decaboranethiol SAM reacted with 4p1b at 82 ℃ for 48 h. All images were collected at a sample bias of +1.00 V and a tunneling current of 12.0 pA.

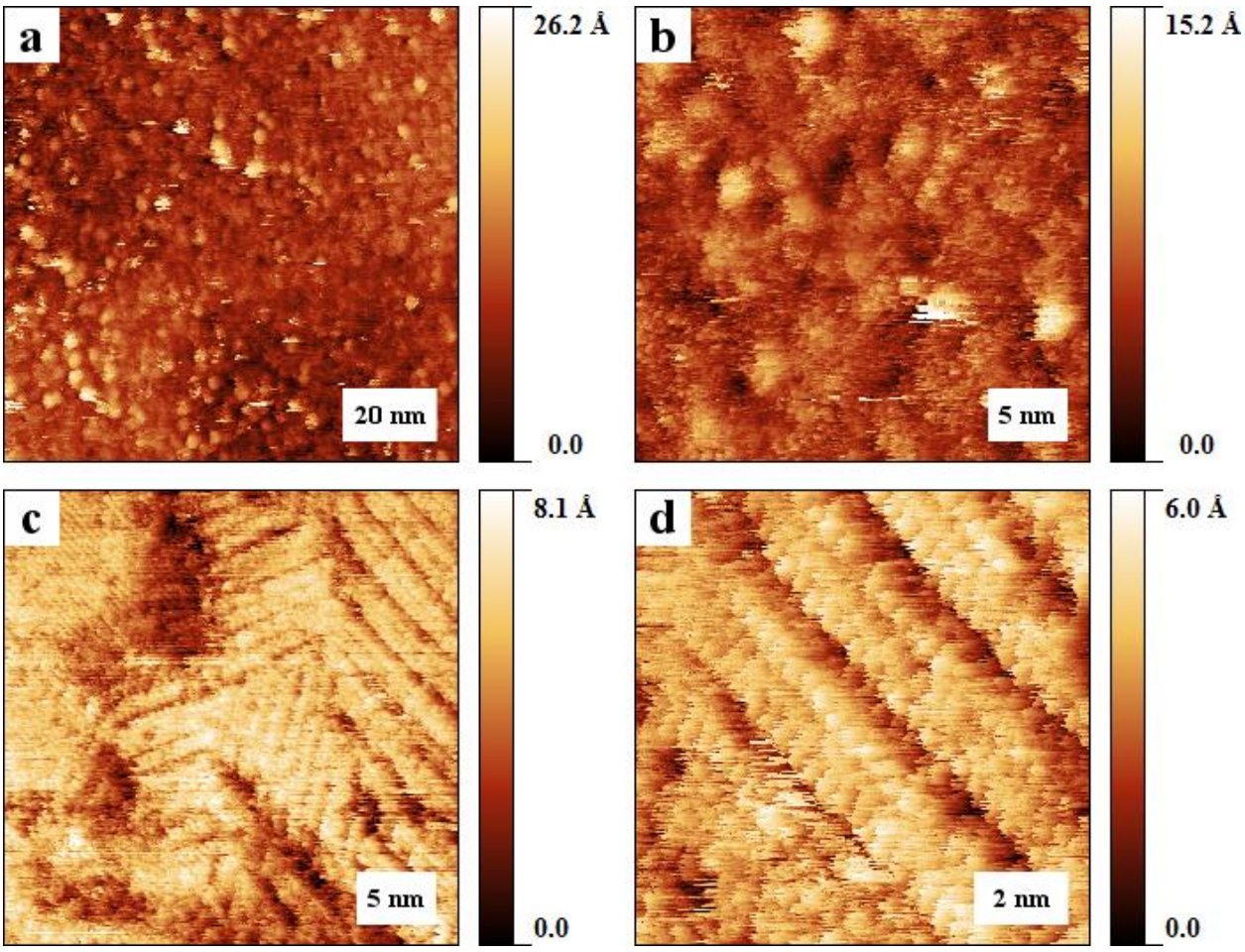

Figure 4.7. (a,b) Scanning tunneling microscopy images of 1-decaboranethiol self-assembled monolayers (SAMs) immersed in ethanol solution of 4p1b at the scale of 100 nm × 100 nm and 30 nm × 30 nm. (c,d) Scanning tunneling microscopy images of 4-phenyl-1-butyne SAMs directly deposited on Au{111} at the scale of 30 nm × 30 nm and 10 nm × 10 nm. All images were collected at a sample bias of +1.00 V and a tunneling current of 12.0 pA.

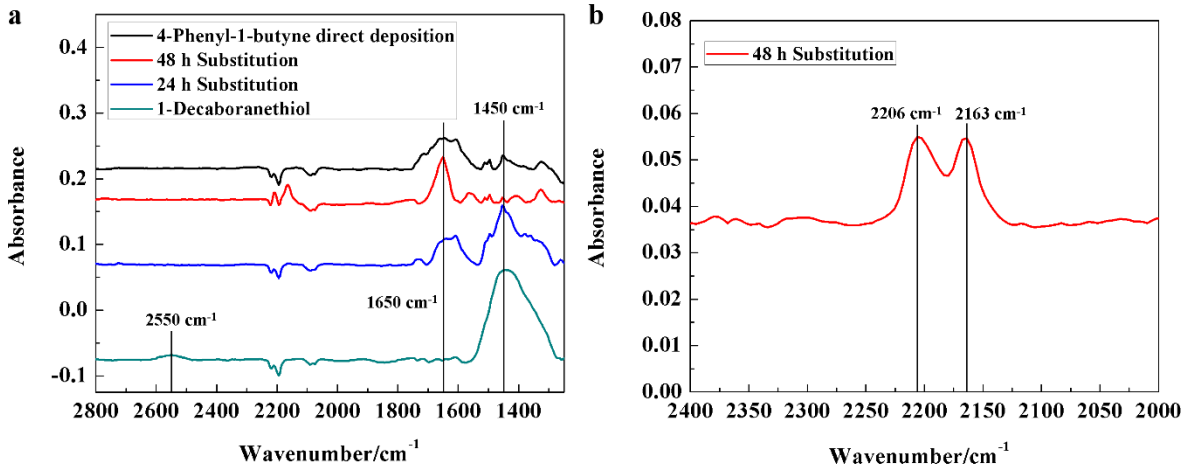

Figure 4.8. (a) Fourier transform infrared spectra of: 1-decaboranethiol self-assembled monolayers (SAMs) on a gold surface (green line), 1-decaboranethiol SAMs substituted by 4-phenyl-1-butyne for 24 h (blue line) and 48 h (red line), and 4-phenyl-1-butyne SAMs prepared by direct deposition on clean gold surface in air (black line). (b) Fourier transform infrared spectrum of 1-decaboranethiol SAMs substituted by 4-phenyl-1-butyne for 48 h obtained using 1-decaboranethiol SAMs as background.

REFERENCES

(1) Pla-Vilanova, P.; Aragones, A. C.; Ciampi, S.; Sanz, F.; Darwish, N.; Diez-Perez, I. The Spontaneous Formation of Single-Molecule Junctions via Terminal Alkynes. *Nanotechnology* **2015,** *26*, 381001.

(2) Fu, Y.; Chen, S.; Kuzume, A.; Rudnev, A.; Huang, C.; Kaliginedi, V.; Baghernejad, M.; Hong, W.; Wandlowski, T.; Decurtins, S.; Liu, S.-X. Exploitation of Desilylation Chemistry in Tailor-Made Functionalization on Diverse Surfaces. *Nat. Commun.* **2015,** *6*, 6403.

(3) Bowers, C. M.; Liao, K. C.; Zaba, T.; Rappoport, D.; Baghbanzadeh, M.; Breiten, B.; Krzykawska, A.; Cyganik, P.; Whitesides, G. M. Characterizing the Metal - SAM Interface in Tunneling Junctions. *ACS Nano* **2015,** *9*, 1471–1477.

(4) Zaba, T.; Noworolska, A.; Bowers, C. M.; Breiten, B.; Whitesides, G. M.; Cyganik, P. Formation of Highly Ordered Self-Assembled Monolayers of Alkynes on Au(111) Substrate. *J. Am. Chem. Soc.* **2014,** *136*, 11918–11921.

(5) Fracasso, D.; Kumar, S.; Rudolf, P.; Chiechi, R. C. Self-Assembled Monolayers of Terminal Acetylenes as Replacements for Thiols in Bottom-Up Tunneling Junctions. *RSC Adv.* **2014,** *4*, 56026–56030.

(6) McDonagh, A. M.; Zareie, H. M.; Ford, M. J.; Barton, C. S.; Ginic-Markovic, M.; Matisons, J. G. Ethynylbenzene Monolayers on Gold: A Metal-Molecule Binding Motif Derived from a Hydrocarbon. *J. Am. Chem. Soc.* **2007,** *129*, 3533–3538.

(7) Monnell, J. D.; Stapleton, J. J.; Dirk, S. M.; Reinerth, W. A.; Tour, J. M.; Allara, D. L.; Weiss, P. S. Relative Conductances of Alkaneselenolate and Alkanethiolate Monolayers on Au{111}. *J. Phys. Chem. B* **2005,** *109*, 20343–20349.

(8) Chen, W.; Widawsky, J. R.; Vázquez, H.; Schneebeli, S. T.; Hybertsen, M. S.; Breslow, R.; Venkataraman, L. Highly Conducting π-Conjugated Molecular Junctions Covalently Bonded to Gold Electrodes. *J. Am. Chem. Soc.* **2011,** *133*, 17160–17163.

(9) Cheng, Z. L.; Skouta, R.; Vazquez, H.; Widawsky, J. R.; Schneebeli, S.; Chen, W.; Hybertsen, M. S.; Breslow, R.; Venkataraman, L. In Situ Formation of Highly Conducting Covalent Au–C Contacts for Single-Molecule Junctions. *Nat. Nanotech.* **2011,** *6*, 353–357.

(10) Hong, W.; Li, H.; Liu, S.-X.; Fu, Y.; Li, J.; Kaliginedi, V.; Decurtins, S.; Wandlowski, T. Trimethylsilyl-Terminated Oligo(phenylene ethynylene)s: An Approach to Single-Molecule Junctions with Covalent Au–C σ-Bonds. *J. Am. Chem. Soc.* **2012,** *134*, 19425–19431.

(11) Widawsky, J. R.; Chen, W.; Vázquez, H.; Kim, T.; Breslow, R.; Hybertsen, M. S.; Venkataraman, L. Length-Dependent Thermopower of Highly Conducting Au–C Bonded Single Molecule Junctions. *Nano Lett.* **2013,** *13*, 2889–2894.

(12) Heying, T. L.; Ager, J. W.; Clark, S. L.; Mangold, D. J.; Goldstein, H. L.; Hillman, M.; Polak, R. J.; Szymanski, J. W. A New Series of Organoboranes. 1. Carboranes From Reaction of Decaborane with Acetylenic Compounds. *Inorg. Chem.* **1963,** *2*, 1089–1092.

(13) Saavedra, H. M.; Thompson, C. M.; Hohman, J. N.; Crespi, V. H.; Weiss, P. S. Reversible Lability by in Situ Reaction of Self-Assembled Monolayers. *J. Am. Chem. Soc.* **2009,** *131*, 2252–2259.

(14) Cygan, M. T.; Dunbar, T. D.; Arnold, J. J.; Bumm, L. A.; Shedlock, N. F.; Burgin, T. P.; Jones, L.; Allara, D. L.; Tour, J. M.; Weiss, P. S. Insertion, Conductivity, and Structures of Conjugated Organic Oligomers in Self-Assembled Alkanethiol Monolayers on Au{111}. *J. Am. Chem. Soc.* **1998,** *120*, 2721–2732.

(15) Donhauser, Z. J.; Price, D. W.; Tour, J. M.; Weiss, P. S. Control of Alkanethiolate Monolayer Structure Using Vapor-Phase Annealing. *J. Am. Chem. Soc.* **2003,** *125*, 11462–11463.

(16) Mullen, T. J.; Srinivasan, C.; Hohman, J. N.; Gillmor, S. D.; Shuster, M. J.; Horn, M. W.; Andrews, A. M.; Weiss, P. S. Microcontact Insertion Printing. *Appl. Phys. Lett.* **2007,** *90*, 063114.

(17) Saavedra, H. M.; Barbu, C. M.; Dameron, A. A.; Mullen, T. J.; Crespi, V. H.; Weiss, P. S. 1-Adamantanethiolate Monolayer Displacement Kinetics Follow a Universal Form. *J. Am. Chem. Soc.* **2007,** *129*, 10741–10746.

(18) Kim, M.; Hohman, J. N.; Morin, E. I.; Daniel, T. A.; Weiss, P. S. Self-Assembled Monolayers of 2-Adamantanethiol on Au{111}: Control of Structure and Displacement. *J. Phys. Chem. A* **2009,** *113*, 3895–3903.

(19) Claridge, S. A.; Liao, W.-S.; Thomas, J. C.; Zhao, Y.; Cao, H. H.; Cheunkar, S.; Serino, A. C.; Andrews, A. M.; Weiss, P. S. From the Bottom Up: Dimensional Control and Characterization in Molecular Monolayers. *Chem. Soc. Rev.* **2013,** *42*, 2725–2745.

(20) Bould, J.; Machacek, J.; Londesborough, M. G. S.; Macias, R.; Kennedy, J. D.; Bastl, Z.; Rupper, P.; Base, T. Decaborane Thiols as Building Blocks for Self-Assembled Monolayers on Metal Surfaces. *Inorg. Chem.* **2012,** *51*, 1685–1694.

(21) Ferris, J. H.; Kushmerick, J. G.; Johnson, J. A.; Youngquist, M. G. Y.; Kessinger, R. B.; Kingsbury, H. F.; Weiss, P. S. Design, Operation, and Housing of an Ultrastable, Low Temperature, Ultrahigh Vacuum Scanning Tunneling Microscope. *Rev. Sci. Instrum.* **1998,** *69*, 2691–2695.

(22) Bumm, L. A.; Arnold, J. J.; Charles, L. F.; Dunbar, T. D.; Allara, D. L.; Weiss, P. S. Directed Self-Assembly to Create Molecular Terraces with Molecularly Sharp Boundaries in Organic Monolayers. *J. Am. Chem. Soc.* **1999,** *121*, 8017–8021.

(23) Hohman, J. N.; Zhang, P.; Morin, E. I.; Han, P.; Kim, M.; Kurland, A. R.; McClanahan, P. D.; Balema, V. P.; Weiss, P. S. Self-Assembly of Carboranethiol Isomers on Au{111}:

Intermolecular Interactions Determined by Molecular Dipole Orientations. *ACS Nano* **2009,** *3*, 527–536.

(24) Weck, M.; Jackiw, J. J.; Rossi, R. R.; Weiss, P. S.; Grubbs, R. H. Ring-Opening Metathesis Polymerization from Surfaces. *J. Am. Chem. Soc.* **1999,** *121*, 4088–4089.

(25) Tillekaratne, A.; Trenary, M. Adsorption and Dehydrogenation of Decaborane on the Pt(111) Surface. *J. Phys. Chem. C* **2009,** *113*, 13847–13854.

(26) Bumm, L. A.; Arnold, J. J.; Cygan, M. T.; Dunbar, T. D.; Burgin, T. P.; Jones, L.; Allara, D. L.; Tour, J. M.; Weiss, P. S. Are Single Molecular Wires Conducting? *Science* **1996,** *271*, 1705–1707.

(27) Weiss, P. S. Functional Molecules and Assemblies in Controlled Environments: Formation and Measurements. *Acc. Chem. Res.* **2008,** *41*, 1772–1781.

CHAPTER 5

Summary and Outlook

5.1 Characterization of Photo-Induced Charge Distribution at the Single-Molecule Level

Combining laser illumination and scanning tunneling microscopy (STM) provides a way to characterize the photo-response of molecules and nanomaterials with nanometer-scale resolution in real time and space. In Chapter 1 of this thesis, a custom-built laser-assisted STM that functions at ambient conditions and room temperature has been introduced. Laser illuminations are frequency modulated and incorporated into the tunneling junction through total internal reflection to minimize the thermal effect. Phase-sensitive detection on the tunneling current is conducted using a lock-in amplifier during the raster scan to generate maps of photo-induced carriers. The thermal effect of the evanescent illumination is tested with *n*-dodecanethiol (C12) self-assembled monolayers (SAMs) and is used to determine whether the lasers are illuminating the raster scan area properly. The reference phase of the lock-in amplifier is adjusted based on the thermal effect signals so that the phase shift of thermal expansion signal is 0° at positive sample bias and 180° at negative sample bias. In this case, the magnitude of in-phase signal is maximized the magnitude of quadrature signal is minimized. In-phase signals are used in spectroscopic images to represent photoelectron densities since it depends on the polarity of the sample bias. It has also been demonstrated in Chapter 1 that, in C12 SAMs, areas with higher apparent height correspond to higher thermal expansion signals. Such information can be used to differentiate photo-induced charges and thermal expansion signals in other systems.

In Chapters 2 and 3, we present our studies on photoactive molecules using the custom-built laser-assisted STM. Two strategies involving highly ordered SAMs have been used for STM to get molecular resolution under ambient conditions and room temperature. C_{60}-tethered 2,5-dithienylpyrrole triads (C_{60} triads) are isolated in C12 SAMs while titanyl phthalocyanine

(TiOPc) molecules can self-assemble into two different lattice structures (hexagonal and rectangular) on Au{111}. Using our spectroscopic imaging method, we have visualized the distribution of photo-induced electrons and holes in single C_{60} triad molecules, which is absent for matrix and control molecules. Our data show that the conformation of C_{60} triads can affect the generation efficiency of photo-induced carriers. The photo-response of TiOPc SAMs is also characterized by our laser-assisted STM. We found out that TiOPc molecules in hexagonal lattices can be activated by both 633 nm and 780 nm light. The electron density changes in TiOPc molecules upon activation is in accordance with theoretical results. However, the photo-response of TiOPc molecules in rectangular lattices is different from that in hexagonal lattices and not correspond to theoretical predictions. Our tentative explanation is that TiOPc molecules in rectangular lattices cannot be activated by 633 nm or 780 nm light, indicating that the packing arrangement of TiOPc can influence its optical properties. Our study also shows that the photo-induced carrier generation efficiency of TiOPc can be affected by local environment such as surface morphology.

The laser-assisted STM demonstrated in this thesis can be used as a powerful diagnostic tool for photoactive molecules and nanostructures. By anchoring and isolating photoactive molecules in well-defined SAMs on gold or exploring highly ordered photoactive molecular assemblies, we can study single-molecule photon absorption at ambient conditions and obtain information that is relevant to real application systems. Such information may have been neglected or lost by traditional characterization methods due to the averaging or integrating measurements at the ensemble level. With knowledge of the factors that can influence the distribution of

photo-generated carriers in single molecules, we can better engineer improved photoactive molecules or local environments to achieve more efficient photovoltaic or optoelectronic devices.

5.2 Properties of 1-Decaboranethiolate Self-Assembled Monolayers

1-Decaboranethiol can form disordered SAMs on Au{111} with evenly distributed defects. We have been able to insert *n*-dodecanethiol molecules in these defects and obtained molecular level mixed SAMs (Figure 5.1). The inserted molecules are evenly distributed and well isolated by 1-decaboranethiolate molecules. Potential reactivity of the decaborane group suggests that with 1-decaboranethiolate SAMs, we may be able to attach electron donor/acceptor functional groups on the surface after the insertion of electron acceptor/donor molecules and achieve molecular level mixed *p-n* junctions. However, while studying the reactivity of the 1-decaboranethiolate molecules, we found out that the reaction between 1-decaboranethiolate and 4-phenyl-1-butyne (4p1b) can result in the displacement of the 1-decaboranethiolate molecules and highly ordered SAMs of 4p1b. The displacement process was characterized by STM, grazing incidence Fourier transform infrared (FTIR) spectroscopy, and X-ray photoelectron spectroscopy (XPS). Results from STM and FTIR suggest that the process happens gradually and XPS results confirm the total substitution of 1-decaboranethiolate. This process provides a way to fabricate highly ordered terminal alkyne SAMs in air that cannot be achieved through direct deposition of alkynes. Other reactions of 1-decaboranethiolate that proceed less harshly are still worth exploring as unique surface modification methods.

5.3 Potential Novel Photoactive Systems for Laser-Assisted Scanning Tunneling Microscopy

Laser-assisted STM techniques have been used to study the electronic and optical properties of semiconducting nanomaterials to obtain fundamental information on how to modify and apply

these systems.[1-7] We are investigating novel thin-film nanomaterials as candidate objects for our laser-assisted STM. One potential class of materials are metal-organic chalcogenolate assemblies (MOCHAs) since they can be distributed or grown *in situ* on conductive surfaces and they are atomically flat and thus suitable for STM analysis. Recently, a MOCHA material, silver benzeneselenolate (Mithrene) has been discovered and studied.[8,9] It has been shown that Mithrene can be synthesized through the tarnishing process of silver metal with diphenyl diselenide (DPSe).[10] We adopted this synthetic method to prepare Mithrene on sapphire/Au/Ag substrates. Thin Ag films (5 nm) were deposited on sapphire prism-supported Au{111} substrates at 300 ℃ and an evaporation rate of 0.11 Å/s. Mithrene can be prepared by sealing such silver substrates with solid DPSe in a vial and heating the system at 80 ℃ for 3 days (Figure 5.2). Scanning electron microscopy images of the substrates in Figure 5.3 show that we have successfully synthesized thin-film Mithrene on the surface. The square shape and darker color of Mithrene make it straightforwardly distinguished from the substrate. We can see that Mithrene is evenly distributed on the surface but there can be a 1-2 μm gap between neighboring Mithrene, making it difficult to locate with STM. Preliminary STM data are presented in Figure 5.4, which are consecutively collected STM topographic images of the same area under 405 nm laser illumination (5 mW). We can see from Figure 5.4 that the presented area decomposed during the data collection period. Such decomposition can be due to the strong intensity of the laser since no large-scale decomposition has been observed in photoluminescence experiments.[9,10] The laser power and scanning conditions need to be optimized for photocurrent measurements. Furthermore, scanning tunneling spectroscopy is a promising method to characterize the band gap of Mithrene and to determine the energy conversion efficiency in Mithrene upon optical activation.

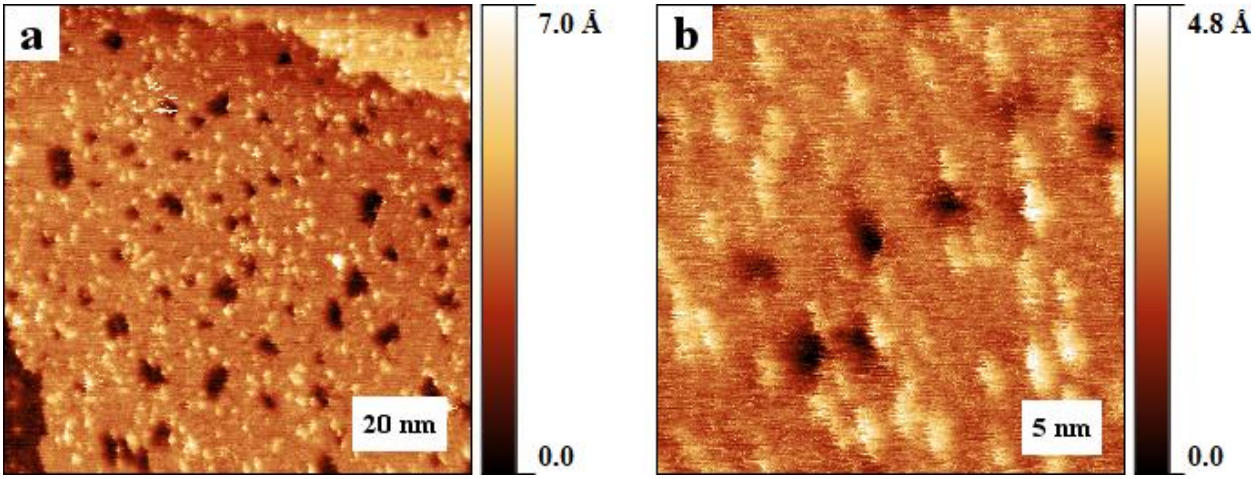

Figure 5.1. Scanning tunneling microscopy images of *n*-dodecanethiol molecules inserted in 1-decaboranethiol self-assembled monolayers at the scales of (a) 100 nm × 100 nm and (b) 30 nm × 30 nm on Au{111}. All images were collected at a sample bias of +1.00 V and a tunneling current of 12.0 pA.

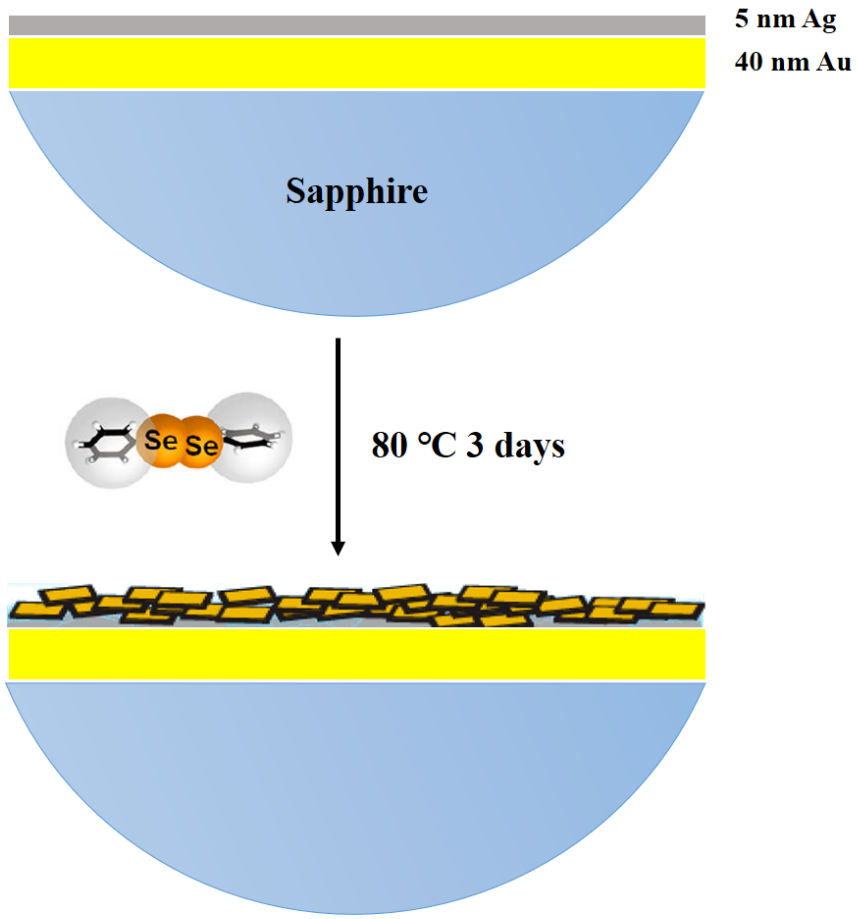

Figure 5.2. Scheme showing the synthesis of Mithrene on sapphire/Au/Ag substrate.

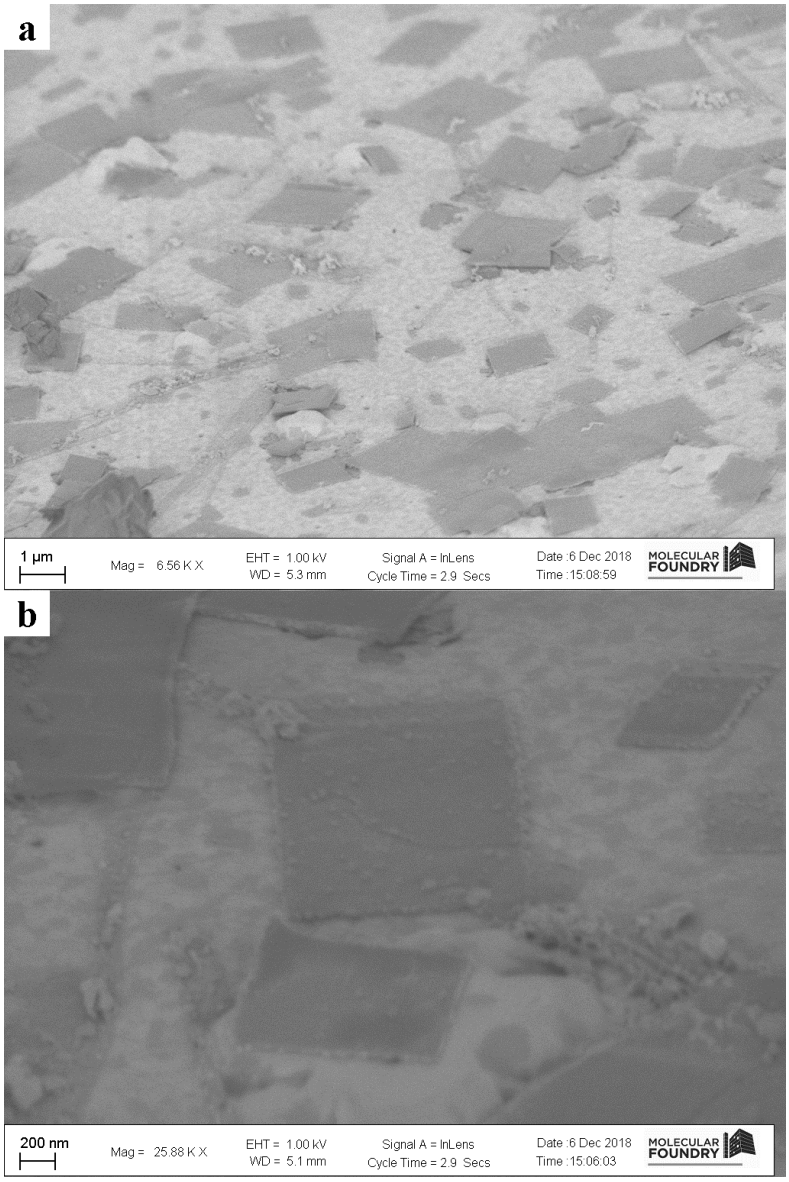

Figure 5.3. (a,b) Scanning electron microscopy images of Mithrene on sapphire/Au/Ag substrate.

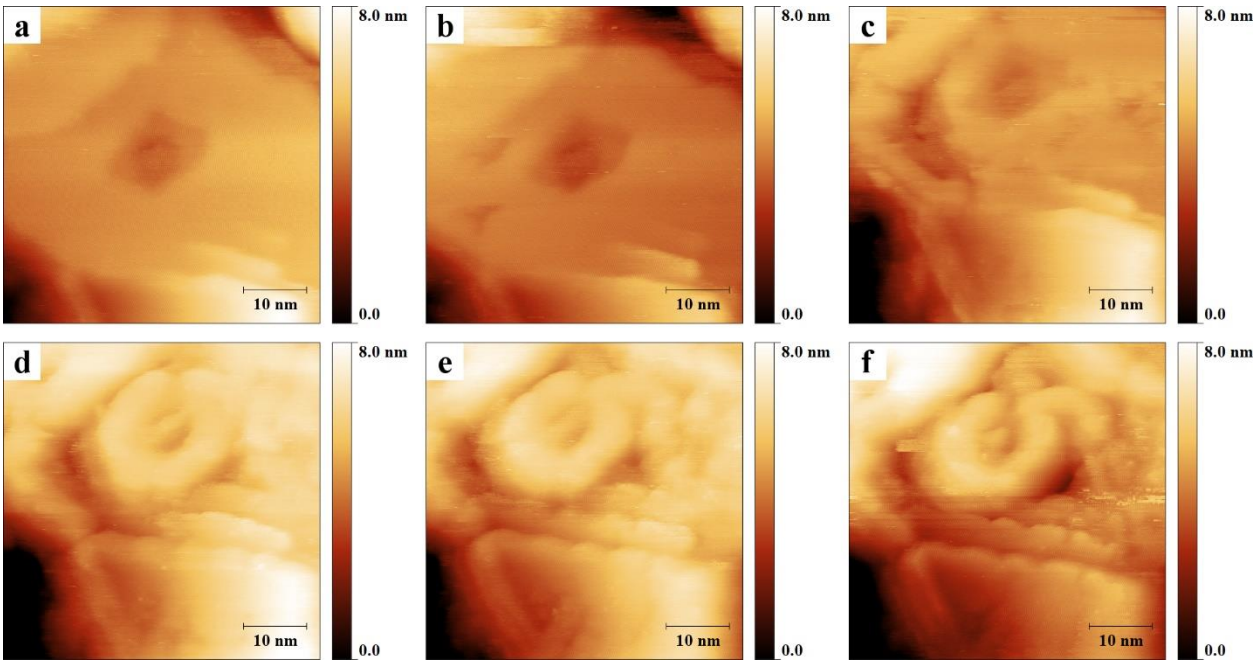

Figure 5.4. (a-f) Consecutively collected scanning tunneling microscopy (STM) topographic images showing the decomposition of Mithrene under 405 nm laser illumination. Figure (a) and (f) are collected without illumination. Figure (b-e) are collected under 405 nm laser illumination (5 mW). All STM images were collected at a sample bias of -1.00 V and a tunneling current of 12 pA.

REFERENCES

(1) Yasuhiko, T.; Masahiro, A.; Hiroyuki, K.; Atsushi, T.; Osamu, T.; Hidemi, S. Ultrafast Photoinduced Carrier Dynamics in GaNAs Probed Using Femtosecond Time-Resolved Scanning Tunnelling Microscopy. *Nanotechnology* **2007,** *18*, 044028.

(2) Shoji, Y.; Yuya, K.; Ryuji, O.; Yoshitaka, O.; Osamu, T.; Hidemi, S. Nanoscale Mapping of Built-in Potential in GaAs p–n Junction Using Light-Modulated Scanning Tunneling Microscopy. *Jpn. J. Appl. Phys.* **2008,** *47*, 6117–6120.

(3) Yoshida, S.; Terada, Y.; Oshima, R.; Takeuchi, O.; Shigekawa, H. Nanoscale Probing of Transient Carrier Dynamics Modulated in a GaAs-PIN Junction by Laser-Combined Scanning Tunneling Microscopy. *Nanoscale* **2012,** *4*, 757–761.

(4) Nienhaus, L.; Wieghold, S.; Nguyen, D.; Lyding, J. W.; Scott, G. E.; Gruebele, M. Optoelectronic Switching of a Carbon Nanotube Chiral Junction Imaged with Nanometer Spatial Resolution. *ACS Nano* **2015,** *9*, 10563–10570.

(5) Nguyen, D.; Nguyen, H. A.; Lyding, J. W.; Gruebele, M. Imaging and Manipulating Energy Transfer Among Quantum Dots at Individual Dot Resolution. *ACS Nano* **2017,** *11*, 6328–6335.

(6) Nguyen, H. A.; Banerjee, P.; Nguyen, D.; Lyding, J. W.; Gruebele, M.; Jain, P. K. STM Imaging of Localized Surface Plasmons on Individual Gold Nanoislands. *J. Phys. Chem. Lett.* **2018,** *9*, 1970–1976.

(7) Nguyen, D.; Wallum, A.; Nguyen, H. A.; Nguyen, N. T.; Lyding, J. W.; Gruebele, M. Imaging of Carbon Nanotube Electronic States Polarized by the Field of an Excited Quantum Dot. *ACS Nano* **2019,** *13*, 1012–1018.

(8) Cuthbert, H. L.; Wallbank, A. I.; Taylor, N. J.; Corrigan, J. F. Synthesis and Structural Characterization of $[Cu_{20}Se_4(\mu_3\text{-}SePh)_{12}(PPh_3)_6]$ and $[Ag(SePh)]_\infty$. *Z. Anorg. Allg. Chem.* **2002,** *628*, 2483–2488.

(9) Schriber, E. A.; Popple, D. C.; Yeung, M.; Brady, M. A.; Corlett, S. A.; Hohman, J. N. Mithrene is a Self-Assembling Robustly Blue Luminescent Metal–Organic Chalcogenolate Assembly for 2D Optoelectronic Applications. *ACS Appl. Nano Mater.* **2018,** *1*, 3498–3508.

(10) Trang, B.; Yeung, M.; Popple, D. C.; Schriber, E. A.; Brady, M. A.; Kuykendall, T. R.; Hohman, J. N. Tarnishing Silver Metal into Mithrene. *J. Am. Chem. Soc.* **2018,** *140*, 13892–13903.